

University of Alberta

Experimental Investigation of Pore Scale Velocity within Micro Porous Media

by

Debjyoti Sen

A thesis submitted to the Faculty of Graduate Studies and Research
in partial fulfillment of the requirements for the degree of

Master of Science

Department of Mechanical Engineering

©Debjyoti Sen

Fall 2011

Edmonton, Alberta

Permission is hereby granted to the University of Alberta Libraries to reproduce single copies of this thesis and to lend or sell such copies for private, scholarly or scientific research purposes only. Where the thesis is converted to, or otherwise made available in digital form, the University of Alberta will advise potential users of the thesis of these terms.

The author reserves all other publication and other rights in association with the copyright in the thesis and, except as herein before provided, neither the thesis nor any substantial portion thereof may be printed or otherwise reproduced in any material form whatsoever without the author's prior written permission

THIS THESIS IS DEDICATED TO MY PARENTS. THANK YOU MOM FOR ALL THE LOVE, AFFECTION AND THE SACRIFICES YOU MADE IN BRINGING ME UP. I WOULD LIKE TO THANK MY DAD, WHOM I CONSIDER TO BE MY FAVORITE TEACHER, PHILOSOPHER, FRIEND AND GUIDE. THANK YOU FOR TEACHING ME ALL THE FUNDAMENTALS SINCE CHILDHOOD AND INSPIRING ME TOWARDS SCIENCE AND TECHNOLOGY.

ABSTRACT

An experimental technique to quantify velocity field at pore scale within micro porous media, formed by packing of micro glass spheres inside a glass micro-model, is presented. A scanning micro particle image velocimetry (μ -PIV) system is used to obtain two component two dimensional (2C2D) velocity field at two different measurement planes-one close to the glass wall and the other 100 μm below the glass surface. A combined PIV and particle tracking velocimetry (PTV) algorithm is used to quantify velocity within the micro-porous media. The probability density functions for axial and transverse velocity components at different Reynolds number are compared with available results in literature.

The three component three dimensional (3C3D) velocity field is obtained by scanning through 100 μm inside the porous media. The pore scale velocity field obtained can provide insight to flow properties in micro-porous media and can be a powerful tool to validate existing numerical results

TABLE OF CONTENT

CHAPTER 1: Introduction	1
1.1 Motivation.....	1
1.2 Literature Review.....	1
1.3 Summary and Thesis Outline.....	6
CHAPTER 2: Experimental Method and Apparatus	10
2.1 Introduction.....	10
2.2 Flow cell and flow facility	10
2.3 Experimental Details.....	13
2.3.1 Description of μ -PIV set up.....	17
2.3.2 Field of View and Resolution	20
2.3.3 Data Acquisition	21
2.3.4 Calibration.....	24
2.4 Image pre-processing	27
2.4.1 Subtract a sliding minimum.....	27
2.4.2 Multiplication to increase intensity count.....	28
2.4.3 Subtract a constant value	28
2.4.4 Linear smoothing filter	29
2.5 Vector field calculation.....	32
2.5.1 2C2D vector field calculation	32
2.5.2 Vector field post processing.....	36
2.5.3 3C3D vector field calculation	39
2.6 Errors.....	42
2.7 Summary.....	45

CHAPTER 3: RESULTS AND DISCUSSIONS PERTAINING TO 2C2D VELOCITY FIELD MEASUREMENT.....	46
3.1 Introduction.....	46
3.2 Velocity field at different regions.....	46
3.3 Probability density functions for the velocity field.....	56
3.3.1 Pdf of transverse velocity field.....	62
3.3.2 Pdf of longitudinal velocity field.....	66
3.4 Summary.....	71
 CHAPTER 4: RESULTS AND DISCUSSIONS PERTAINING TO THE 3C3D VELOCITY FIELD MEASUREMENT.....	 72
4.1 Introduction.....	72
4.2 3C3D velocity field.....	73
4.3 Probability density function for w component.....	80
4.4 Summary.....	83
 CHAPTER 5: CONCLUSION.....	 85
5.1 2C2D velocity field.....	85
5.2 3C3D velocity field.....	86
5.3 Future work.....	86
5.3.1 Matched refractive index technique.....	86
5.3.2 3D PIV +PTV.....	87
5.3.3 Validation of out of plane component of velocity.....	87
5.3.4 Ordered porous media.....	88
 REFERENCES.....	 89

LIST OF TABLES

Table 1-1 A summary of experimental and numerical studies in porous media	7
Table 2-1 A summary of time interval between each image in a double frame image	33
Table 3-1 Comparison of velocity field at different locations denoted by L1, L2, L3 and L4. $ \overline{V}_L $ denotes the magnitude of average velocity at location L and the $ \overline{V}_2 $ represents the magnitude of velocity for the entire region at $Q_s = 60 \mu\text{l}/\text{min}$. The magnitude of velocity field at both planes denoted by z is studied.	55
Table 3-2 A summary of flow rate (Q_s), average velocity field and Reynolds number for region R2. The observations are made close to wall at $z = 25 \mu\text{m}$	60
Table 3-3 A summary of flow rate (Q_s), average velocity field and Reynolds number for different regions. The observations are made close to wall at $z = 25 \mu\text{m}$	61
Table 3-4 A summary of flow rate (Q_s), average velocity field and Reynolds number for different regions. The observations are made at mid plane location at $z = 100 \mu\text{m}$. 61	
Table 4-1 The mean value of w denoted by \overline{w} , for each spatial location denoted by L ₁ , L ₂ , L ₃ and L ₄ are shown below. z represents the plane at which the values of \overline{w} is measured.	80
Table B-1 Specification of the illumination source (continuous green laser)	96
Table B-2 Specifications of fluorescent tracing particles	97
Table B-3 Specification of the high speed camera.	98

LIST OF FIGURES

Figure 2-1 An exploded solid model view of the flow cell holder.	11
Figure 2-2 A section view of a channel in the flow cell holder.	11
Figure 2-3 A schematic showing the packed bed of 200 μm size glass spheres. The image was taken using bright field imaging technique with a 2.5 X microscopic objective. Four representative location R1, R2, R3 and R4 are identified for the 2C2D velocity field measurement.....	13
Figure 2-4 A schematic showing location of focal plane where measurement was taken for the 2C2D experiment.	15
Figure 2-5 A raw image from the camera showing a pore formed by 400 μm glass spheres. The 3C3D velocity field is studied in this single pore.....	16
Figure 2-6 A schematic showing the z plane locations for the 3C3D velocity field measurement experiment. The 3C3D velocity field is obtained by scanning the pore region from $z = 0 \mu\text{m}$ through $z = 100 \mu\text{m}$ plane.	17
Figure 2-7 (a) The solid model of the scanning μ -PIV system. (b) Schematic of the scanning μ -PIV system.	19
Figure 2-8 Timing diagram for the piezo and the camera. A constant voltage is applied to the piezo stage to fix the location of the focal plane. The camera takes 1000 images with 200 frames per second. (a) The focal plane is set at $z = 25 \mu\text{m}$. (b) The focal plane is set at $z = 100 \mu\text{m}$ plane.....	22
Figure 2-9 A timing diagram showing the control signals for synchronization of camera with the piezo stage for 3C3D velocity field measurement.....	23
Figure 2-10 An image of the micro calibration target showing grid spacing and line width.	25
. Figure 2-11 An image of a standard scale used for verifying calibration factor.	26
Figure 2-12. Image pre-processing steps used to identify the fluorescent tracing particle. (a) Raw image (b) Subtract sliding minimum over 6×6 pixels (c) Subtraction of constant intensity count (d) Linear smoothing filter 3×3 pixels (e) Shape of	

fluorescent particle (zoomed in) spread over 1-2 pixels (f) Shape of fluorescent particles (zoomed in) after linear smoothening over 3×3 pixels.....	30
Figure 2-13 A comparison of intensity map before and after image pre-processing is shown. (a) The intensity map of the raw image shows lot of noise. The intensity of the particles are swamped by the background noise (b) The intensity map after image pre-processing shows sharp peaks at the location of the fluorescent particles	31
Figure 2-14 A schematic showing conversion of time series images into double frame images	32
Figure 2-15 A schematic showing comparison of PIV and PTV process. (a) A PIV process correlates a group of particles in the interrogation window and calculates the displacement of a group of particles (b) A PTV algorithm finds out the displacement of each individual particle.....	34
Figure 2-16 Instantaneous velocity field obtained after processing a double frame image. The vectors are overlaid on top of the raw image of $200 \mu\text{m}$ glass spheres. The vector field obtained is for Region B with focal plane location at $z = 25 \mu\text{m}$ and $Q_s = 60 \mu\text{l/min}$	36
Figure 2-17 A dense vector field is obtained after accumulating the instantaneous vector fields on to a single image.	37
Figure 2-18 The vectors obtained after accumulation are distributed on to a regular grid of 8×8 pixels	39
Figure 2-19. A schematic showing 100 images were taken in one scan to generate a volume of data. Two such consecutive volumes of data are cross correlated to obtain the 3C3D velocity field.....	40
Figure 2-20. The instantaneous 3C3D velocity field is shown. The in-plane velocity components are shown by vector arrows .The length of the arrow denotes the magnitude of the vector. A reference vector of magnitude $10 \mu\text{m/s}$ is shown on the figure. The out of plane component is shown by the background color map and the values of w are indicated by the color bar.....	42
Figure 3-1 The pore structure at different regions is shown, each region is $800 \mu\text{m} \times 600 \mu\text{m}$. (a) Region R1 (b) Region R2 (c) Region R3 and (d) Region R4..	47

Figure 3-2 Velocity plots for $Q_s = 40 \mu\text{l}/\text{min}$. The color map shows the magnitude of velocity. (a) Close to the wall at $z = 25 \mu\text{m}$ (b) Mid plane location of first layer of spheres at $z = 100 \mu\text{m}$ 50

Figure 3-3 Velocity plots for $Q_s = 60 \mu\text{l}/\text{min}$. The color map shows the magnitude of velocity. (a) Close to the wall at $z = 25 \mu\text{m}$ (b) Mid plane location of first layer of spheres at $z = 100 \mu\text{m}$ 51

Figure 3-4 Velocity plots for $Q_s = 80 \mu\text{l}/\text{min}$. The color map shows the magnitude of velocity. (a) Close to the wall at $z = 25 \mu\text{m}$ (b) Mid plane location of first layer of spheres at $z = 100 \mu\text{m}$ (b) 52

Figure 3-5 Velocity plots for $Q_s = 100 \mu\text{l}/\text{min}$. The color map shows the magnitude of velocity. (a) Close to the wall at $z = 25 \mu\text{m}$ (b) Mid plane location of first layer of spheres at $z = 100 \mu\text{m}$ 53

Figure 3-6 A comparison of pdf predicted by histogram with kernel density function for transverse velocity component for region R2 at $Q_s = 100 \mu\text{l}/\text{min}$. The observation was made for data obtained close to the wall at $z = 25 \mu\text{m}$ plane. (a) A normalized histogram is plotted with bin size $10 \mu\text{m}/\text{s}$. (b) A smooth velocity profile obtained by kernel density estimator which closely preserves the trend of the histogram. 58

Figure 3-7 A comparison of pdf predicted by histogram with kernel density function for axial velocity component for region R2 at $Q_s = 100 \mu\text{l}/\text{min}$. The observation was made for data obtained close to the wall at $z = 25 \mu\text{m}$ plane (a) A normalized histogram is plotted with bin size $10 \mu\text{m}/\text{s}$. (b) A smooth velocity profile obtained by kernel density estimator which closely preserves the trend of the histogram. 59

Figure 3-8 The probability density function (pdf) of non-dimensionalized transverse (y-component) velocity $\left(\frac{v_i}{\sigma_{v_i}}\right)$ is plotted, where σ_{v_i} the standard deviation of v_i is, is plotted. The velocity data are obtained from R2 at $z = 25 \mu\text{m}$ plane. (a) pdf $\left(\frac{v_i}{\sigma_{v_i}}\right)$ is denoted by *asterisk*. v_i is the transverse velocity component corresponding to the mean velocity and $\text{Re}_p = 0.023$. A normal Gaussian curve is fitted to the data as shown by *dotted lines*. The results are compared with Moroni and Cushman (2001) ,

denoted by *upward pointing triangle*. (b) pdf is plotted for four Reynolds numbers.

..... 63

Figure 3-9 The probability density function (pdf) of non-dimensionalized transverse (y-

component) velocity $\left(\frac{v_i}{\sigma_{v_i}}\right)$ is plotted, where σ_{v_i} the standard deviation of v_i . The

velocities data are obtained at different regions are shown. (a) velocity profile close

to the wall at $z = 25 \mu\text{m}$ (b) velocity profile at mid plane location at $z = 100 \mu\text{m}$. . 65

Figure 3-10 The probability density function for longitudinal velocity component, u_i , is

plotted at different Reynolds number. The velocity data is obtained at region R2 at z

$= 25 \mu\text{m}$ plane..... 66

Figure 3-11 The probability density function (pdf) of non-dimensionalized longitudinal

(x-component) velocity $\left(\frac{u_i}{\bar{u}_i}\right)$, where \bar{u}_i is the arithmetic mean of u_i , is plotted on the

vertical axis and $\left(\frac{u_i}{u_i}\right)$ is plotted on the horizontal axis. The velocity data is obtained

from region R2 at $z = 25 \mu\text{m}$ plane (a) pdf $\left(\frac{u_i}{\bar{u}_i}\right)$ is denoted by *asterisk*. u_i is the

transverse velocity component corresponding to mean velocity $|\bar{v}_i| = 117 \mu\text{m/s}$ and

$Re_p = 0.023$. The results are compared with Lebon et al. (1996) denoted by *upward*

pointing triangle and Maier et al. (1998) denoted by *right pointing triangle* (b) pdf

$\left(\frac{u_i}{\bar{u}_i}\right)$ is plotted for four different Reynolds number..... 68

Figure 3-12 The probability density function (pdf) of non-dimensionalized longitudinal

(x-component) velocity $\left(\frac{u_i}{\bar{u}_i}\right)$, where \bar{u}_i is the arithmetic mean of u_i , is plotted on the

vertical axis and $\left(\frac{u_i}{u_i}\right)$ is plotted on the horizontal axis. The velocity profile at

different regions are studied. (a) velocity profile close to the wall at $z = 25 \mu\text{m}$ (b)

velocity profile at mid plane location at $z = 100 \mu\text{m}$ 70

Figure 4-1 A micro pore region formed by 4 glass spheres of $400 \mu\text{m}$ diameters and

denoted by S1, S2, S3 and S4. Four regions which are denoted by L₁, L₂, L₃ and L₄

are identified. The out of plane component of velocity, w , is quantified for each of this locations. 73

Figure 4-2 The horizontal and vertical axis represents position of x and y co-ordinate respectively in μm . The direction of flow is in negative x -direction. The in plane velocity components are denoted by the vectors. The length of the vectors denotes the magnitude. A reference velocity vector of $10 \mu\text{m/s}$ is shown. The out of plane velocity component, w , is shown by the color map and the color bar represents corresponding values of w . $Q_s = 0.1 \mu\text{l/min}$ and $\text{Re}_p = 6.4 \times 10^{-4}$. All spatial positions are in μm . Each subplot represents velocity field at a z -plane. (a) $z = 0 \mu\text{m}$ (b) $z = 9 \mu\text{m}$ (c) $z = 18 \mu\text{m}$ (d) $z = 27 \mu\text{m}$ (e) $z = 36 \mu\text{m}$ (f) $z = 45 \mu\text{m}$ (g) $z = 54 \mu\text{m}$ (h) $z = 63 \mu\text{m}$ 77

Figure 4-3 The probability density function (pdf) of non-dimensionalized transverse (z -component) velocity $\left(\frac{w}{\sigma_w}\right)$, where σ_w the standard deviation of w is, is plotted on the vertical axis and $\left(\frac{w}{\sigma_w}\right)$ is plotted on the horizontal axis. The probability density function is plotted using kernel density estimator 81

Figure 4-4 The probability density function (pdf) of non-dimensionalized transverse (y -component) velocity $\left(\frac{v}{\sigma_v}\right)$, where σ_v the standard deviation of v is, is plotted on the vertical axis and $\left(\frac{v}{\sigma_v}\right)$ is plotted on the horizontal axis. The probability density function is plotted using kernel density estimator 82

Figure 4-5 The probability density function (pdf) of non-dimensionalized longitudinal (x -component) velocity $\left(\frac{u}{\sigma_u}\right)$ is plotted. The probability density function is plotted using kernel density estimator 82

LIST OF NOMENCLATURE

Latin Symbols

d_e Image diameter of a particle on CCD sensor [pixels]

d_p Diameter of glass beads [μm]

d_{pf} Diameter of a fluorescent particle [μm]

\mathcal{D} Diffusion coefficient [m^2/s]

h Bandwidth of a Kernel

i Used as an index to specify flow rate

j counter used for counting number of velocity vectors

k Counter used to count number of images

K Kernel function

M Magnification of the objective

n Number of images in a data set

N Number of vectors in an image

Q_s Inlet flow rate from the syringe pump ($\mu\text{l}/\text{min}$)

Re_pReynolds number based on particle diameter

sDisplacement of particle due to diffusion [m]

tTime (s)

TTemperature [K]

u, v, w x, y, z component of velocity respectively

u_0, v_0, w_0value of u, v, w at spatial location (x_0, y_0, z_0)

$u_{dev}, v_{dev}, w_{dev}$Deviation of u, v, w from the neighboring vectors

$\bar{u}, \bar{v}, \bar{w}$ Arithmetic mean of each component of velocity

\mathbf{V}Velocity vector

V_iVelocity at flow rate specified by i

$|\mathbf{V}|$Magnitude of velocity vector

$\overline{|\mathbf{V}|}$ Average value of velocity field at a region in space

x, y, z Positional coordinates

VVolts

Greek Symbols

ρDensity of the working fluid[kg/m^3]

ρ_pDensity of fluorescent particle [kg/m^3]

λWavelength of light[nm]

μ Viscosity of working fluid [Pa.s]

σ_{v_i} Standard deviation of the variable in subscript

ε_bRelative error due to Brownian motion

κBoltzmann Constant

Abbreviations

2C2D.....Two component two dimensional

3D.....Three dimensional

3C3D.....Three component three dimensional

NA.....Numerical aperature

PIVParticle image velocimetry

LDVLaser Doppler velocimetry

LDALaser Doppler anemometry

μ -PIVMicro Particle image velocimetry

PTV.....Particle tracking velocitmetry

PMMA.....Polymethyl methacrylate

Pdf.....Probability density function

CHAPTER 1: INTRODUCTION

1.1 Motivation

The phenomenon of flow through a porous media has applications in oil extraction from reservoirs, packed bed regenerators, packed bed micro-reactors, fuel cells, electronic equipment cooling and biomedical devices (Vafai 2005; Vafai 2010; Sahimi 1995; Neild & Bejan 2006; Pattekar & Kothare 2005). To understand, develop and optimize processes involved in these applications, transport processes in micro-porous media need to be characterized. Multiphase transport in micron-sized porous media has direct bearing on secondary and tertiary oil recovery processes from porous reservoirs(Sahimi 1995). Recent trends suggest that transport in pore-scale is becoming an important issue for energy applications (Berejnov et al. 2008). Geological studies have shown that more than 50% of oil is trapped in porous reservoirs (Sahimi 1995). Conventional oil recovery processes are not energy efficient in extracting the oil. To develop energy efficient processes for recovering the oil residing in these oil reservoirs, a thorough understanding of transport processes within micro-porous media is required.

1.2 Literature Review

Scaled down replicas of oil reservoirs have been used for laboratory experiments to predict efficiency of oil recovery processes. A common practice is to replicate the porous media by creating a micro model of packed sand or glass beads inside a flow cell

and to study transport processes by flow visualization techniques (Dawe et al. 1992; Turta et al. 2003). Santosh et al. (2007) used a flow visualization technique to determine water flood profiles during oil recovery for horizontal and vertical well configurations. They used a packed bed of white sand of size 400-600 μm inside a transparent core holder and a two dimensional study was conducted. The study provided important information about water flood profiles and it verified two dimensional numerical models. Hatiboglu & Babadagli (2008) also conducted similar flow visualization experiments using 100 μm transparent glass beads and some of the important properties of spontaneous imbibition and wetting phase flow were captured. Flow visualization experiments are based on area averaged tracers and these experiments can at most provide qualitative velocity fields.

Qualitative results can provide information about the velocity profile and are useful in studying some of the flow properties within micro porous media. Quantitative measurement of velocity field can provide a detailed understanding of transport processes in porous media and can be used for verification of available analytical and numerical results. Micro particle image velocimetry (μ -PIV) is an optical measurement technique which is used to quantify velocity field for micro scale flows (Santiago et al. 1998; Lindken et al. 2009; Lee & S. Kim 2009). Although μ -PIV technique has been used for many applications on micro scale flows, probing flow within a complex porous geometry is experimentally difficult to achieve (Perrin et al. 2005). Perrin et al. (2005) studied flow properties within a micro capillary pore using μ -PIV technique. They have quantified the velocity field within the micro capillary pore of 40 μm size. Their work elucidated that μ -PIV can be used to quantify pore scale velocity where pore size is in the order of 40 μm .

Evidence of flow measurement through “macro” porous media with complex geometry, such as porous media formed by packed glass beads, is available in the literature. Laser Doppler Velocimetry (LDV) was one of the early techniques used to measure interstitial velocity within a macro porous media (Dybbs & Edwards 1984). LDV is a non intrusive single point measurement technique and each point in the field of view needs to be probed to get an estimate of pore scale velocity field. Johnston et al. (1975) used LDV technique to study velocity field inside porous media formed by packing of plexi glass spheres of diameter 1.27 cm. The major drawback of LDV is that it’s time consuming. Being a single point measurement system, it cannot capture the temporal and spatial variation of velocity field.

Particle image velocity (PIV) has been used to measure flow velocity profiles within macro-scale porous media. The PIV technique involves creating a thin laser sheet to illuminate the area of interest in the flow which is seeded with tracing particles. Saleh et al. (1992) used PIV to study interstitial velocity field within a porous media formed by 10 mm Plexi glass beads. Aluminum particles of 4 μm size were used as tracing particles and the velocity range for their experiment was 25 $\mu\text{m/s}$ to 2.5 mm/s. Their experiments suffered from noise that originated from reflections from the glass spheres. Northrup et al. (1993) used fluorescent particle image velocimetry technique to measure two component two dimensional (2C2D) velocity fields inside a porous media formed by packing of PMMA beads of size 10 mm inside a cylindrical container. A matched refractive index technique was used to achieve optical transparency. The flow velocity for their experiment was in the order of 50 $\mu\text{m/s}$. Using fluorescent PIV, they could

successfully remove background noise due to reflection and was able to obtain better results, in terms of resolution and number of vectors, compared to Saleh et al. (1992).

PIV techniques can quantify velocity field in porous media but in cases where the seeding density of tracing particle is low, methods such as particle tracking velocimetry (PTV) can give more reliable results (Theunissen 2003). The PTV algorithm is based on tracking individual particles. PTV has been used to study pore scale velocity in macro-porous media (Moroni & Cushman 2001; Huang et al. 2008). Moroni and Cushman (2001) used two cameras and 3D-PTV technique was used to obtain three dimensional velocity field with in the porous media formed by packing of 1.9 cm diameter Pyrex spheres. Huang et al. (2008) used a PTV technique to characterize the pore scale velocity and they used a single camera to obtain two components of velocity. Moroni & Cushman (2001); Huang et al. (2008) used statistical methods to compare the longitudinal and transverse velocity with data available from literature. They established that PTV method can be used to obtain velocity field in macro porous media

The non intrusive techniques discussed above can successfully measure three component and two component velocity fields within a macro-porous media. However, measuring the three component velocity field at the micro scale requires special techniques. To measure the out-of-plane component, stereoscope μ -PIV has been introduced by Yu & Kim (2008) that utilizes a final particle tracking velocimetry (PTV) processing step. In this technique, the three components of velocity over a single plane can be measured by using two cameras and a stereoscope microscope. The out-of-plane component can also be measured using defocusing μ -PIV introduced by Kajitani & Dabari (2005). In this approach the third component of the velocity is based on the size of

the defocused ring of an imaged particle seeded in the flow. This was shown to be linearly related to the position of the particle in the out-of-plane direction and could be used to track the particle in 3D. A recent approach was introduced by Nobes et al. (2010) that used a scanning μ PIV system capable of measuring three component three dimensional velocity field (3C3D) for micro scale flows.

Nuclear magnetic resonance (NMR) spectroscopy is another non intrusive flow measurement technique used for measuring flow in packed bed of spheres (Shattuck et al. 1991; Kutsovsky et al. 1996; Lebon et al. 1996; Hunter et al. 2010). NMR spectroscopy has been used mainly to study dispersion of tracer particles inside micro porous. Lebon et al. (1996) used randomly packed glass beads of 800 μm size to study fluid displacement. They could successfully obtain velocity distribution of the longitudinal component of velocity. It was reported that the velocities close to the wall of the spheres could not be determined accurately due to loss of signal (Lebon et al. 1996; Maier et al. 1998).

Numerical models have been developed in the literature which can quantify flow velocity in both macro and micro porous media. Lattice Boltzmann simulations have become one of the popular tools to quantify flow through packed bed of spheres. Maier et al. (1998); Hill et al. (2001); Hoef et al. (2005) used Lattice Boltzmann simulations to study flow through porous media formed by packing of spheres. The length scale for these studies is typically in the order of millimeters and it can be considered to be macro scale study. Xu & Jiang (2008); Zaman & Jalali (2010) used computational fluid dynamics (CFD) technique to model flow through micro porous media. They used commercial software to quantify interstitial velocity field inside micro porous media formed by packed bed of spheres. The velocity fields were used to determine the

hydraulic permeability and the results were compared with analytical results. Akanji & Matthai (2009) highlighted the need to study pore scale flow in micro porous media and they have used a finite element method to successfully compute the velocity field within a micro-pore of size around 10 μm . Numerical works have contributed significantly in understanding flow through porous media in both macro and micro scale. Existing literature provide evidence of validation of numerical works for macro-porous media, however experimental validation of pore scale flow in micron scale porous media is still lacking.

1.3 Summary and Thesis Outline

The literature shows evidence of different techniques used for pore scale flow measurement. Non-intrusive experimental techniques such as PIV and PTV have been used to quantify velocity field in macro-porous media. Micro scale flow measurement techniques such as μ -PIV has been widely used for flow measurements in micro channels, however limited evidence was found for flow measurement with in micro-porous media. Numerical techniques have been used to quantify flow in both micro and macro porous media. A brief summary of the different flow measurement techniques used for pore scale flow measurement is given in Table 1-1

Table 1-1 A summary of experimental and numerical studies in porous media

Author, Year	d_p (mm)	$ \overline{V} $ ($\mu\text{m/s}$)	Re_p	Remark
Saleh et al. (1992)	10	25	1.25×10^{-3}	Macro scale study of porous media using PIV
Northrup et al. (1993)	10	50	3.6×10^{-3}	Macro scale study of porous media using FPIV
Maier et al. (1995)	6	100-5000	0.6-30	Numerical study using Lattice Boltzmann simulation
Lebon et al. (1996)	0.8	1300-6700	1.04-5.36	NMR study
Hassan and Dominguezontiveros (2008)	4.7	500- 1.25×10^4	2-500	Macro scale study using PIV.
Moroni and Cushman (2001)	19	2100-5510	0.049- 0.129	Macro scale study using PTV
Huang et al. (2008)	7	4000	28	Macro scale study using PIV
Zaman and Jalai (2010)	0.2-1	4	8×10^{-4} - 4×10^{-3}	Micro scale study using CFD
Present work	0.2-0.4	10^{-6} - 10^{-4}	0.02-0.05	Microscale, PIV+PTV

In Table 1-1 d_p , represents the diameter of the sphere, $|\overline{\mathbf{V}}|$ represents the magnitude of average pore scale velocity and Re_p denotes the Reynolds number. In some of the literature mentioned in Table 1-1, the values of Reynolds number is stated and for the rest, the value of Reynolds number is calculated using:

$$Re_p = \frac{d_p \rho |\overline{\mathbf{V}}|}{\mu} \quad (1.1)$$

where, ρ is the density of working fluid and μ is the viscosity of the working fluid. The value of Reynolds number gives a fair estimate of the flow regime in which the experiments are conducted.

The basic outline of the thesis is as follows- Chapter 2 of the thesis describes the flow facility which includes design, manufacturing of the flow cell and setting up of the flow. The optical measurement system and its components are described in detail in this chapter. This chapter also describes the image processing techniques and correlation techniques used to obtain the velocity fields. Two separate experimental technique is discussed in this chapter- one to obtain the 2C2D velocity field in packed bed of 200 μm spheres and the second experiment was preliminary study of 3C3D velocity field within a single pore. Chapter 3 of the thesis includes results and discussions pertaining to 2C2D velocity field. The effect of Reynolds number on transverse and axial components of velocity is studied and compared with existing literature. The result and discussions related to the 3C3D velocity field is given in chapter 4 of the thesis. The preliminary results showing the behavior of out of plane component of velocity field is discussed in this chapter. The general conclusion and scope of future work is discussed in chapter 5 of

the thesis. Appendix A of the thesis contains engineering drawings for the design of flow cell. Appendix B contains a list of equipment specifications used for the experiment.

CHAPTER 2: EXPERIMENTAL METHOD AND APPARATUS

2.1 Introduction

The experimental methodology of determining the velocity field within a micro porous media is described in this chapter. The details of the flow facility and description of flow cell used for the packed glass beads is also covered in this chapter. A detailed description of the scanning μ -PIV system and its components is provided. The image processing algorithms used for identifying the tracing particles from the raw data obtained from camera are described in details. The correlation algorithms for each case i.e., 2C2D and 3C3D data are described separately. The post processing algorithms used for refining the results are also discussed in this chapter.

2.2 Flow cell and flow facility

An exploded view of the flow cell holder used in this work is shown in Fig 2-1. This flow cell holder consists of three individual flow cells. The cell is designed using solid model software (Dassault Systemes SolidWorks Corp, SolidWorks 2009) and is manufactured using a rapid prototype (Objet, Eden 350) technique. The body of the cell is made of acrylic based photopolymer plastic (Fullcure, 720) that is built in 16 μ m layers. This allowed complex internal details to be built into the flow cell body to supply fluid from a syringe pump and hold all features. The cell consists of three independent channels with separate inlets and outlets. The internal dimensions of each channel are 14.5 \times 4.5 \times 4.5 mm³. The section view of a single channel is shown in Fig. 2-2.

Parts of this chapter appear in the following publications: 1. Sen,D., Mona A, Nobes, D.S., Mitra, S.K. (2010), *Investigation of interstitial velocity field within micro porous media*, Proceedings of the 2010 International Mechanical Engineering Congress and Exposition IMECE2010 November 12-18, 2010, Vancouver, British Columbia, Canada.

2. Sen,D., Nobes, D.S., Mitra,S.K. (2011), *Optical measurement of pore scale velocity field within micro porous media*, Microfluidics and Nanofluidics, DOI: 0.1007/s10404-011-0862-x.

3. Sen,D.,Nobes,D.S.,Bhattacharjee,S.,Mitra,S.K (2011). *Optical measurement of the motion of a spherical particle inside a micro-capillary*.ICNMM2011, June 19-22, Edmonton, Alberta, Canada

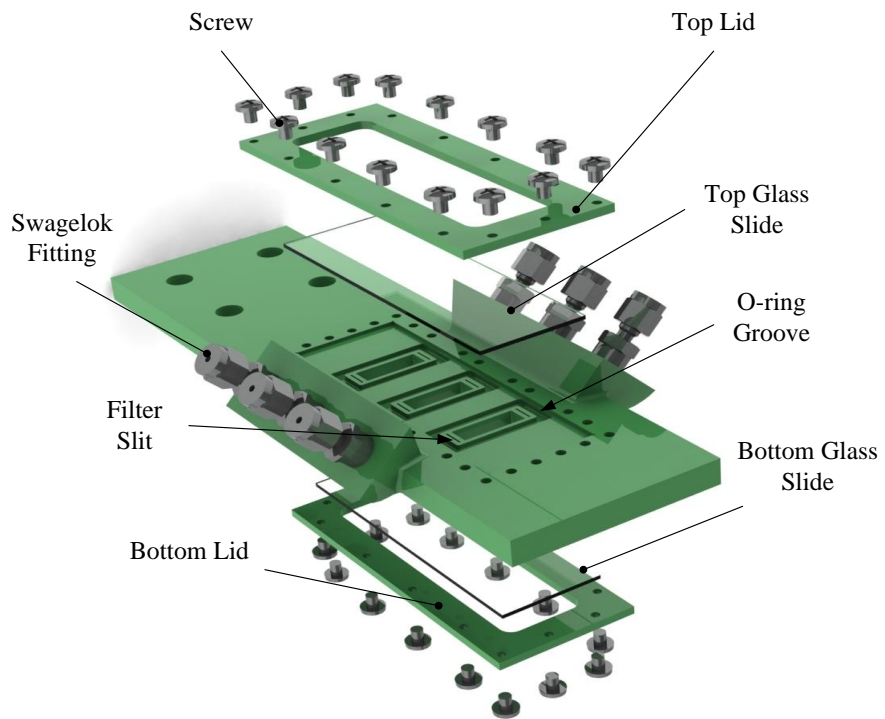


Figure 2-1 An exploded solid model view of the flow cell holder.

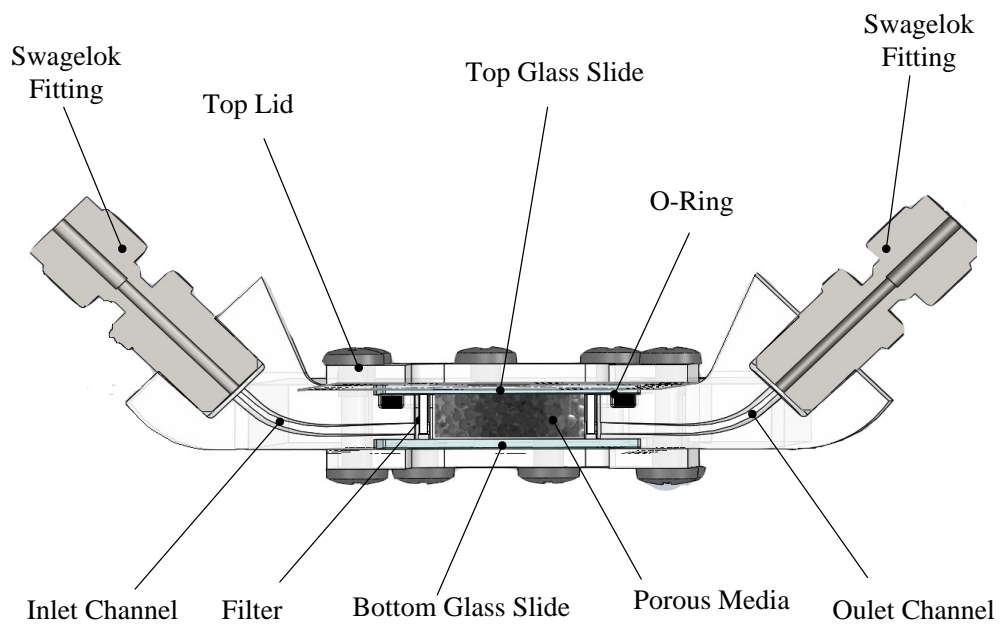


Figure 2-2 A section view of a channel in the flow cell holder.

Standard microscopic glass slides (Fisher Scientific, 12-550 A) are used as viewing windows. The rear glass slide is glued (GE, Silicone I) permanently to the back of the flow cell and the lid is secured using screws to hold the replaceable viewing window which is sealed using an O-ring (Hi-Tech Seals, 017). Filters (Millipore, SLSV025LS) with 5 μm pore size are cut and inserted in the filter slits to hold the packing material in the flow cell. The channel is packed with micro-glass beads (Corpuscular, Custom #200 glass) of nominal size 200 μm . The flow filters allow the fluorescent tracing particles (Thermo Scientific, R0200) of 2 μm size to flow through the channel and retain the micro glass beads within the flow cell. Commercial fittings (Swagelok) with 1.6 mm tubing are used at the inlet and outlet to supply and remove fluid from the flow cell. A detailed engineering drawing of the flow cell design is given in Appendix A. Optimum seeding density is obtained by adding 0.2 ml of an aqueous solution of tracing particle to 20 ml of de-ionized water. The flow is driven by a syringe pump (Harvard Apparatus, PHD 2000) which can control the flow rate precisely. A glass syringe (Hamilton, 25ml glass) of 25 ml capacity was used with the syringe pump.

After packing the channel with micro glass beads and placing the glass slides. The lids are carefully secured with bolts to ensure that the glass slide fits tightly on the O-rings and there is no leakage. Initially pure de-ionized water (without any fluorescent particles) is pumped in the flow cell using the syringe pump. A high flow rate of around 10 ml/min was maintained using the syringe pump. This ensures that the glass beads are tightly packed near the outlet filter. The packed bed was observed under a bright field microscope (Leica Microsystem, DMI 6000 B) to ensure tight packing was achieved. The flow rate was increased to 20 ml/min and no movement of the glass beads was observed.

Since the flow rate for the experiment was in the range of 100 $\mu\text{l}/\text{min}$, it ensures that during the experiments the glass beads do not move and a closed packing is achieved. After closed packing is achieved the solution of fluorescent particles is pumped through the packed bed and using the $\mu\text{-PIV}$ system data was captured.

2.3 Experimental Details

Two separate experiments were conducted; one to obtain the 2C2D velocity field for a packed bed of 200 μm glass spheres and another experiment was conducted to capture the 3C3D velocity field within 400 μm packed bed of spheres.

For the study of 2C2D velocity field, four regions of interest in the packed bed are selected, as shown in Fig. 2-3. The regions of interest are denoted by R1, R2, R3 and R4. Each region has a unique pore structure and the pore scale velocity field is studied in each of this region.

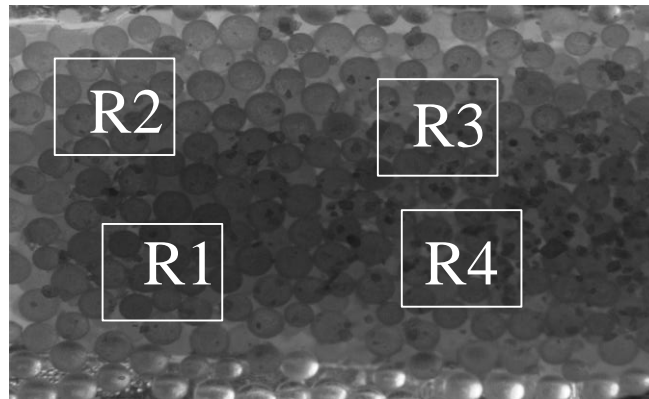


Figure 2-3 A schematic showing the packed bed of 200 μm size glass spheres. The image was taken using bright field imaging technique with a 2.5 X microscopic objective. Four representative location R1, R2, R3 and R4 are identified for the 2C2D velocity field measurement

..

Two planes are considered-one close to the glass wall at $z = 25 \mu\text{m}$ and the other in the mid plane location of first layer of spheres at $z = 100 \mu\text{m}$ as shown in Fig. 2-4. The first layer of glass spheres are tangentially touching the glass slide, the bottom of the glass slide is denoted as $z = 0$ plane. The focal plane location $z = 25 \mu\text{m}$ and $z = 100 \mu\text{m}$ are found out relative to $z = 0$ plane. The location of $z = 0$ plane was achieved by carefully marking one side of each glass with a slide symbol before placing the glass slides on the flow cell. A fine painting brush and solution of fluorescent particle was used to mark a symbol on the glass slide. The glass slide was allowed to dry and then it was placed on the flow cell such that the side marked with the symbol stays inside the flow cell. Before setting up the flow, the optical system was used to obtain a sharp focus of the mark. Since the mark was created using the solution of fluorescent particle it was clearly visible using the optical system. The $z = 0$ plane was defined where the mark was sharply in focus.

Experiments are conducted at different flow rates ranging from 40 to 100 $\mu\text{l}/\text{min}$ in steps of 20 $\mu\text{l}/\text{min}$. For each flow, rate readings were taken at $z = 25 \mu\text{m}$ and $z = 100 \mu\text{m}$ plane before moving onto the next flow rate. Once the readings were taken for a particular region at two different planes and with all flow rates, the traverse is manually moved to a different region. This process was repeated for collecting data for all other regions. The same packing was used for all the experiments.

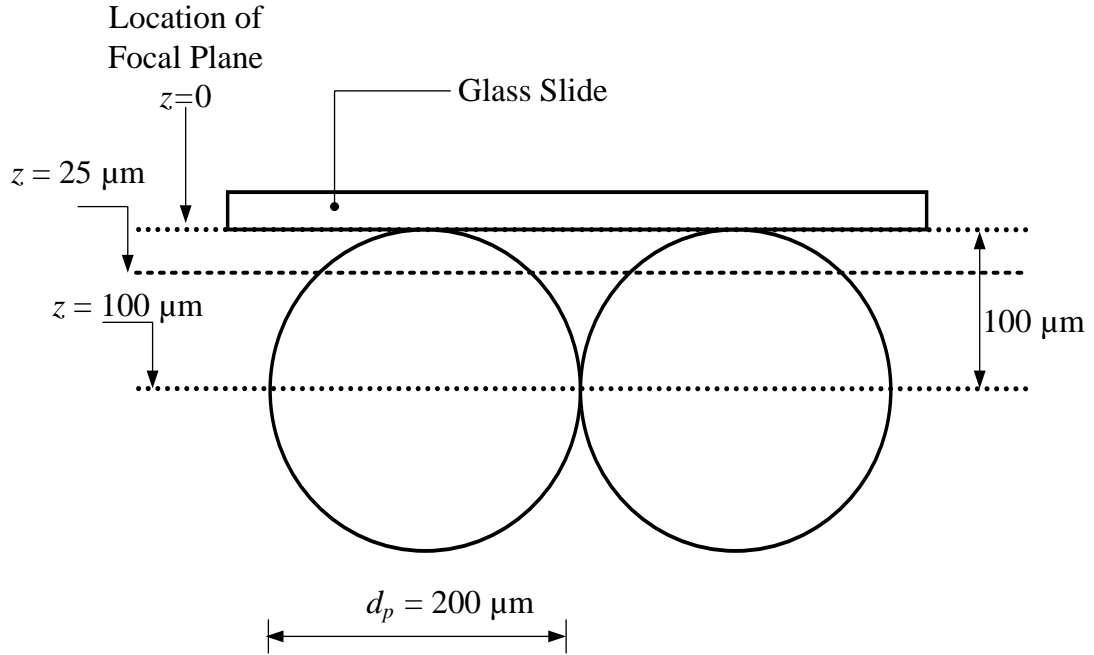


Figure 2-4 A schematic showing location of focal plane where measurement was taken for the 2C2D experiment.

The 3C3D velocity field is studied at the pore region formed between four glass spheres as shown in Fig. 2-5. The diameter of each glass sphere is $400\ \mu\text{m}$. The same procedure as discussed for 2C2D velocity field was followed to ensure closed packing of the glass beads. The experiments were conducted at low flow rate of $1\ \mu\text{l}/\text{min}$.

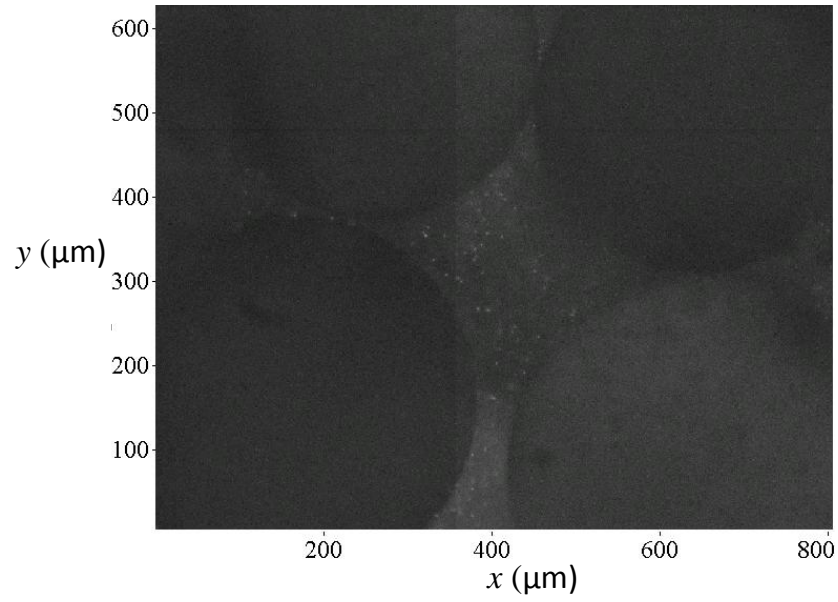


Figure 2-5 A raw image from the camera showing a pore formed by 400 μm glass spheres. The 3C3D velocity field is studied in this single pore

For the 3C3D study, the z plane locations are defined differently from 2C2D study. The mid plane location of the first layer of spheres were determined by manually focusing the optical traverse at the mid plane. The edges of the spheres appear to be sharpest at the mid plane location. The mid plane location is defined as $z = 100 \mu\text{m}$ and $z = 0$ location is defined 100 μm above it close to the glass wall as shown in Fig. 2-6. The piezo stage can scan through a maximum distance of 100 μm . Each scan was done through $z = 0 \mu\text{m}$ plane to $z = 100 \mu\text{m}$ plane, i.e, the mid plane location of first layer of spheres. Each scan results in a volume of data and two subsequent volumes of data are correlated to obtain the 3C3D velocity field.

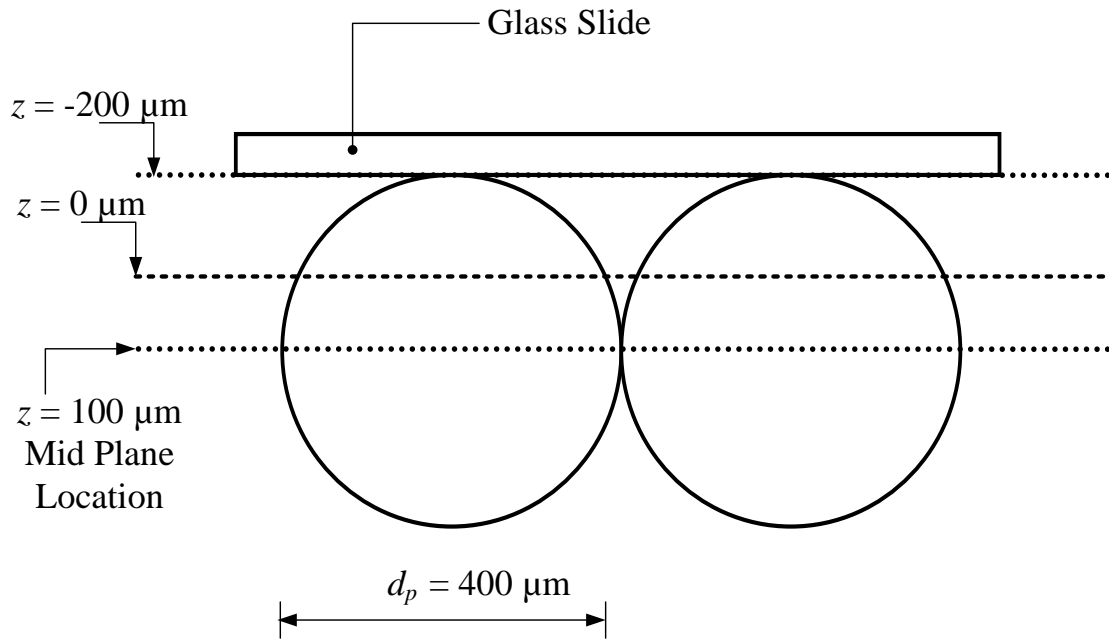


Figure 2-6 A schematic showing the z plane locations for the 3C3D velocity field measurement experiment. The 3C3D velocity field is obtained by scanning the pore region from $z = 0 \mu\text{m}$ through $z = 100 \mu\text{m}$ plane.

2.3.1 Description of μ -PIV set up

The optical set up is a μ -PIV setup based on Nobes et al. (2010) and Homeniuk (2009). The main components of the optical system are shown in. 2.7 (a). An Nd:YAG CW laser (Laser Glow, LRS 0532-PFW-02000-01) is used for illumination. The laser emits light of 532 nm wavelength which passes through a green emission filter and strikes a dichroic mirror which is oriented at an angle of 45° to the incident beam. The dichroic mirror reflects light below 600 nm, so the incident beam is reflected downward. The reflected beam strikes an infinity corrected objective (Olympus, Plan N 10x/0.25/FN22). The objective focuses the green light into the region of interest inside the porous media. Deionized water is seeded with fluorescent particles of $2 \mu\text{m}$ in size flows through the porous media. The particles fluoresce red light at 612nm when excited

with green light of 532 nm. The fluorescent particles are sized to faithfully follow the fluid motion. When the syringe pump is in operation, the fluorescent particles uniformly suspended in water starts flowing through the porous media.

A schematic of the optical system is shown in Fig. 2-7 (b). When green light from the objective strikes the fluorescent particles, they emit red light at 612 nm. The emitted red light is captured by the objective and it passes through the dichroic mirror as dichroic mirror allows light of a wavelength above 600 nm to pass through. The light passes through the field lens which focuses it into the high speed camera (Basler, Pioneer piA640-210gm), capable of capturing images at 200 frames per second at full resolution of 640×480 pixels. The light passes through a red filter before entering the camera. The red filter allows only light from 600 to 650 nm to pass through it and the camera receives only the fluorescent signal.

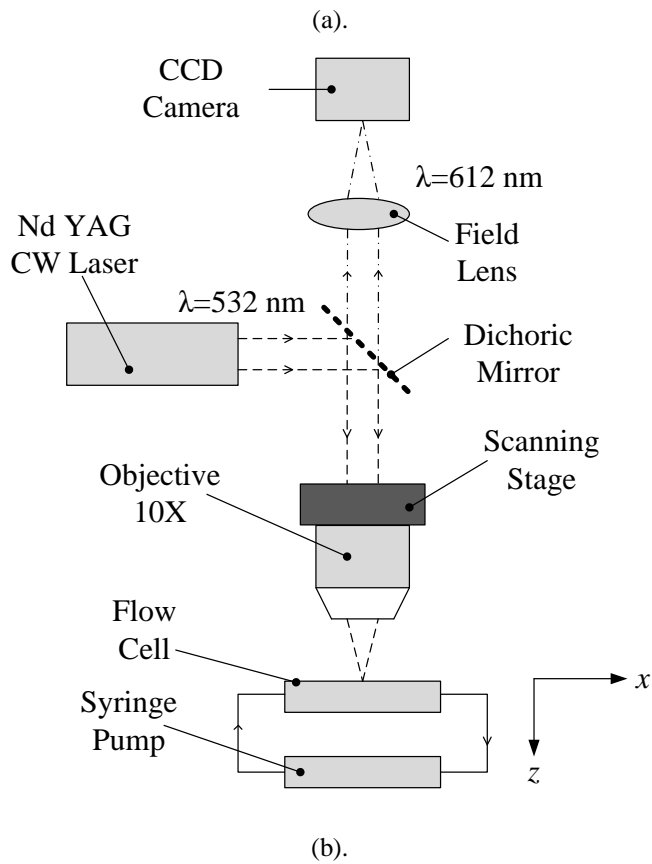
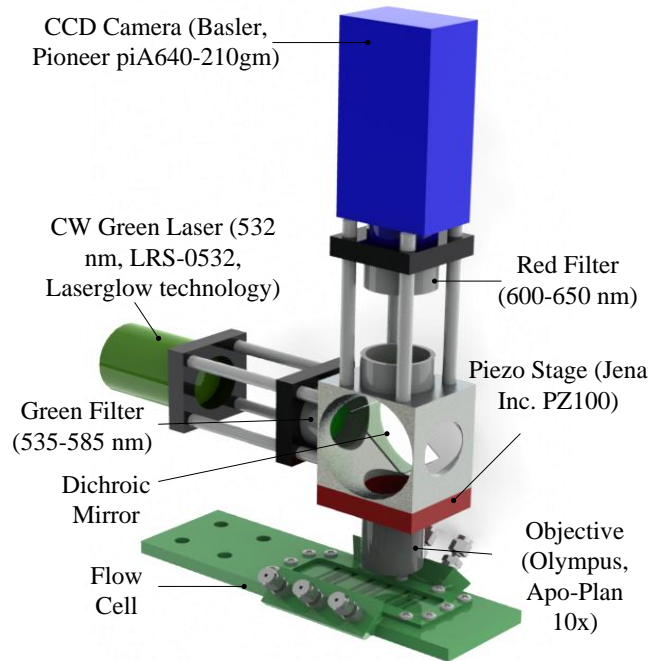


Figure 2-7 (a) The solid model of the scanning μ -PIV system. (b) Schematic of the scanning μ -PIV system.

The thickness of the focal plane for the objective is 8 μm , which means the objective can focus on any particle within the focal plane thickness. The objective is mounted on a peizo scanning stage (Piezosystem Jena Inc, PZ100). On applying electrical signal to the piezo stage it will be strained parallel to the z -axis and the objective can move in z -axis. The movement of the piezo stage can be controlled accurately by controlling the voltage, which is done using custom software (National Instruments, LabWindows CVI). The z -position of the stage can be accurately controlled and the maximum range is 100 μm . On moving the stage, the objective moves in the z -direction along with the stage this changes the focal plane of the lens. The lens can focus on different z -planes inside the porous media as far the optical access allows viewing. The control signal for the camera and the scanning stage are controlled though a custom software (National Instrument, Lab Windows CVI). A detailed discussion about the control signal with timing diagrams are provided in section 2.3.3. The specifications of the major components of the μ -PIV setup is given in Appendix B.

2.3.2 Field of View and Resolution

A 10x microscopic objective is used to get optimum field of view and resolution for the optical system. There is always a tradeoff between field of view and optical resolution of the system. With a higher magnification lens, the optical resolution increases but the field of view decreases. For the current optical system the field of view is $800 \times 600 \mu\text{m}$.

The diameter of the image of a fluorescent particle on the CCD chip of the camera is given by,

$$d_e = \left[\left\{ 2.44(M+1) \frac{\lambda}{2NA} \right\}^2 + M^2 d_{pf}^2 \right] \quad (2.1)$$

where, M is the magnification, d_{pf} is the diameter of the fluorescent particle, NA is the numerical aperture of the objective and λ is the wavelength of the emitted light from the fluorescent particle (Lindken et al. 2009). The diameter of the 2 μm fluorescent particle projected on the CCD chip, d_e , is 38.46 μm . The physical size of one pixel on the CCD chip of the camera is 7.4 μm , hence the image of a fluorescent particle is resolved over 5 pixels. This satisfies the condition that an image of a particle should be resolved at least over 2-3 pixels (Lindken et al. 2009). Projecting back the image of the particle on the flow field, the value of $\frac{d_e}{M}$, is 3.846 μm . The correlation peak can be determined within 1/10th of the particle image diameter (Prasad et al. 1992). Hence the diffraction limited resolution of the optical system is 386 nm.

2.3.3 Data Acquisition

The entire data acquisition system is controlled using custom software (Lab Window CVI, National Instruments). The software interacts with an acquisition hardware system which sends signal to the camera and the scanning peizo stage. The camera takes an image when it is triggered by a signal of 6.5 V. The illumination from the laser is continuous, so the camera takes a time series of images in the form of a movie. The scanning peizo stage can be sequenced with the camera using the software. The data acquisition for each of the experiment i.e, 2C2D velocity field and 3C3D velocity field is described below separately.

2.3.2.1 Data acquisition for 2C2D velocity field

For the 2C2D velocity field, measurements are taken only for two planes i.e, at $z = 25 \mu\text{m}$ and $z = 100 \mu\text{m}$. For focusing the objective at $z = 25 \mu\text{m}$ plane a constant voltage of 2.5 V was applied to the piezo. The constant voltage ensures that the objective remains focused at $z = 25 \mu\text{m}$ plane. The camera takes 1000 images at 200 frames per second. The camera operates at full resolution mode 640×480 pixels. Upon applying a constant voltage of 10 V the focal plane moves to $z = 100 \mu\text{m}$ plane location and 1000 images are taken by the camera. The timing diagrams are shown in Fig. 2-8. The camera transfers the images to a computer hard drive using a Gigabit Ethernet port output. For each region A, B, C and D , 1000 images are recorded for each plane i.e at $z = 25 \mu\text{m}$ and $z = 100 \mu\text{m}$. The time series images are used for processing and obtaining vector field.

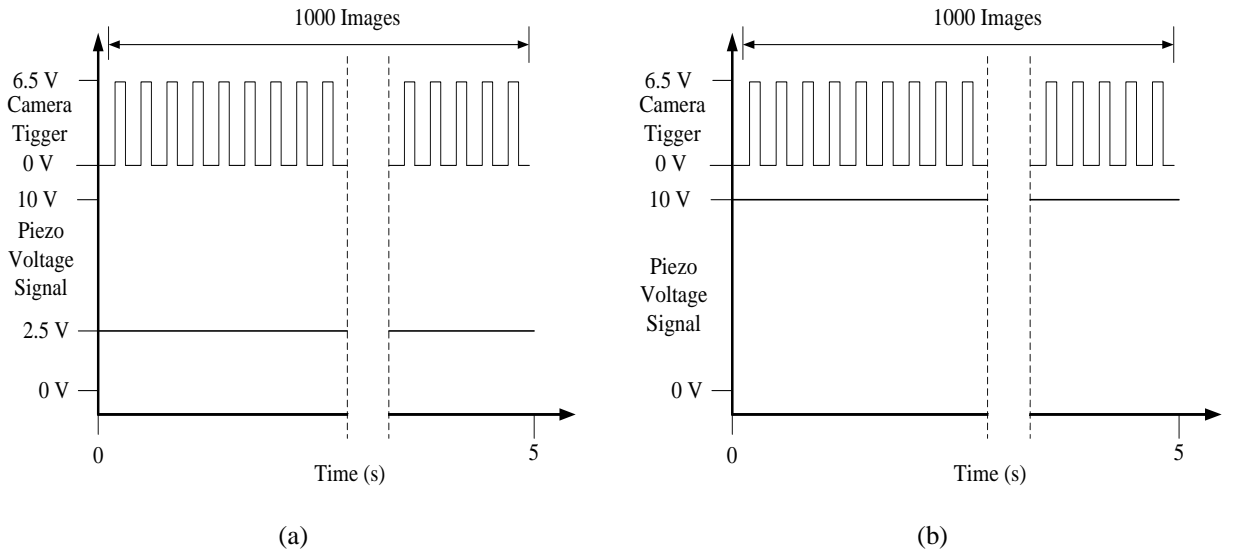


Figure 2-8 Timing diagram for the piezo and the camera. A constant voltage is applied to the piezo stage to fix the location of the focal plane. The camera takes 1000 images with 200 frames per second. (a) The focal plane is set at $z = 25 \mu\text{m}$. (b) The focal plane is set at $z = 100 \mu\text{m}$ plane

2.3.2.2 Data acquisition for the 3C3D velocity field

The 3C3D study was conducted using packed bed of 400 μm spheres. A saw tooth type voltage signal was given to the piezo and the camera was synchronized with the piezo as shown in Fig 2-9

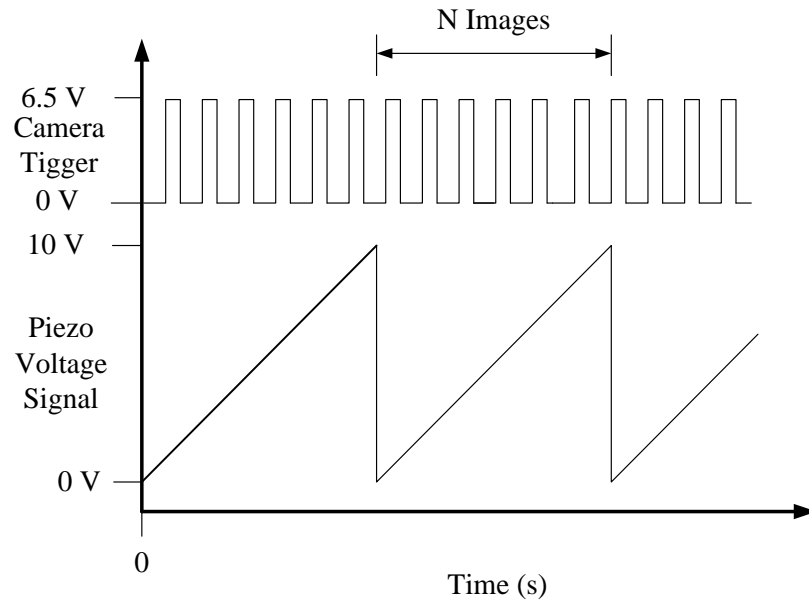


Figure 2-9 A timing diagram showing the control signals for synchronization of camera with the piezo stage for 3C3D velocity field measurement

The piezo scans through a distance of 100 μm in the z direction while the camera takes images. For the current experiment, 100 images were taken per scan. The frequency of the piezo was set to 2 Hz, which means there are two scans in one second. The porous media was scanned through $z = 0$ plane to $z = 100 \mu\text{m}$ plane. Five such scans were conducted to record 500 images. The images were later used for processing and vector field calculations.

There is a limitation with the data acquisition software which was observed and it was previously noted by Homeniuk (2009). The problem was with synchronizing the camera trigger with the piezo stage. The camera does not start taking images at the same

time as the peizo starts scanning. There is a time lag and the camera starts taking images at some point in the middle of first scan. However, the camera gets synchronized with the peizo from the next scan. The data obtained was manually observed and few images from the first scan which was deleted. Homeniuk et al. (2009) pointed out that the lag does not affect the accuracy of the system.

2.3.4 Calibration

The images obtained from the camera are in pixel space. This means that each particle image is spread over a few pixels on the CCD camera chip. The conversion of pixel space to real space is performed by calibrating the optical system. A micro calibration target (Max Levy Inc., Multipurpose Target) was used for this purpose. The calibration target has regular grid pattern with 100 μm spacing and the line width is 5 μm . Commercial image processing software (La Vision, Davis 7.4) was used for the calibration. The calibration target was placed at the same location as that of the flow cell and an image of the calibration target (Fig. 2-10) was taken and imported in the software's calibration wizard.

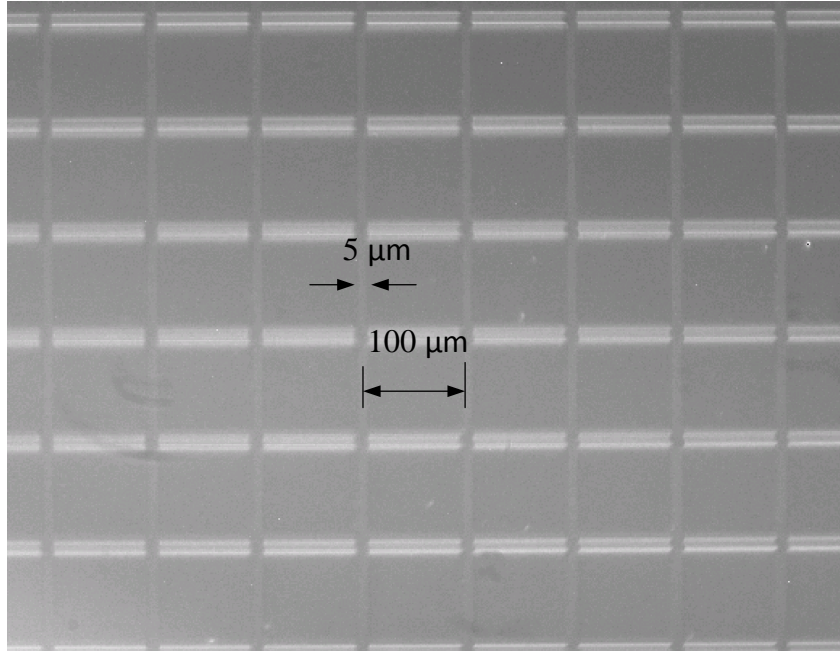
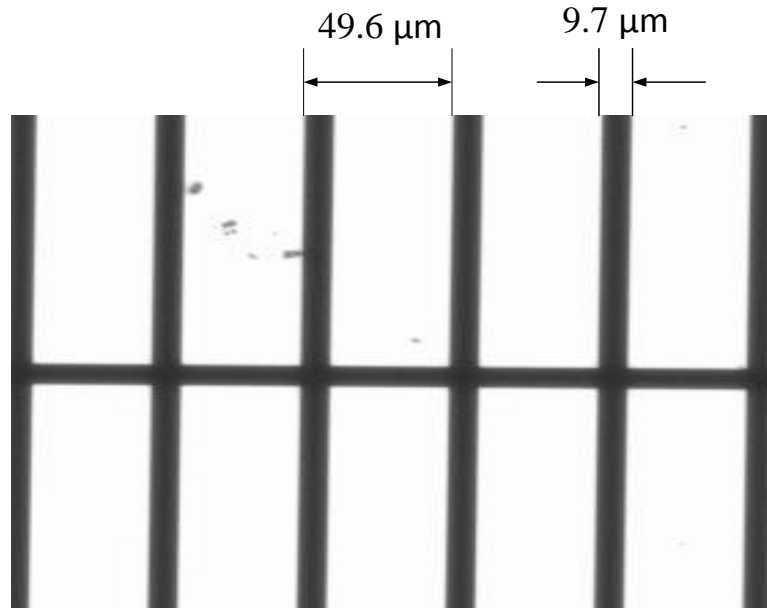


Figure 2-10 An image of the micro calibration target showing grid spacing and line width.

The distance between the two points on the grid which are 100 μm apart are shown in Fig. 2-10, is compared with the corresponding number of pixels. This process was repeated ten times by selecting random points on the grid which are 100 μm apart. The number of pixels corresponding to 100 μm is noted. The thickness of a line as shown in Fig. 2-10 is 5 μm and the corresponding number of pixels are recorded. This process was also repeated 10 times. The average value of number of pixels/ μm is noted which is the calibration factor. The calibration factor for the current optical system with a 10 x objective comes out to be 1.36 pixel/ μm . This conversion factor was used to convert pixel space to real space.

The calibration was verified by measuring a standard micro scale (Max Levy Inc, Multipurpose Target). The image of the standard scale is shown in Fig. 2-11.



. **Figure 2-11** An image of a standard scale used for verifying calibration factor.

The calibration was verified by measuring a standard micro scale (Max Levy Inc, Multipurpose Target). The image of the standard scale is shown in Fig. 2-11. The specified distance from the manufacturer, between two lines is $50 \mu\text{m}$ and the line width is $10 \mu\text{m}$. Using the calibration factor calculated from the calibration wizard, the distance between the lines comes out to be $49.6 \mu\text{m}$ and the line width comes out to be $9.7 \mu\text{m}$. The error in calibration comes out to be $0.4 \mu\text{m}$.

The method for calibration of the out of plane component of the camera involves a reconstruction technique used by Homenuick et al. (2009). This method involves taking images of same particles at different focal planes by using the scanning system. The out of plane coordinate of a particle is determined by finding out the focal plane corresponding to the maximum intensity of the particle. The maximum intensity occurs when the particle is in focus. Homenuick et al. (2009) found out the out of plane component by correlating the focal plane distance with the corresponding voltage applied

to the piezo at that instance. It was found out that the stage moves for 1 μm for every 0.1 V.

2.4 Image pre-processing

The pre-processing step involves removing noise from the raw images so that the fluorescent tracing particles can be clearly distinguished from the background. A commercial image processing software (LaVision, Davis 7.4) is used for image pre-processing. Figure 2-12(a) shows the glass spheres of 200 μm and the fluorescent particles of 2 μm flowing around it, which appear as bright white dots. The glass spheres are visible due to red fluorescent signal emitted by the out of focus particles. An inherent problem of flow measurement through packed bed of micro spheres is identified. The background fluorescent signal gets reflected in the glass sphere which creates lots of background noise; this makes it harder to identify the tracing particles compared to a simple micro channel experiment. An image pre-processing recipe was developed to significantly improve the signal to noise ratio. One of the major challenges was to remove the background noise and this was done by effective selection of pre-processing steps and the parameters. The same pre-processing recipe was used for the experiment on 3C3D velocity field with 400 μm glass spheres.

2.4.1 Subtract a sliding minimum

A raw image taken from the camera indicates regions of high intensity fluctuations arising due to background noise as shown in Fig. 2-12 (a). A sliding minimum subtraction algorithm reduces background noise significantly. The image of a single fluorescent particle is spread over 3-4 pixels. A 6×6 pixel window is selected to

perform the sliding minimum algorithm. The window size is selected bigger than the particle so that subtracting is not performed on the particle image. The algorithm finds out the minimum intensity within the window and subtracts it from the intensity at the center of the window. The center of the window then shifts to the next pixel location and the process is repeated. The effect of this image processing step is shown in Fig. 2-12 (b). The fluorescent particles appear brighter than the background image and the uneven intensity fluctuations were removed from the image.

2.4.2 Multiplication to increase intensity count

The next pre-processing step involves increasing the intensity value of the image. This was done by multiplying the intensity by a constant value of 25. This resulted in the intensity count of the fluorescent particles to be in the order of 7000 to 10,000 where as the intensity count of the background is 3500. This step helps in selecting the threshold value of image subtraction which is explained in the next step.

2.4.3 Subtract a constant value

A constant intensity value is subtracted from all the pixels in the image. The intensity value is chosen to be 5000 counts. Any pixel on the image which has intensity count less than 5000 is set to zero count. This process ensures that the background noise level is set to zero. The effect of this process is shown in Fig. 2-12 (c). The threshold value for subtraction is crucial because a high value will remove the background but there are chances of losing data. An image of a fluorescent particle is typically spread over 3-4 pixels. The brightest pixel has a count more than 5000 where as the neighboring pixel can have a count less than 5000. The algorithm can remove some pixels from the image

of the fluorescent particle. Fig 2-12 (e) shows some fluorescent particles which suffered from this and are spread over only one or two pixels. This problem was resolved using a linear filter as described below.

2.4.4 Linear smoothing filter

A linear Gaussian smoothing filter is used to convert images of the particles into smooth circular images as shown in Fig 2-12 (d). The Gaussian smoothing was performed over 3×3 pixels. The images of the particles which got truncated during subtraction process and are spread over less than 2 pixels are converted into smooth circular particles. Fig. 2-12(f) shows images of particles after Gaussian smoothing was performed. The particles are spread over 3×3 pixels and brightest pixel placed at the center. Particles of such shape can be easily identified by cross correlation algorithm performed during vector field calculation.

The effect of image pre-processing steps can be observed in Fig 2-13. The intensity plot for the raw image shown in Fig. 2-12 (a) is plotted in Fig. 2-13 (a). The intensity plot of the raw image shows background noise and the intensity of the fluorescent particles are swamped by the background noise. The intensity plot for Fig. 2-12 (d) is shown in Fig. 2-13 (b). The intensity plot in Fig. 2-13 (b) shows sharp peaks at the location of the fluorescent particles. Fig. 2-13 shows that the image pre-processing algorithm could successfully remove the background noise and has significantly increased signal to noise ratio.

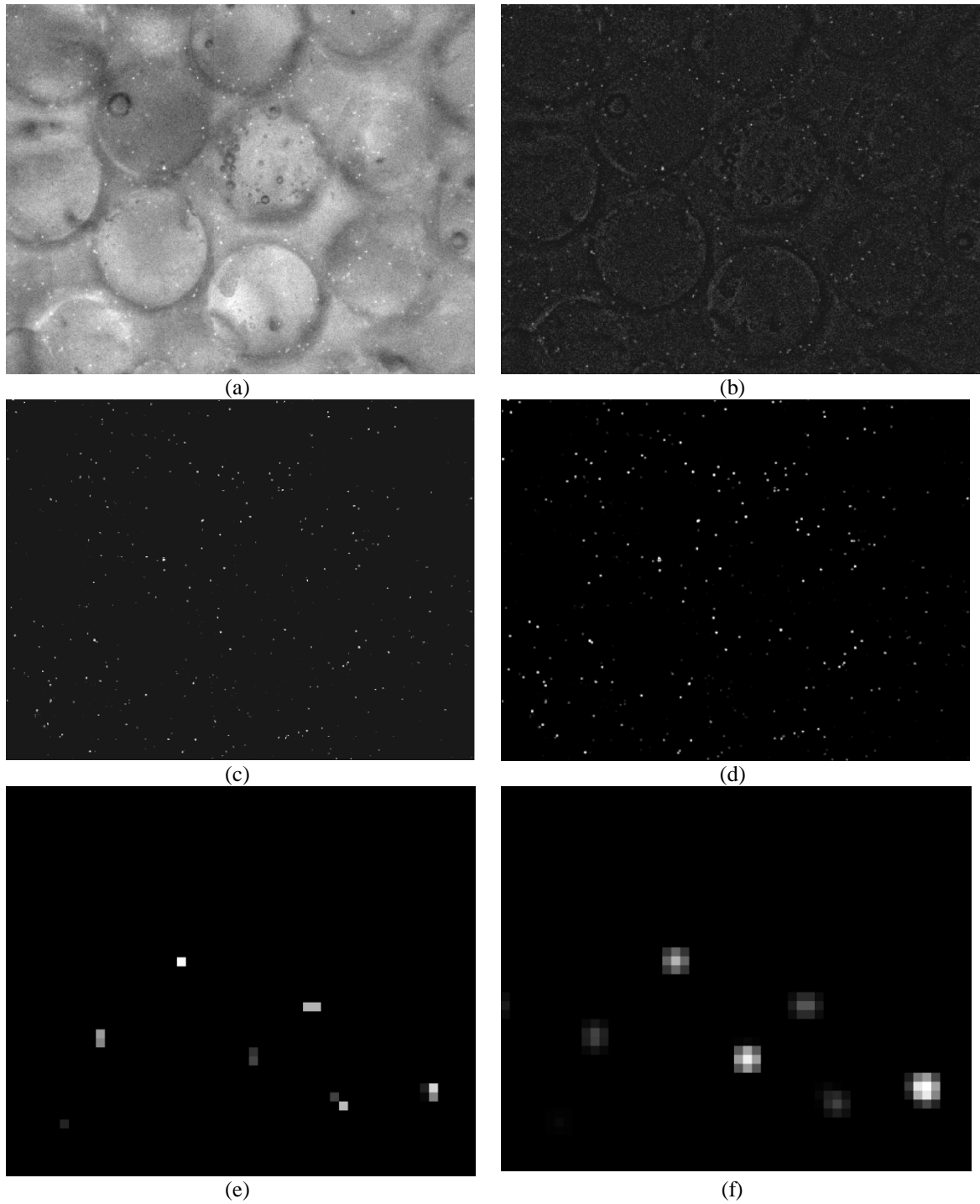
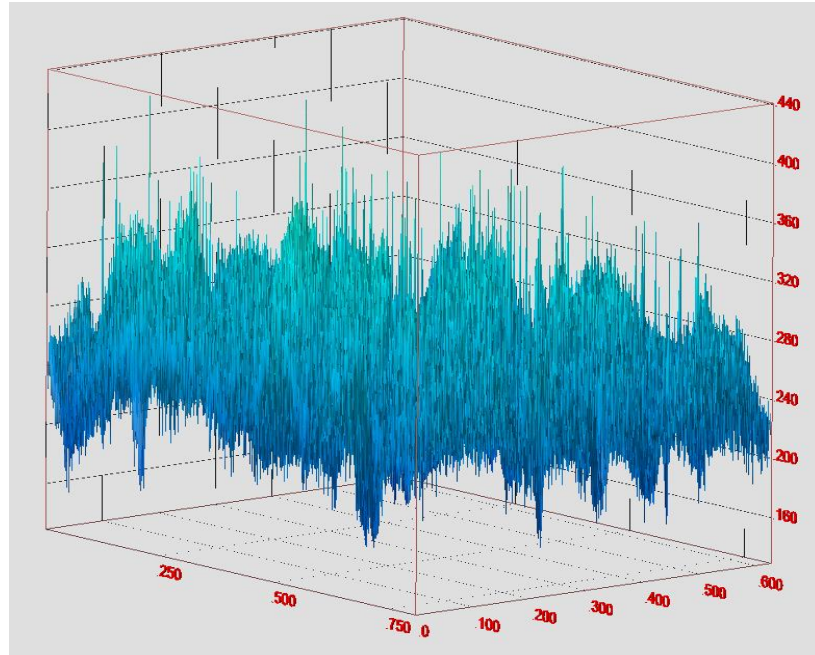
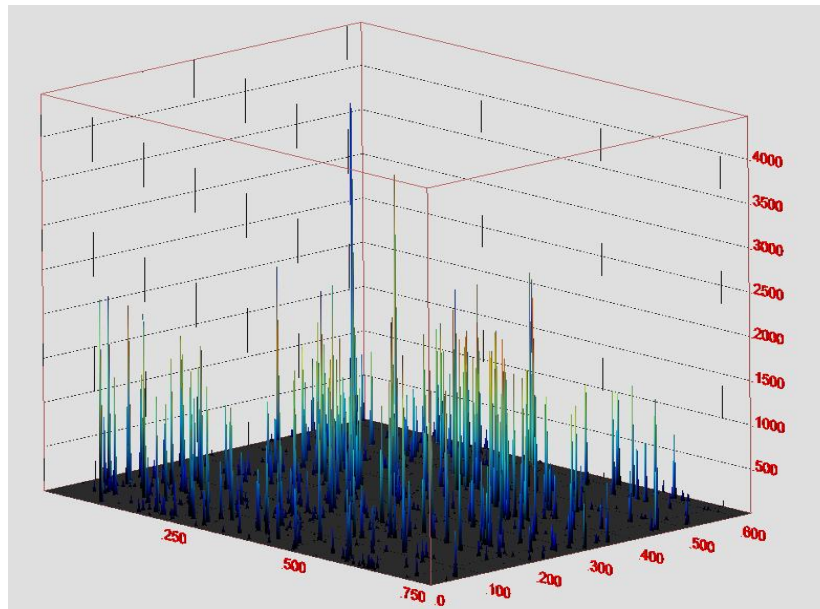


Figure 2-12. Image pre-processing steps used to identify the fluorescent tracing particle. (a) Raw image (b) Subtract sliding minimum over 6×6 pixels (c) Subtraction of constant intensity count (d) Linear smoothing filter 3×3 pixels (e) Shape of fluorescent particle (zoomed in) spread over 1-2 pixels (f) Shape of fluorescent particles (zoomed in) after linear smoothing over 3×3 pixels.



(a)



(b)

Figure 2-13 A comparison of intensity map before and after image pre-processing is shown. (a) The intensity map of the raw image shows lot of noise. The intensity of the particles are swamped by the background noise (b) The intensity map after image pre-processing shows sharp peaks at the location of the fluorescent particles

2.5 Vector field calculation

The pre-processed images are used for vector field calculation. Commercial software (LaVision, Davis 7.4) was used for calculation of the velocity field vectors. Separate techniques are used for 2C2D vector field calculation and 3C3D vector field calculation which have been discussed in this section. A hybrid PIV+PTV technique was used to obtain the 2C2D velocity field whereas the 3C3D velocity field is obtained by 3D cross correlation method.

2.5.1 2C2D vector field calculation

The time interval (Δt) between each image is 0.005 s as the camera took images at 200 frames per second. The 2C2D velocity field is studied with flow rates ranging from 40 $\mu\text{l}/\text{min}$ to 100 $\mu\text{l}/\text{min}$ in steps of 20 $\mu\text{l}/\text{min}$. With increase in flow rate the velocity of the particle increases within the porous media. The time series images are redistributed into double frame images as shown in Fig. 2-14.

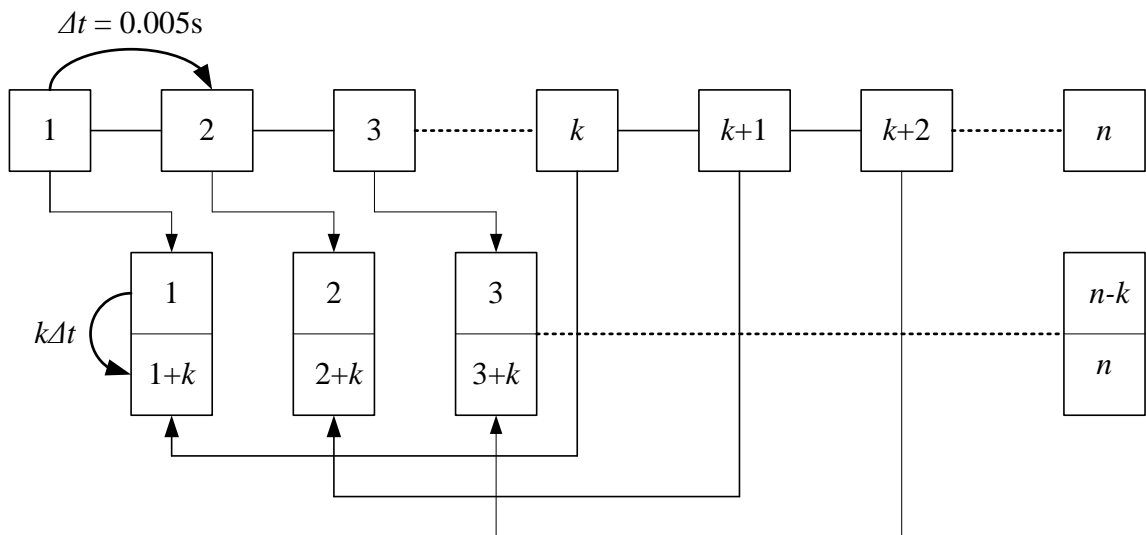


Figure 2-14 A schematic showing conversion of time series images into double frame images

Converting into double frame images ensures that the tracing particles travel sufficient distance in the time interval $k\Delta t$. The value of k used for processing each data set pertaining to a particular flow rate is given in Table 2-1. The displacement of the tracing particle between each image in a double frame is calculated using PIV+PTV algorithm. On dividing the displacement vector by $k\Delta t$, the instantaneous velocity is obtained.

Table 2-1 A summary of time interval between each image in a double frame image

Flow Rate (Q_s) ($\mu\text{l}/\text{min}$)	k	$k\Delta t$ (s)
40	5	0.0025
60	2	0.001
80	2	0.001
100	1	0.0005

A PIV algorithm correlates a group of particles within an interrogation window (Lindken et al. 2009). A PIV algorithm gives reliable results when particle seeding density is high (Theunissen 2003). The resolution of a PIV algorithm is limited by the size of the smallest interrogation window used. However, using a very small interrogation window can result in a particle moving out of the interrogation window. On the other hand a PTV algorithm tracks the displacement of each individual particle. A PTV algorithm works on correlating intensities of two individual particles and forming particle pairs for calculating the displacement. A comparison of PIV and PTV process is shown in Fig. 2-15. A PTV algorithm is known to produce reliable results when seeding density is low (Theunissen 2003). The inherent problem in PTV algorithm is that it can give

spurious results when seeding density is high or there is a high velocity gradient in the flow. The spurious vector field can occur due to false pairing of particles.

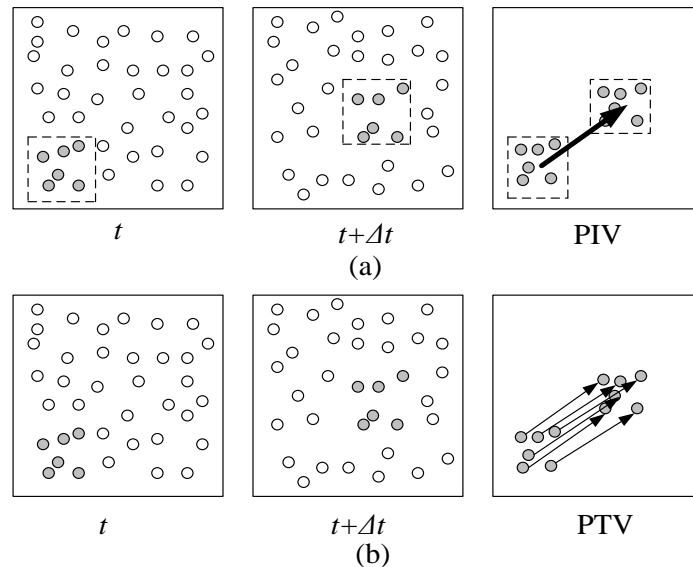


Figure 2-15 A schematic showing comparison of PIV and PTV process. (a) A PIV process correlates a group of particles in the interrogation window and calculates the displacement of a group of particles (b) A PTV algorithm finds out the displacement of each individual particle

A hybrid PIV+PTV scheme approach produces reliable vector field with an increase in spatial resolution compared to conventional PIV or PTV techniques (Scarano & Reithmuller 2000; Stanislas et al. 2005). The hybrid scheme approach works in two steps. The first step involves a conventional PIV algorithm, which determines the displacement of a group of particles within an interrogation window between two images in a double frame. The cross correlation is performed in two passes, in the first pass, the interrogation window size was 64×64 pixels with 50% overlap between the interrogation

windows, and the second pass was performed with 32×32 interrogation window with 60 % overlap. The window sizes were selected based on analysis of correlation map.

The second step involves tracking the displacement of individual particles. A particle diameter of 2-6 pixel is specified to identify an individual particle. An intensity threshold value of 300 counts is selected since the intensity of any particle is higher than 300 counts and anything below 300 counts is considered to be noise. The intensity of the particle image is fitted to a Gaussian distribution and the location of the peak corresponds to the center of the particle. Once the center of a particle is determined, an interrogation window of size 8×8 pixels is placed such that the particle center coincides with the center of the interrogation window. The interrogation window size is selected so that a single particle is inscribed in the interrogation window. The predicted value of displacement from the PIV algorithm gives an initial indication of the particle location in the next frame. This helps in avoiding false pairing of particles by reducing particle search and also increases the accuracy of the process. The interrogation window is shifted to the next frame based on this prediction. An individual particle correlation is performed and a displacement vector is obtained. The displacement vector is divided by the time interval ($k\Delta t$) to obtain velocity vector. A combined PIV and PTV technique is known to produce results with resolution of $1.2 \text{ pixel} \times 1.2 \text{ pixel}$ (Keane et al. 1995; Takehara et al. 2000)

There are $n-k$ double frame images on which the PIV + PTV vector field calculation is carried out. This resulted in $n-k$ instantaneous vector field. The instantaneous velocity field is sparse and there are only few vectors. One such instantaneous vector field for region B close to the wall at $z = 25 \text{ }\mu\text{m}$ is shown in Fig.2-

16. The magnitudes of the vectors are denoted by their color. The vectors are overlaid on top of the raw image showing the packed bed of spheres. The color bar shows different colors corresponding to the magnitude of the vectors denoted by $|V|$.

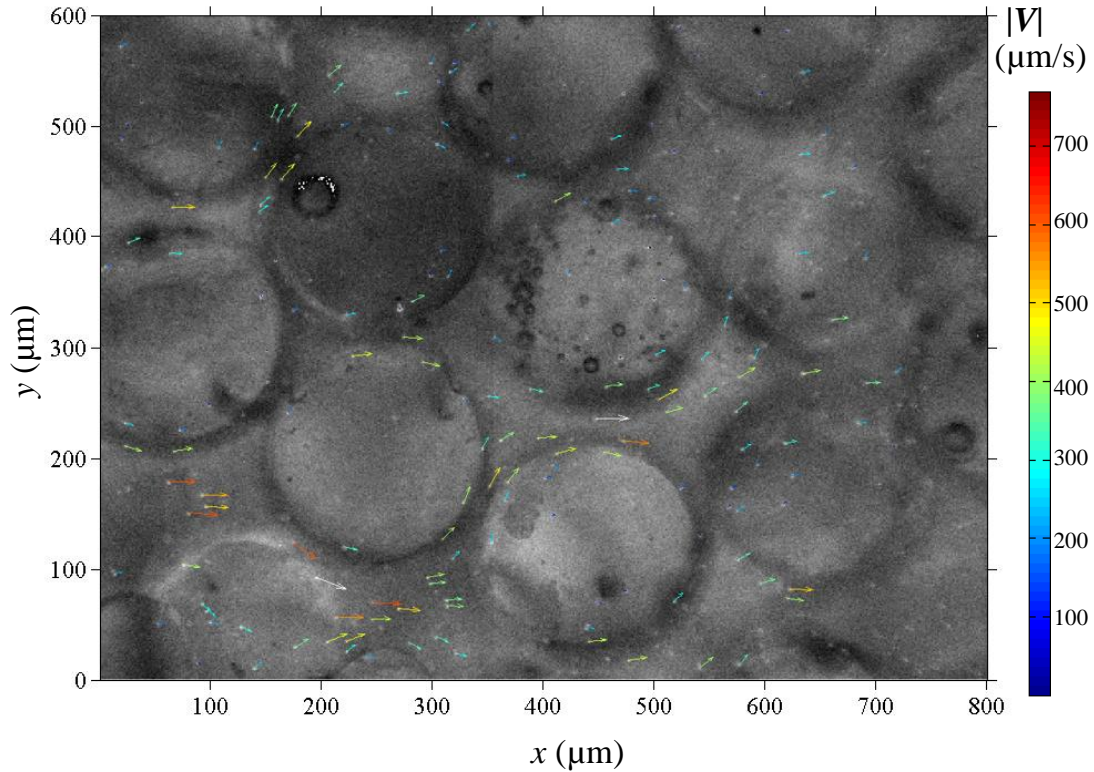


Figure 2-16 Instantaneous velocity field obtained after processing a double frame image. The vectors are overlaid on top of the raw image of 200 μm glass spheres. The vector field obtained is for Region B with focal plane location at $z = 25 \mu\text{m}$ and $Q_s = 80 \mu\text{l}/\text{min}$

2.5.2 Vector field post processing

The flow is laminar and steady with time, so the spatial variation of flow field is important. The $n-k$ instantaneous velocity fields are accumulated on a single frame to obtain a dense vector field. The accumulation process involves an averaging technique. If multiple vectors appear on the same pixel during the accumulation process, the average

magnitude depending on number of vectors on that pixel is considered. However, the chances of multiple vectors appearing on the same pixel is low and in most of the cases self averaging was done which is basically accumulation. The accumulation was done over 998 instantaneous velocity fields. A dense vector field with 77,146 vectors is obtained as shown in Fig. 2-17.

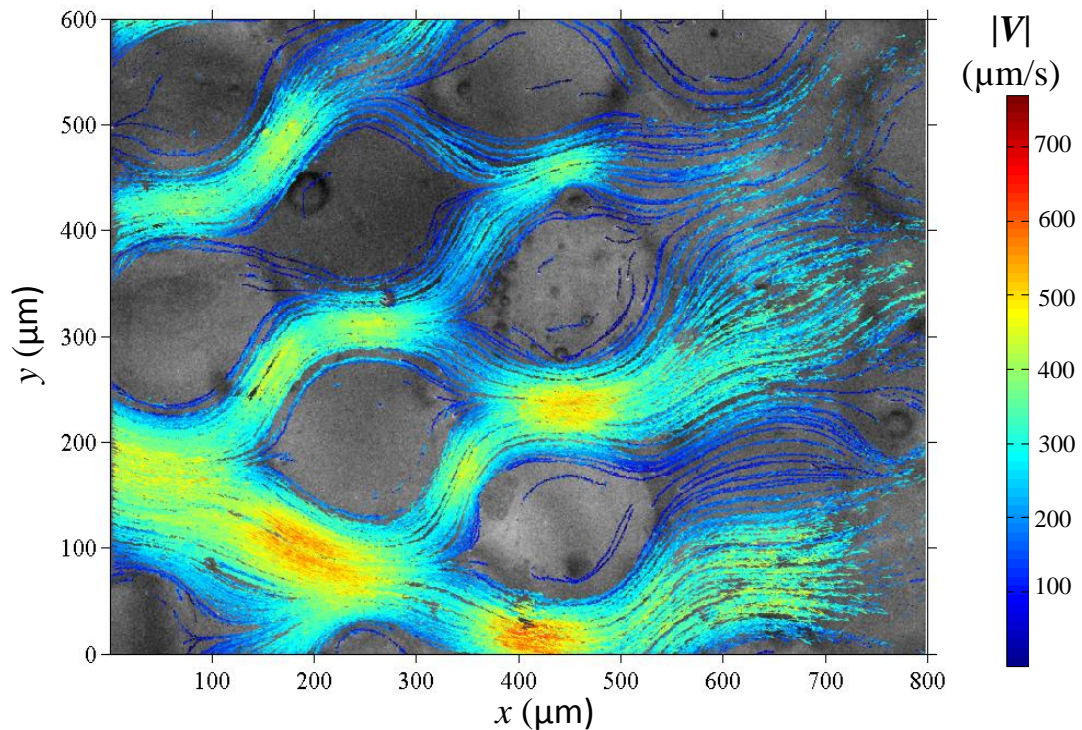


Figure 2-17 A dense vector field is obtained after accumulating the instantaneous vector fields on to a single image.

The velocity field obtained has few spurious vectors which are believed to have originated from some false correlation. The spurious vectors are removed using a non-linear median filter. The velocity vector \mathbf{V} has two components u and v in the x and y direction respectively. Let u_0 represents the velocity value at location (x_0, y_0) . The algorithm calculates the median of velocity values in a 3×3 grid centered around (x_0, y_0) . The algorithm also calculates deviation of the neighboring vectors based on Equation 2.2.

$$u_{dev} = \sqrt{\frac{1}{N} \sum_{j=1}^N (u_j - u_{median})^2} \quad (2.2)$$

where, u_{dev} is the deviation of the neighboring vectors, u_j is the value of a neighboring vectors around u_0 , N is the number of neighboring vectors. Similarly, the median and deviation for v is calculated and are denoted by v_{median} and v_{dev} respectively The vector V at location (x_0, y_0) is considered spurious and is removed if either of the conditions mentioned below applies

$$u_0 - u_{median} > 1.5 \times u_{dev}$$

OR

$$v_0 - v_{median} > 1.5 \times v_{dev}$$

After removing the spurious vectors, the velocity data is distributed on to a regular grid of 8×8 pixels as shown in Fig.2-18. Each vector on the grid is obtained by linearly interpolating over 12 neighboring vectors around it. The vectors are separated from each other by a distance of 8 pixels. This results in a vector spacing of $10.9 \mu\text{m} \times 10.9 \mu\text{m}$.

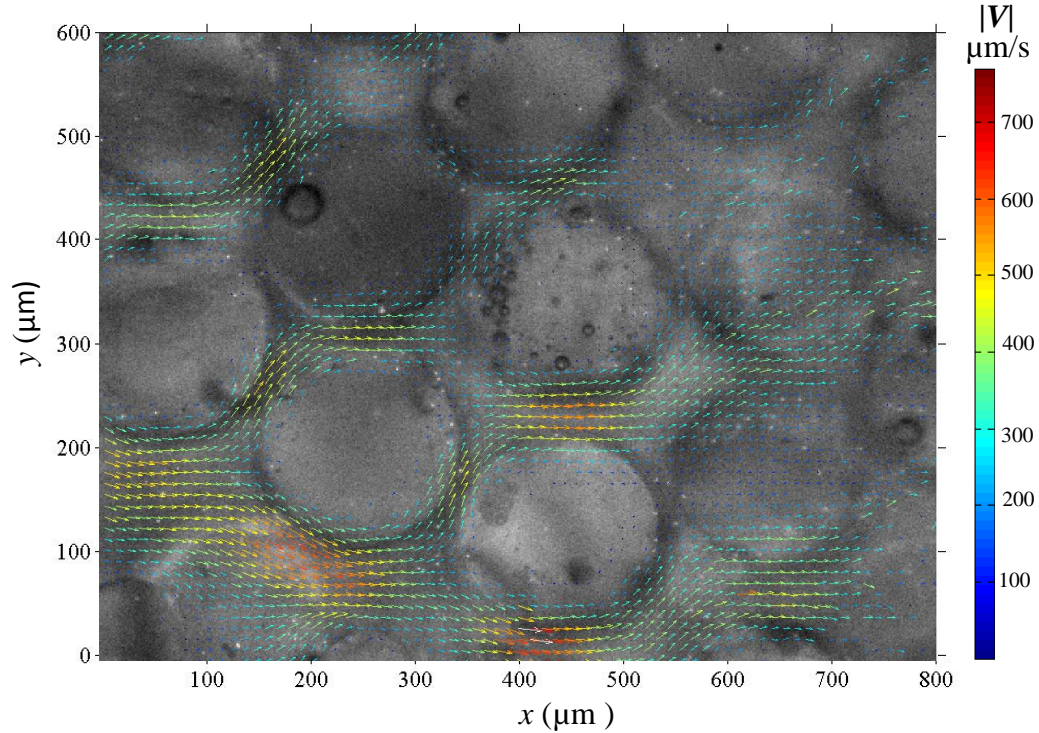


Figure 2-18 The vectors obtained after accumulation are distributed on to a regular grid of 8×8 pixels

2.5.3 3C3D vector field calculation

The images obtained from 2 consecutive scans were used to obtain an instantaneous 3C3D velocity field. 100 images were obtained in each scan and each image is separated by a distance of $1 \mu\text{m}$ in the z direction. Each scan generates a volume of data and two such volumes of data are used to obtain the velocity field. The schematic shown in Fig. 2-19 shows 100 images were taken in each scan. Volume I contains data of particles distributed in 3D space obtained from the first scan at $t=t$. Similarly, Volume II contains position of particles at $t=t+\Delta t$. The time interval Δt between each scan is 0.5 s. The volumes are cross correlated using a 3D cross correlation algorithm to obtain the displacement of the particles in 3D space. The displacement vector is divided by Δt to obtain the velocity vector. The velocity vector has three components denoted by u , v , and w .

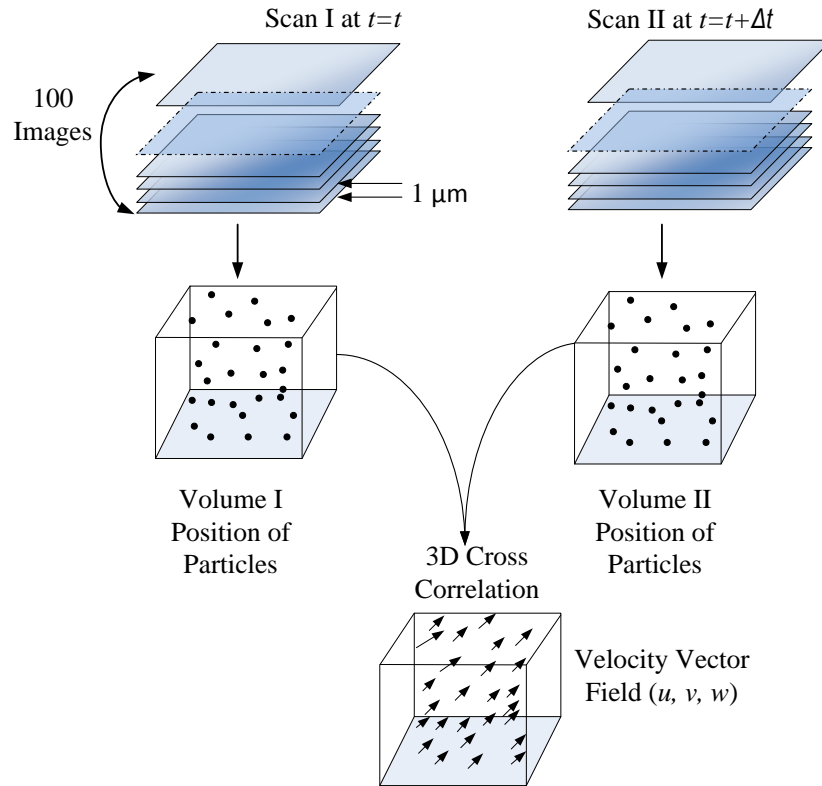


Figure 2-19. A schematic showing 100 images were taken in one scan to generate a volume of data. Two such consecutive volumes of data are cross correlated to obtain the 3C3D velocity field

..

The cross correlation algorithm was performed using two passes. The first pass was performed with an interrogation window of $128 \times 128 \times 32$ pixels with a 75% overlap and the second pass was performed with $64 \times 64 \times 24$ pixels with 60% overlap. A 3C3D velocity field was obtained inside a pore as shown in Fig. 2-20. The in-plane components of velocities i.e., u and v are shown by vector arrows. The magnitude of the vector is represented by the length of the arrow. The out of plane component of velocity, w , is represented by the color map on the background. The color bar shows the value of w . The velocity plot shown in Fig. 2-20 is close to the mid plane location of first layer of $400 \mu\text{m}$ spheres.

The vectors obtained contain some spurious vectors which were removed using a non-linear median filter as discussed in section 2.5.2. The non-linear filter described in section 2.5.2 is for a two dimensional case. The algorithm remains same for the three dimensional velocity fields with an additional check on w component of velocity. The vector \mathbf{V} at location (x_0, y_0, z_0) is considered spurious and is removed if either of the conditions mentioned below applies

$$u_0 - u_{\text{median}} > 1.5 \times u_{dev}$$

OR

$$v_0 - v_{\text{median}} > 1.5 \times v_{dev}$$

OR

$$w_0 - w_{\text{median}} > 1.5 \times w_{dev}$$

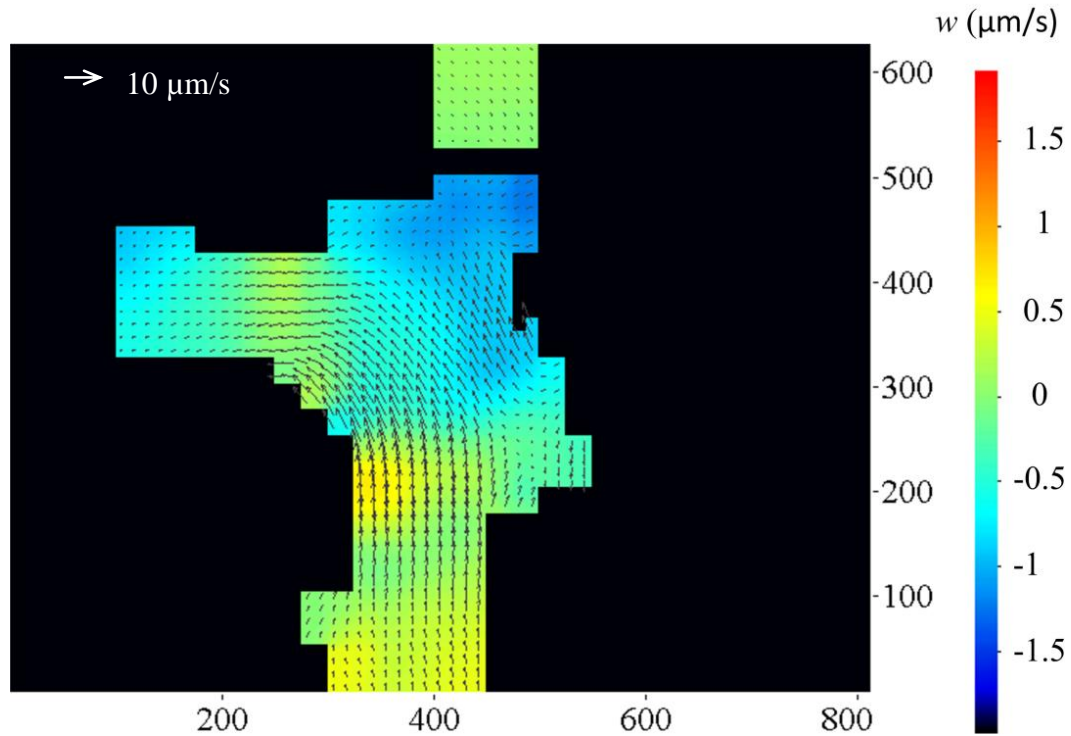


Figure 2-20. The instantaneous 3C3D velocity field is shown. The in-plane velocity components are shown by vector arrows. The length of the arrow denotes the magnitude of the vector. A reference vector of magnitude $10 \mu\text{m/s}$ is shown on the figure. The out of plane component is shown by the background color map and the values of w are indicated by the color bar.

2.6 Errors

The errors in measurement can occur if the tracing particles do not follow the fluid motion faithfully. This could happen due to inertia of the particles and Brownian motion of the particles. Due to inertia of the tracing particles, they can react to change in fluid motion after a certain time interval known as the relaxation time, τ . The relaxation time, τ can be calculated using Equation 2.3 (Lindken et al. 2009)

$$\tau = \frac{d_{pf}^2 \rho_p}{18\mu} \quad (2.3)$$

where, ρ_p is the density of the particle and μ is the viscosity of the fluid. The relaxation time is found to be 2×10^{-7} s for the fluorescent particles of size 2 μm . The time scale for the flow can be calculated from the ratio of diameter of the particle to the average velocity. The time scale for the flow is in the order of 10^{-3} s, which is several orders higher than the relaxation time. The calculation shows that the particles react to the change of fluid motion instantly.

The error due to Brownian motion needs to be quantified (Santiago et al. 1998). The mean square distance travelled by the particle due to Brownian motion is given by

$$\langle s^2 \rangle = 2\mathcal{D} \Delta t \quad (2.4)$$

where, $\langle s^2 \rangle$ is the temporal average of the square of displacement, \mathcal{D} is the diffusion coefficient and Δt is the time interval between images. The diffusion coefficient can be found out from the classical Einstein equation:

$$\mathcal{D} = \frac{\kappa T}{3\pi\mu d_p} \quad (2.5)$$

where, κ is the Boltzmann constant, T is the absolute temperature of the fluid, μ is the dynamic viscosity of the fluid and d_p is the diameter of the particle. If the particles faithfully follow the fluid velocity then the displacement of the particle is

$$\Delta x = |\bar{\mathbf{V}}| \Delta t \quad (2.6)$$

where, $|\bar{V}|$ is the average bulk fluid velocity and Δt is the time interval. The relative error, ε_b , due to Brownian motion can be estimated by

$$\varepsilon_b = \frac{\langle s^2 \rangle^{\frac{1}{2}}}{\Delta x} = \frac{1}{|\bar{V}|} \sqrt{\frac{2\mathcal{D}}{\Delta t}} \quad (2.7)$$

The average flow velocity for the present study is $|\bar{V}| \sim 200 \mu\text{m/s}$, viscosity $\mu = 0.001 \text{ kg/m-s}$ for water and the experiments are conducted at room temperature $T=298 \text{ K}$. The relative error due to Brownian motion is calculated using the above values and is found to be 4.7 %. The error calculated is for a single particle. Since the motion of the particles are random and it can happen in all directions the final error in velocity field is much lower than the estimated error. If there are N particles in the interrogation window and each particle contributes to the random error then statistically the error for velocity measurement for N particles is $\frac{\varepsilon_b}{\sqrt{N}}$. There are 4 particles in the interrogation window and two consecutive images are used for correlation, so $N = 8$. The total error due to Brownian motion is 0.6 %. It can be concluded that the error in velocity field due to Brownian motion is not significant and can be neglected.

Another type of error in the present study is calibration error. A micro calibration target was used to calibrate the in plane components of velocity. An *in situ* calibration involves placing the calibration target inside the flow cell. This was not possible due to lack of access and the size of the calibration target was not small enough to fit inside the

flow cell. An *in situ* calibration is more accurate as it takes care of the apparent size of an image due to refraction from the glass and the fluid. The calibration for the present study may suffer from this, which could lead to some error in calculation of the magnitude of the velocity field. However, this error does not affect the velocity trends or the relative comparison of velocity fields at different regions with different flow rates. The focal plane thickness of the lens can affect the calibration of the out of plane coordinate. The scanning system may suffer due to inertia of the piezo stage. The piezo stage may continue to move for certain distance due to its inertia. The accuracy and repeatability of the present scanning system is quantified by Homeniuk et al. (2008).

2.7 Summary

The experimental methods and the techniques used in the present study have been described in details. The image processing algorithms used for enhancing signal to noise ratio was studied. The velocity field calculations for 2C2D flow measurements and 3C3D measurements are explained separately. The algorithms used were successful in obtaining velocity field for each of the study.

CHAPTER 3: RESULTS AND DISCUSSIONS PERTAINING TO 2C2D VELOCITY FIELD MEASUREMENT.

3.1 Introduction

In this chapter a detailed discussion of the velocity fields within the micro porous media is carried out. The velocity plots at different regions within the micro-porous media are compared. The velocity fields at different planes close to the wall and mid plane location of first layer of spheres are studied. A quantitative comparison of magnitude of average velocity field at relatively large pores and narrow pores is carried out. Probability density functions (pdf) are used to study the behavior of transverse and longitudinal velocity fields. The effect of Reynolds number on the velocity profiles are also addressed in this chapter. The velocity fields are compared with available literature which includes numerical and experimental work.

3.2 Velocity field at different regions

Raw images of 200 μm glass spheres at different spatial locations are shown in Fig 3-1. The heterogeneity in the micro porous media is captured by identifying four regions named R1, R2, R3 and R4, as denoted by Fig. 3-1 (a), (b), (c) and (d) respectively. Flow through each of these regions is studied at different flow rates ranging from 40 $\mu\text{l}/\text{min}$ through 100 $\mu\text{l}/\text{min}$ at steps of 20 $\mu\text{l}/\text{min}$. Experiments are conducted at two different planes: close to the wall, i.e., at $z = 25 \mu\text{m}$ and at mid plane of the first layer

of spheres, i.e., at $z = 100 \mu\text{m}$ as shown in Fig.2-4. The flow behavior at two different planes is quantified and a comparative study was done. A few representative locations within the packed porous bed denoted by L1, L2, L3 and L4, shown in Fig. 3-1, are selected and the velocity profile is studied at these locations. The regions L1 and L2, as shown in Fig. 3-1 (a) and Fig. 3-1 (b) respectively, represents narrow pore region between the two spheres. The relatively two big pores are denoted by locations marked as L3 and L4 in Fig. 3-1 (d).

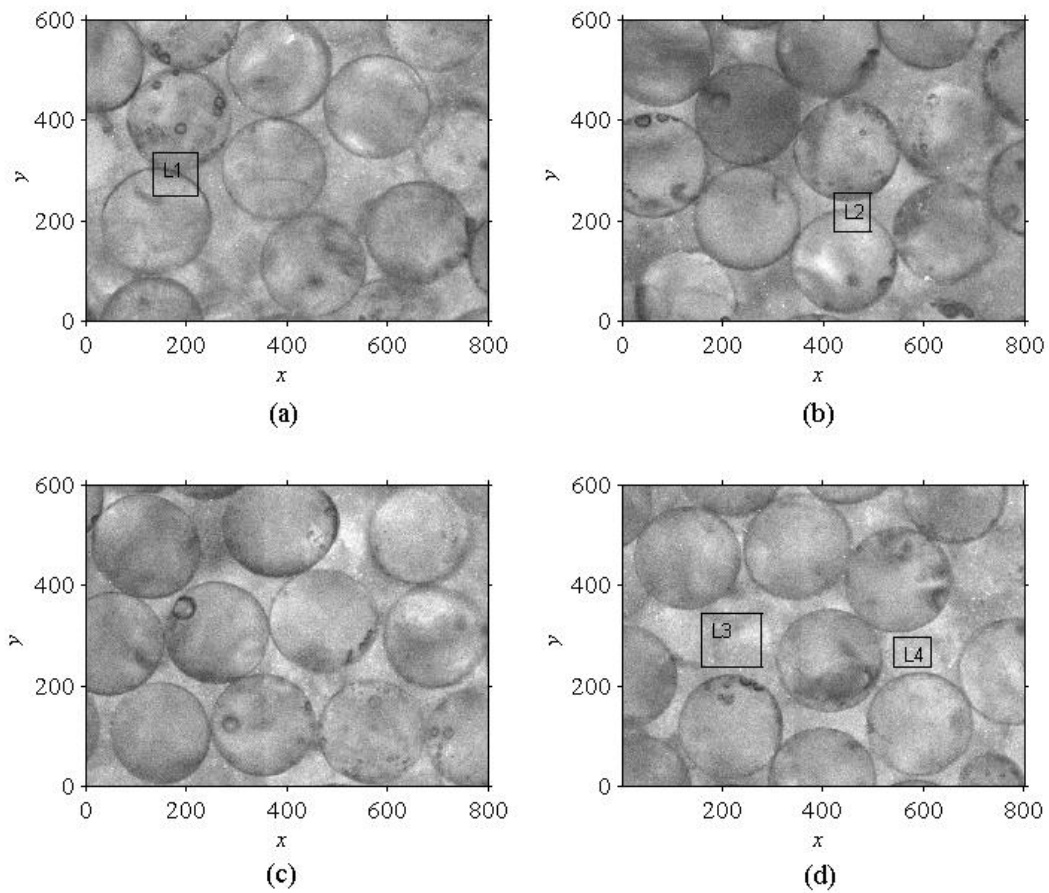


Figure 3-1 The pore structure at different regions is shown, each region is $800 \mu\text{m} \times 600 \mu\text{m}$. (a) Region R1 (b) Region R2 (c) Region R3 and (d) Region R4..

The 2C2D velocity fields processed and calculated with Davis 7.4 are imported in Matlab (Mathworks, R2010 B) for data handling and plotting. Some of the symbols

commonly used in the results and discussions are defined here. $|\mathbf{V}_i|$ denotes the magnitude of velocity vector, where the subscript $i = 1, 2, 3, 4$ represents velocity at flow rates of 40, 60, 80 and 100 $\mu\text{l}/\text{min}$, respectively. The velocity field, \mathbf{V}_i , has two components, i.e., the x and y components denoted by u_i and v_i , respectively. The average vector field for the entire region in space is calculated by

$$|\overline{\mathbf{V}}_i| = \frac{\sum_{j=1}^N |\mathbf{V}_{ij}|}{N} \quad (3.1)$$

where, \mathbf{V}_i denotes the velocity field at a spatial location for a particular flow rate denoted by i , the counter j denotes the number of vectors in a given region and N is the total number of velocity vector in a region.

The 2C2D velocity field for inlet flow rates ranging from 40 $\mu\text{l}/\text{min}$ to 100 $\mu\text{l}/\text{min}$ is shown in Fig 3-2 through Fig. 3-5. Each figure has a subplot which shows the 2C2D velocity field at different z planes. The subplots denoted by (a), shows velocity field close to the wall at $z = 25 \mu\text{m}$ and the subplot denoted by (b), shows velocity field at the mid plane location of first layer of spheres i.e., $z = 100 \mu\text{m}$. The magnitude of velocity, $|\mathbf{V}_i|$, is denoted by color maps and the vectors are overlaid on top of the color map. The same velocity scale denoted by a common color bar is used for each subplot representing a particular focal plane. A common color map can be used to compare the velocity fields at different regions for a particular flow rate and for a focal plane location.

The velocity field at the narrow pore region between the spheres is observed to be higher than the big pore region. Cross flow patterns have been observed in regions denoted by R1, R2 and R4 where as in region R3, capillary like flow pattern is observed as shown in Fig. 3-2 through Fig 3.5. In region R3, as shown in Fig. 3-1 (c), the spheres

are arranged in layers and the fluid flows through the narrow capillary pore structure between the layers. The velocity field observed close to the wall, denoted by Fig 3-2 (a) through 3-5 (a), shows evidence of fluid flowing over the spheres. The spheres are tangentially touching the glass slide so at $z = 25 \mu\text{m}$ plane, the fluid gets a chance to flow over the spheres. At the mid plane location, denoted by subplots (b) velocity vectors are observed only in the pore region. The edges of the spheres appear to be sharp and there is no evidence of flow over the spheres as shown in Fig. 3-2 (b) through Fig. 3-5 (b).

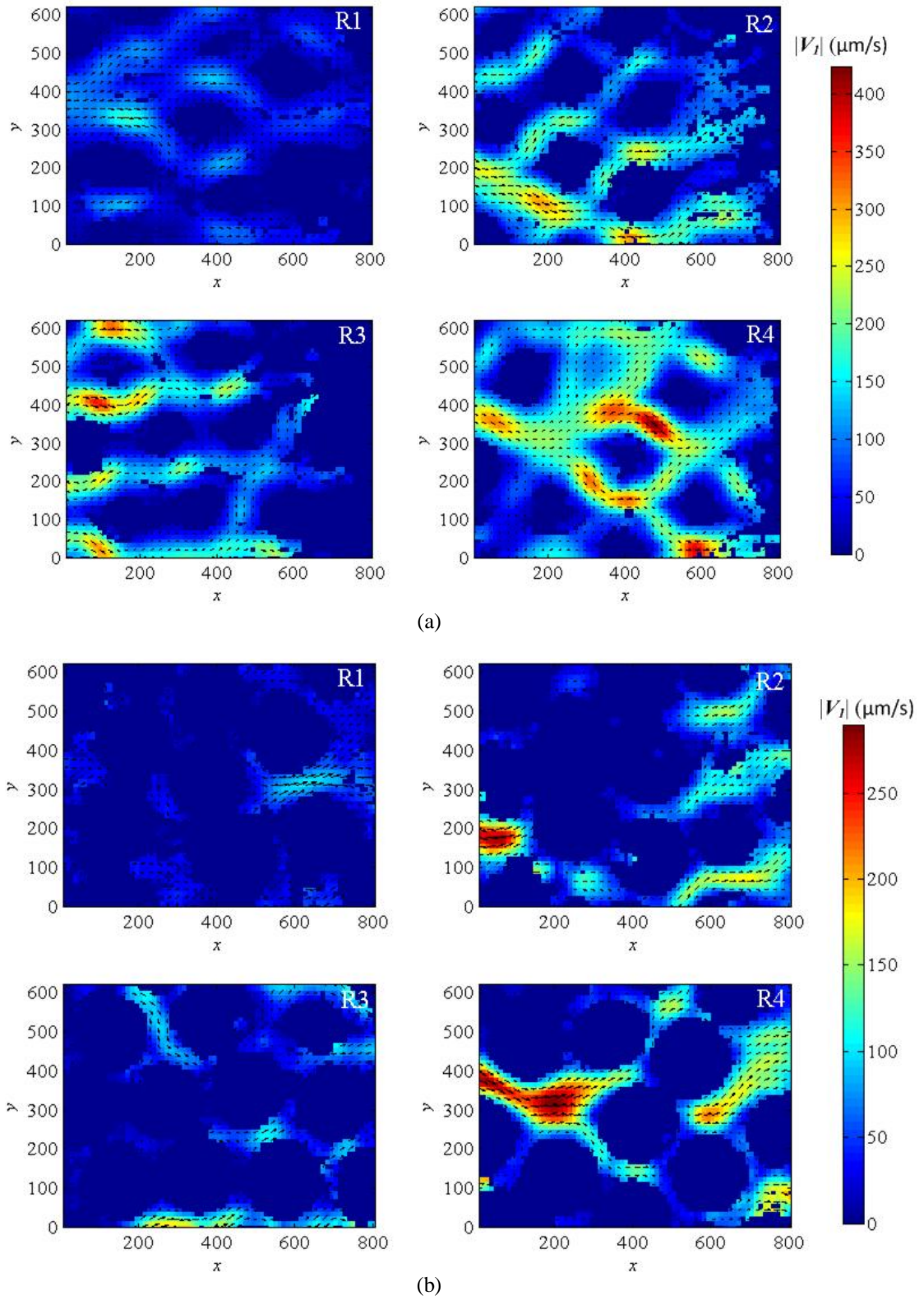


Figure 3-2 Velocity plots for $Q_s = 40 \mu\text{l}/\text{min}$. The color map shows the magnitude of velocity. (a) Close to the wall at $z = 25 \mu\text{m}$ (b) Mid plane location of first layer of spheres at $z = 100 \mu\text{m}$.

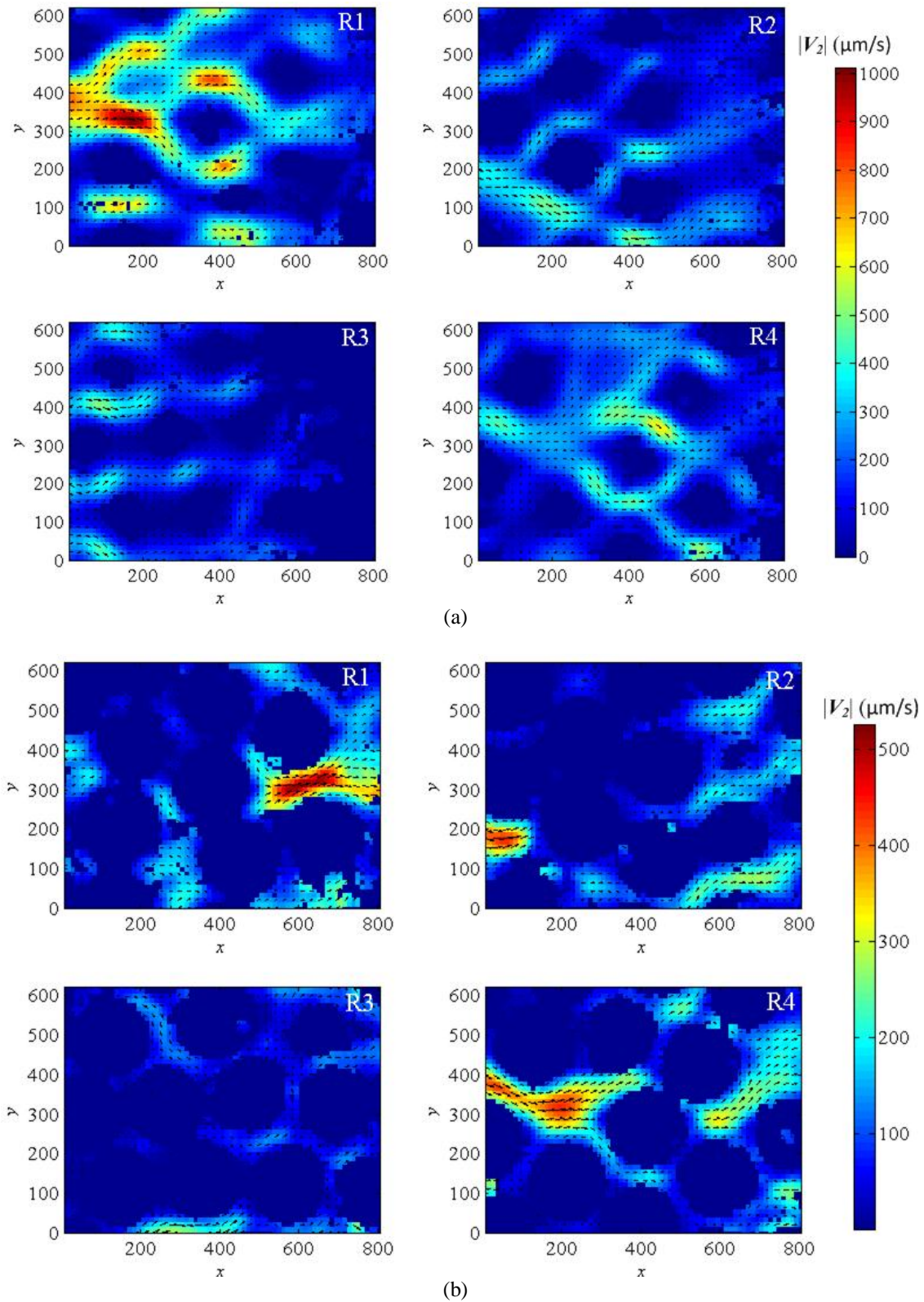


Figure 3-3 Velocity plots for $Q_s = 60 \mu\text{l}/\text{min}$. The color map shows the magnitude of velocity. (a) Close to the wall at $z = 25 \mu\text{m}$ (b) Mid plane location of first layer of spheres at $z = 100 \mu\text{m}$

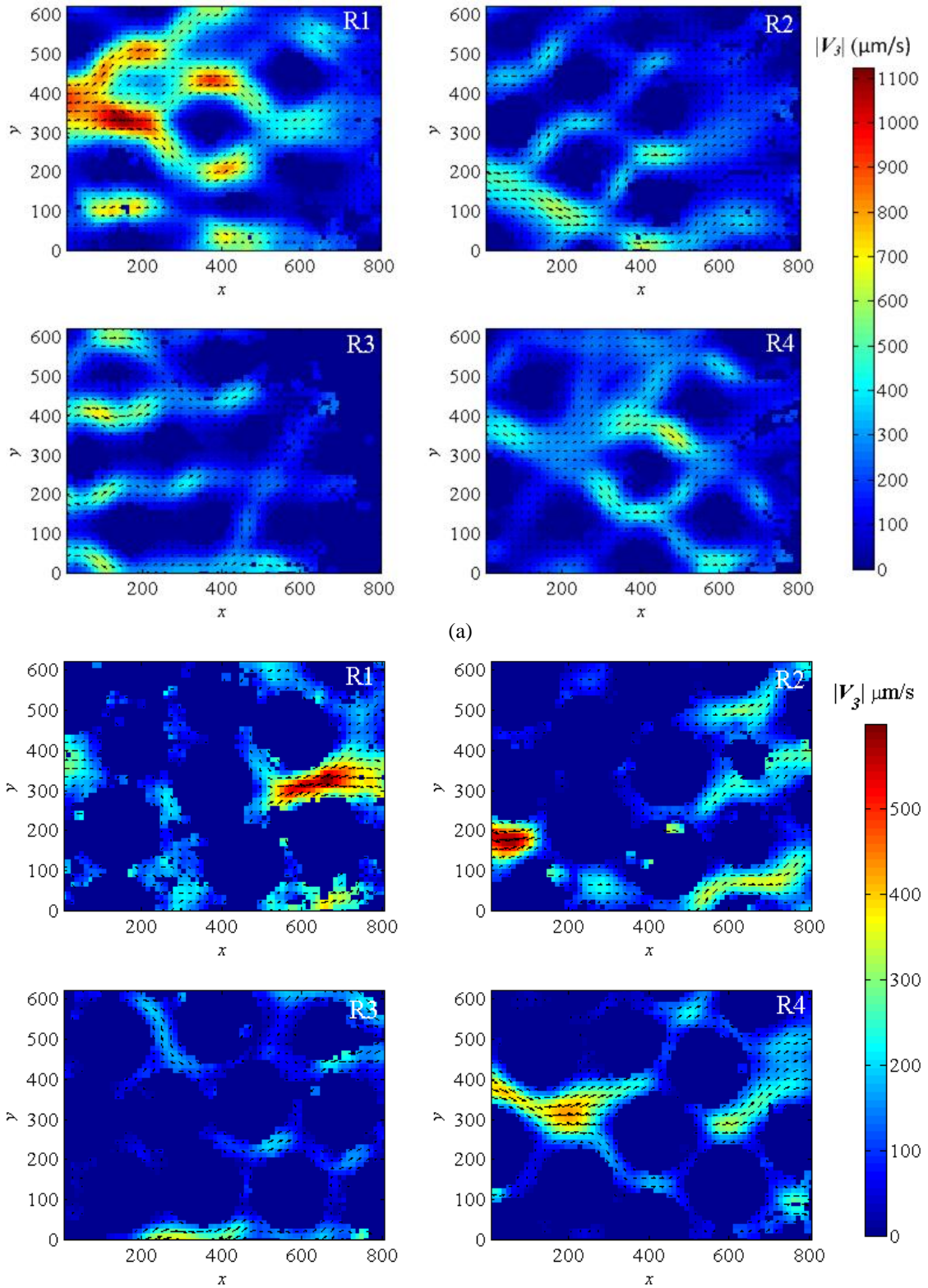
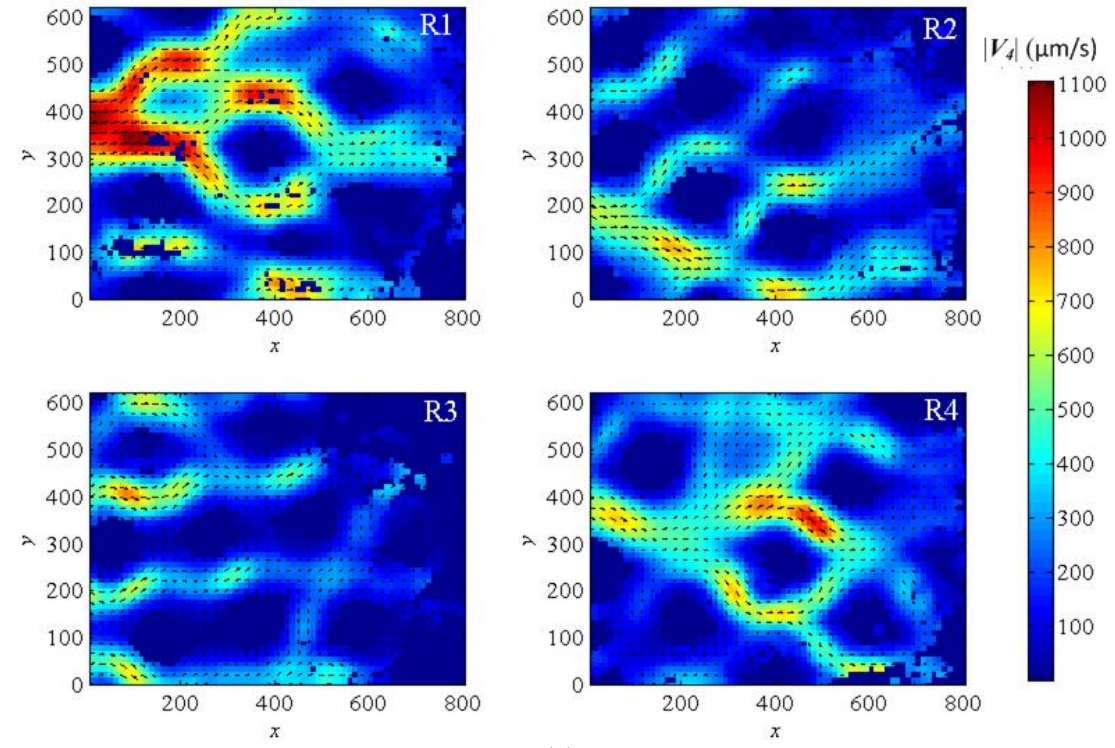
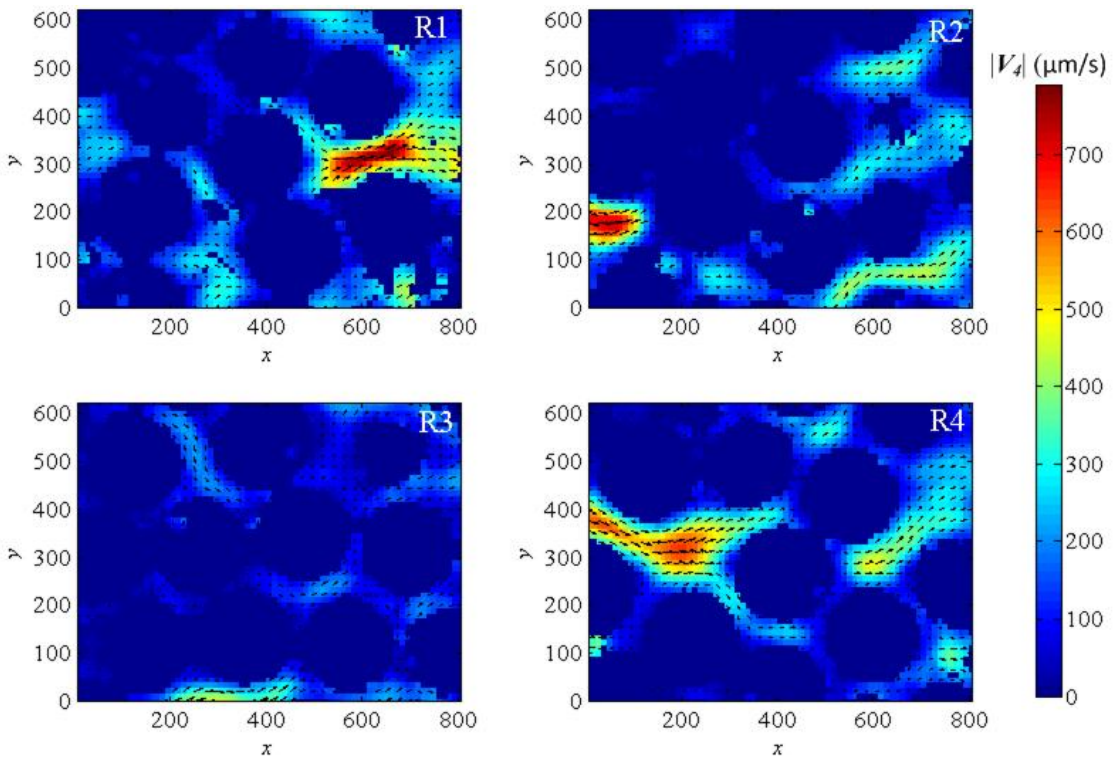


Figure 3-4 Velocity plots for $Q_s = 80 \mu\text{l/min}$. The color map shows the magnitude of velocity. (a) Close to the wall at $z = 25 \mu\text{m}$ (b) Mid plane location of first layer of spheres at $z = 100 \mu\text{m}$ (b)



(a)



(b)

Figure 3-5 Velocity plots for $Q_s = 100 \mu\text{l/min}$. The color map shows the magnitude of velocity. (a) Close to the wall at $z = 25 \mu\text{m}$ (b) Mid plane location of first layer of spheres at $z = 100 \mu\text{m}$.

Figure 3-2 shows that the magnitude of velocity field in the narrow pore locations for region R1 is low, which is denoted by the blue color in the narrow pore regions. In Fig. 3-3 through Fig. 3-5 the narrow pore locations recorded high velocity for region R1, denoted by the red color. The low velocity field at flow rate 40 $\mu\text{l}/\text{min}$ at region R1 could be due to an experimental error which occurred while accruing the data. Precautionary measures were taken while acquiring the data and sufficient time was provided before acquiring a steady velocity field for each flow rate. The reason for low flow velocity may be due to momentary obstruction in flow by any hidden air bubble in the flow system. All other velocities plots for different regions show a consistence pattern and it can be concluded that the problem was momentary and only affected the velocity field at region R1 for flow rate of 40 $\mu\text{l}/\text{min}$.

The velocity field at different marked locations shown in Fig. 3-1 is tabulated in Table 3-1. The magnitude of velocity corresponding to inlet flow rate of 60 $\mu\text{l}/\text{min}$, shown in Fig. 3.3, is studied. The dimensions of locations L1, L2, L3 and L4 are 100 $\mu\text{m} \times 100 \mu\text{m}$, 80 $\mu\text{m} \times 80 \mu\text{m}$, 125 $\mu\text{m} \times 125 \mu\text{m}$ and 75 $\mu\text{m} \times 75 \mu\text{m}$ respectively. For each representative location the velocity field close to the wall, i.e., at $z = 25 \mu\text{m}$ is compared with the velocity field at the mid plane location at $z = 100 \mu\text{m}$. Here, $|\overline{V}_L|$ represents the magnitude of average velocity field at location L, $|\overline{V}_2|$ is the average velocity field for the entire region of 800 $\mu\text{m} \times 600 \mu\text{m}$ and the ratio of velocity $\frac{|\overline{V}_L|}{|\overline{V}_2|}$ is calculated. The value of the ratio gives an indication of the velocity field in each location compared to the average velocity field for the entire region. The location, L1, close to the wall ($z = 25 \mu\text{m}$), represents a narrow pore region between two spheres and the magnitude of velocity is

high, as shown in subplot denoted by R1 in Fig. 3-3 (a). In this case, the magnitude of velocity is three times higher than the average velocity, as observed from Table 3-1. However, for the same location L1 but at the center plane ($z = 100 \mu\text{m}$), the magnitude of velocity is lower because the pore space becomes significantly constricted as the spheres are almost touching each other. It has been observed that velocity, in general, is higher at narrow pore locations. In the narrow pore region the magnitude of velocity is higher, but below a certain inter-pore distance, the pore becomes impermeable to the flow and magnitude of velocity decreases significantly. A similar observation is made in region L2 where the magnitude of velocity decreases from plane $z = 25 \mu\text{m}$ to $z = 100 \mu\text{m}$ as shown in Fig. 3-3(a) and Fig. 3-3(b), respectively.

Table 3-1 Comparison of velocity field at different locations denoted by L1, L2, L3 and L4. $\overline{|\mathbf{V}_L|}$ denotes the magnitude of average velocity at location L and the $|\overline{\mathbf{V}_2}|$ represents the magnitude of velocity for the entire region at $Q_s = 60 \mu\text{l/min}$. The magnitude of velocity field at both planes denoted by z is studied.

Location	z (μm)	$\overline{ \mathbf{V}_L }$ ($\mu\text{m/s}$)	$ \overline{\mathbf{V}_2} $ ($\mu\text{m/s}$)	$\frac{\overline{ \mathbf{V}_L }}{ \overline{\mathbf{V}_2} }$
L1	25	820	270	3.04
L1	100	60	140	0.43
L2	25	295	165	1.79
L2	100	81	113	0.72
L3	25	267	178	1.5
L3	100	342	149	2.3
L4	25	230	178	1.29
L4	100	249	149	1.67

The velocity field in relatively large pores denoted by L3 and L4 are studied at both the planes. The magnitude of velocity is higher for relatively big pores at the mid plane location compared to the plane close to the wall. The ratio $\frac{\overline{V_L}}{\overline{V_2}}$ for location L3 increases from 1.5 to 2.3 from plane $z = 25 \mu\text{m}$ to $z = 100 \mu\text{m}$ (Table 3-1). Similar behavior was captured for location L4. The pore at location L4 is enclosed by three spheres to its left as highlighted in R4 in Fig. 3-1 (d), which potentially blocks any in-plane fluid flow into the pore. However, high flow velocity is observed within the pore at location L4 and the pore acts as a source as shown in subplot marked R4 in Fig. 3-2 (b) through Fig. 3.5 (b). The high velocity field was due to the contribution from the out of plane component of the velocity field. At location L4, fluid flows into the pore from the planes above it. This was confirmed by reviewing the raw time series data close to the wall at location L4. The fluorescent particles which appear as bright white dots were found to disappear into the pore at location L4. However, this chapter deals with 2C2D measurement and the 3C3D measurement is discussed in chapter 4 which deals with out of plane component of velocity.

3.3 Probability density functions for the velocity field

A further detailed study of velocity field is conducted using statistical methods. These methods allowed the comparison of results with existing results for similar experimental and numerical studies conducted for macro-porous media. The probability function for the transverse component of velocity, v , as well as the longitudinal component of velocity, u , is studied separately. Histograms are commonly used to represent probability density for a univariate statistical data (Silverman 1986). Kernel

density estimators are another technique for estimating probability density functions and can provide a better estimate compare to a histogram (Silverman 1986). Each component of velocity field is a univariate data for the current study. The kernel density function for a univariate data such as $[u_1, u_2, u_3, \dots, u_N]$ is given by equation 3.2.

$$f(u) = \frac{1}{Nh} \sum_{i=1}^N K\left(\frac{u-u_i}{h}\right) \quad (3.2)$$

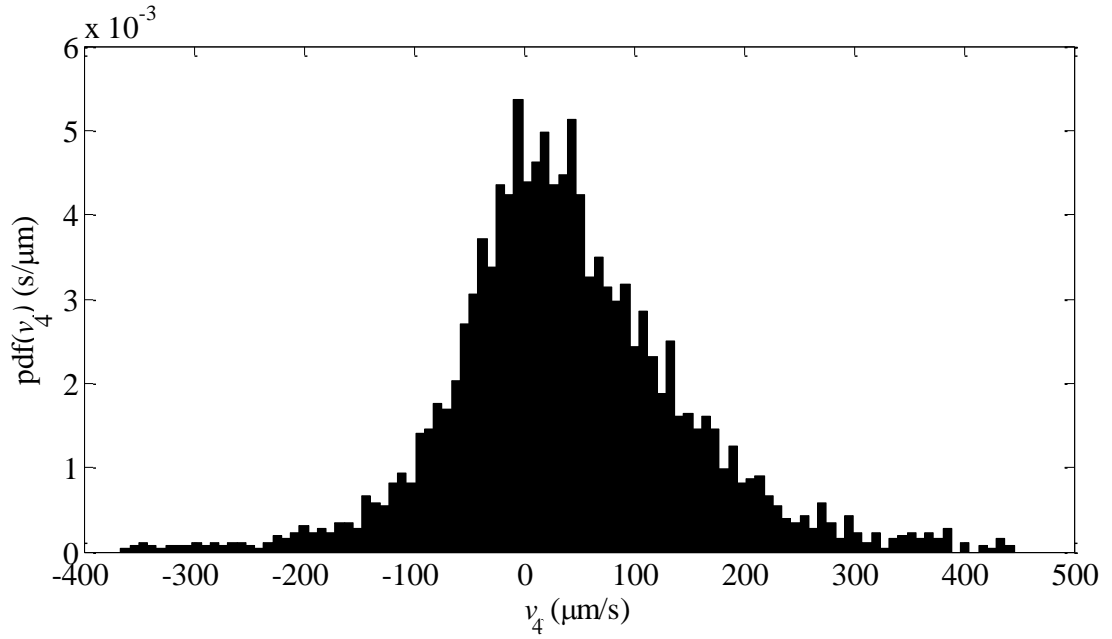
where, K is the kernel function, h is the band width of the kernel and N is the total number of data points. Selection of kernel band width plays an important role in estimating the data. A wide bandwidth can over smooth the data and a narrow bandwidth can result in too many peaks and troughs (Silverman 1986). An optimized band width is selected for the current study by using equation 3.3

$$h = 1.06\sigma N^{-0.2} \quad (3.3)$$

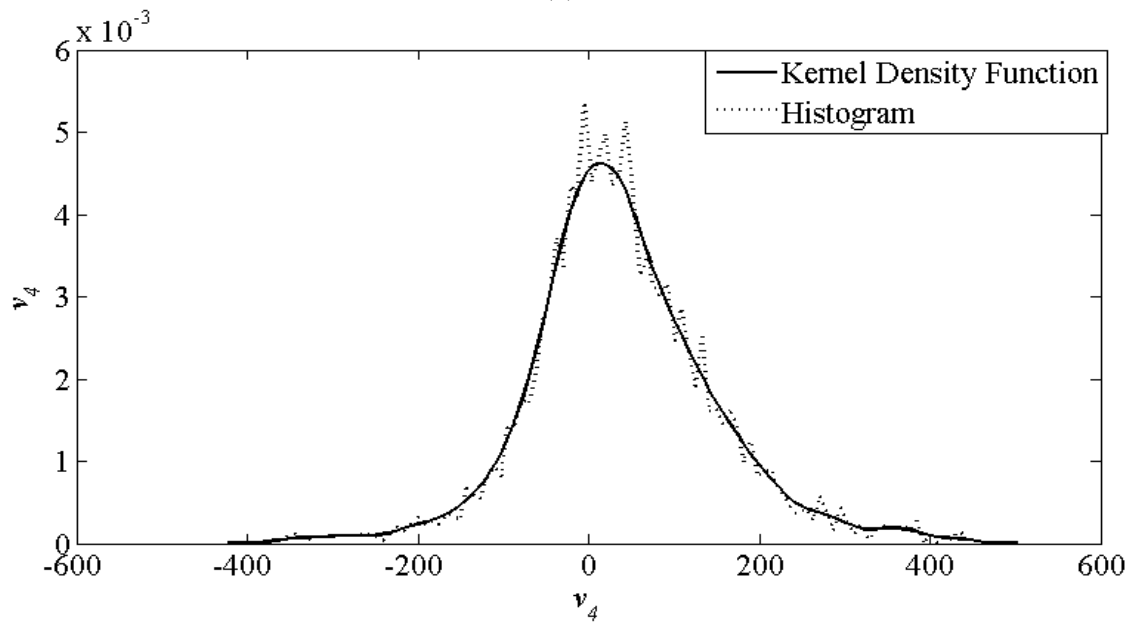
where, σ is the standard deviation of the univariate data.

The function ‘Ksdensity’ provided in Matlab was used to plot the pdf of each component of velocity field. A Gaussian kernel was used for estimating the data. A comparison of pdf of each component of velocity field predicted by kernel density function and the pdf estimated by a normalized histogram is shown in Fig. 3-6 and Fig. 3-7. Figure 3-6 shows the pdf of transverse component of velocity, v , and Fig. 3-7 shows the pdf of longitudinal component of velocity field, u . Before computing the pdf, all velocity values corresponding to $u = 0$ and $v = 0$ are removed from the data. This ensures that the pdf is not biased by the zero velocities at the location of the spheres or any dead

zones in the flow field. However, all other magnitudes of velocity field relatively close to zero, which occurs near the surface of the spheres, are retained.

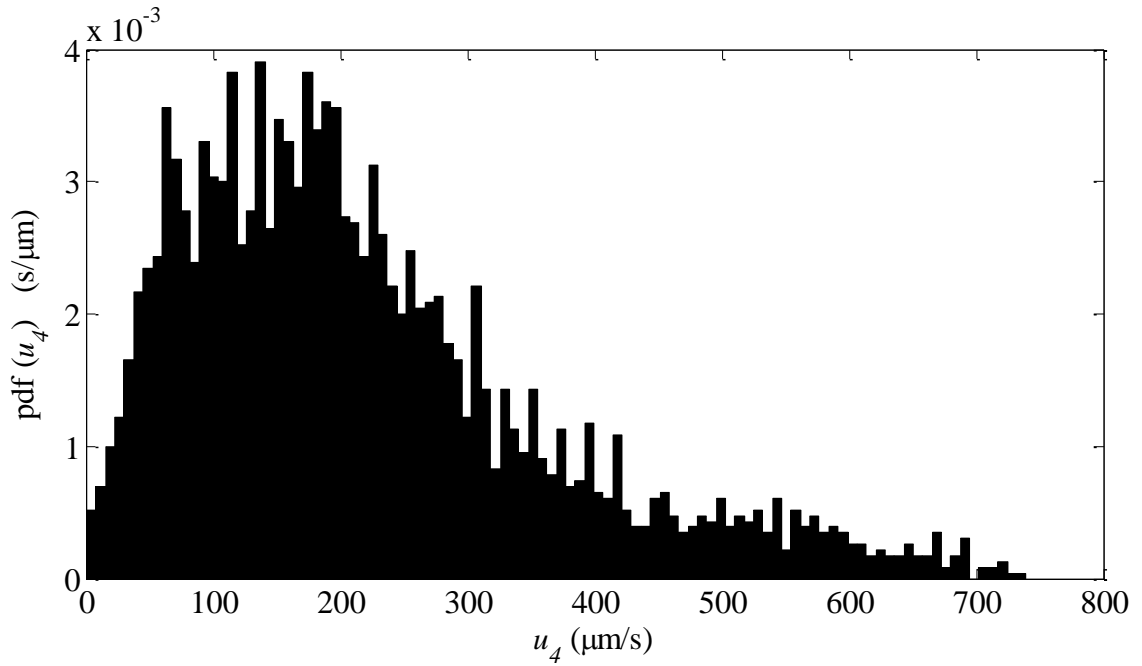


(a)

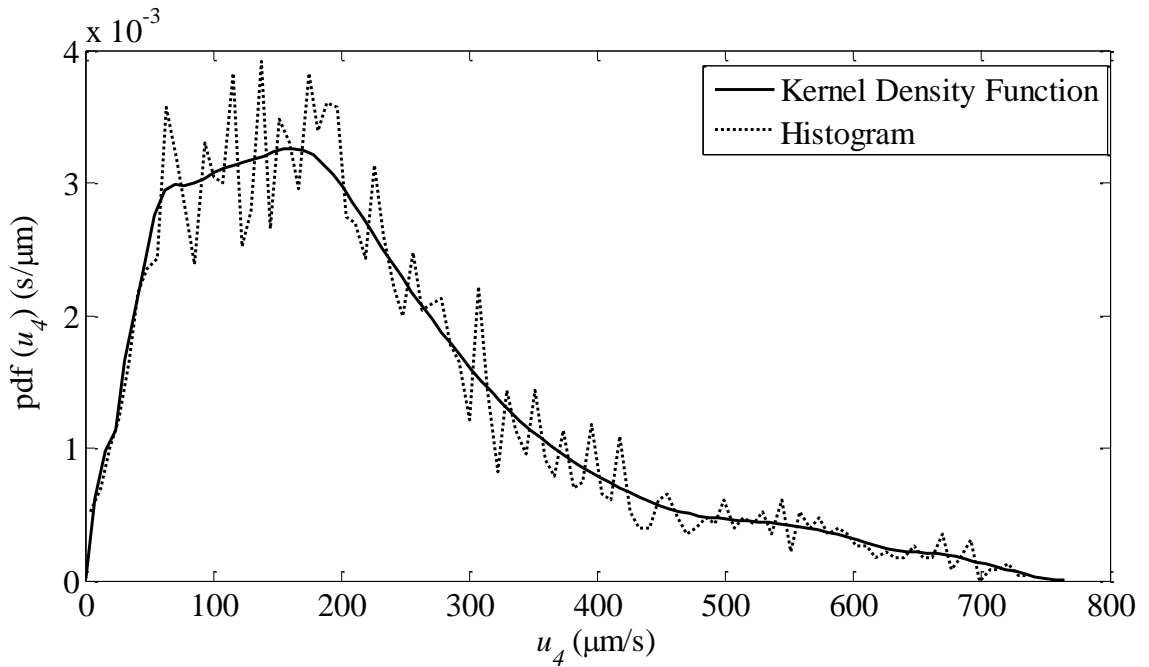


(b)

Figure 3-6 A comparison of pdf predicted by histogram with kernel density function for transverse velocity component for region R2 at $Q_s = 100 \mu\text{l}/\text{min}$. The observation was made for data obtained close to the wall at $z = 25 \mu\text{m}$ plane. (a) A normalized histogram is plotted with bin size $10 \mu\text{m}/\text{s}$. (b) A smooth velocity profile obtained by kernel density estimator which closely preserves the trend of the histogram.



(a)



(b)

Figure 3-7 A comparison of pdf predicted by histogram with kernel density function for axial velocity component for region R2 at $Q_s = 100 \mu\text{l}/\text{min}$. The observation was made for data obtained close to the wall at $z = 25 \mu\text{m}$ plane (a) A normalized histogram is plotted with bin size $10 \mu\text{m}/\text{s}$. (b) A smooth velocity profile obtained by kernel density estimator which closely preserves the trend of the histogram.

The velocity field at region R2 at $z = 25 \mu\text{m}$ was chosen to obtain the pdf of each component of velocity field. The pdf of velocity field at different inlet flow rates at different Reynolds number at region R2 is studied. The mean velocity at different flow rates and Reynolds number is tabulated in Table 3-2.

Table 3-2 A summary of flow rate (Q_s), average velocity field and Reynolds number for region R2. The observations are made close to wall at $z = 25 \mu\text{m}$

Region	Flow Rate, Q_s ($\mu\text{l}/\text{min}$)	$ \overline{\mathbf{V}}_i $ ($\mu\text{m}/\text{s}$)	Re_p
R2	40	117	0.023
R2	60	165	0.033
R2	80	198	0.040
R2	100	246	0.049

The pdf of velocity field is also studied at different regions to capture any influence of pore structure on the flow profile. The inlet flow rates for different regions are chosen such that the Reynolds numbers are close to each other. This ensures that the effect of Reynolds number is minimized. The inlet flow rates, average velocity fields and Reynolds number are tabulated in Table 3-3 and Table 3-4.

Table 3-3 A summary of flow rate (Q_s), average velocity field and Reynolds number for different regions.

The observations are made close to wall at $z = 25 \mu\text{m}$

Region	Flow Rate, Q_s ($\mu\text{l}/\text{min}$)	$ \overline{\mathbf{V}}_i $ ($\mu\text{m}/\text{s}$)	Re_p
R1	60	270	0.054
R2	100	245	0.049
R2	100	221	0.044
R2	100	272	0.054

Table 3-4 A summary of flow rate (Q_s), average velocity field and Reynolds number for different regions.

The observations are made at mid plane location at $z = 100 \mu\text{m}$

Region	Flow Rate, Q_s ($\mu\text{l}/\text{min}$)	$ \overline{\mathbf{V}}_i $ ($\mu\text{m}/\text{s}$)	Re_p
R1	60	141	0.028
R2	80	151	0.032
R2	100	116	0.023
R2	60	149	0.03

3.3.1 Pdf of transverse velocity field

The transverse component of the velocity field, v_i , is non-dimensionalized with its standard deviation, σ_{v_i} , and the pdf of $\left(\frac{v_i}{\sigma_{v_i}}\right)$ is plotted against $\left(\frac{v_i}{\sigma_{v_i}}\right)$ using Ksdensity function as shown in Fig. 3-8(a). This allows us to compare the results available in the literature. The velocity field obtained in the current study closely fits a Gaussian normal distribution curve with a regression square value of 0.98. The velocity profile has a peak close to zero. The agrees well with Moroni & Cushman (2001). It is observed that the experimental data of Moroni & Cushman (2001) underestimates the peak, compared to the present results, as shown in Fig. 3-8 (a). Moroni & Cushman (2001) used bubbles as tracers to determine the flow field and the optical system could not successfully sample velocity fields close to the sphere surfaces. However, in the current study, the PIV+PTV algorithm can track the fluorescent particles close to the wall and near zero velocities are obtained. This results in an increase in the peak height since the number of velocity vectors having magnitude close to zero increases. Similar velocity profiles were obtained for transverse velocity measurement conducted by (Huang et al. 2008). The pdf of $\left(\frac{v_i}{\sigma_{v_i}}\right)$ is plotted against $\left(\frac{v_i}{\sigma_{v_i}}\right)$ for different Reynolds number as shown in Fig. 3-8(b). It was observed that with the increase in Reynolds number, the peak height in the velocity pdf increases. With the increase in Reynolds number, a larger number of vectors is observed close to the glass sphere surface, which contributed to an increase of the peak height.

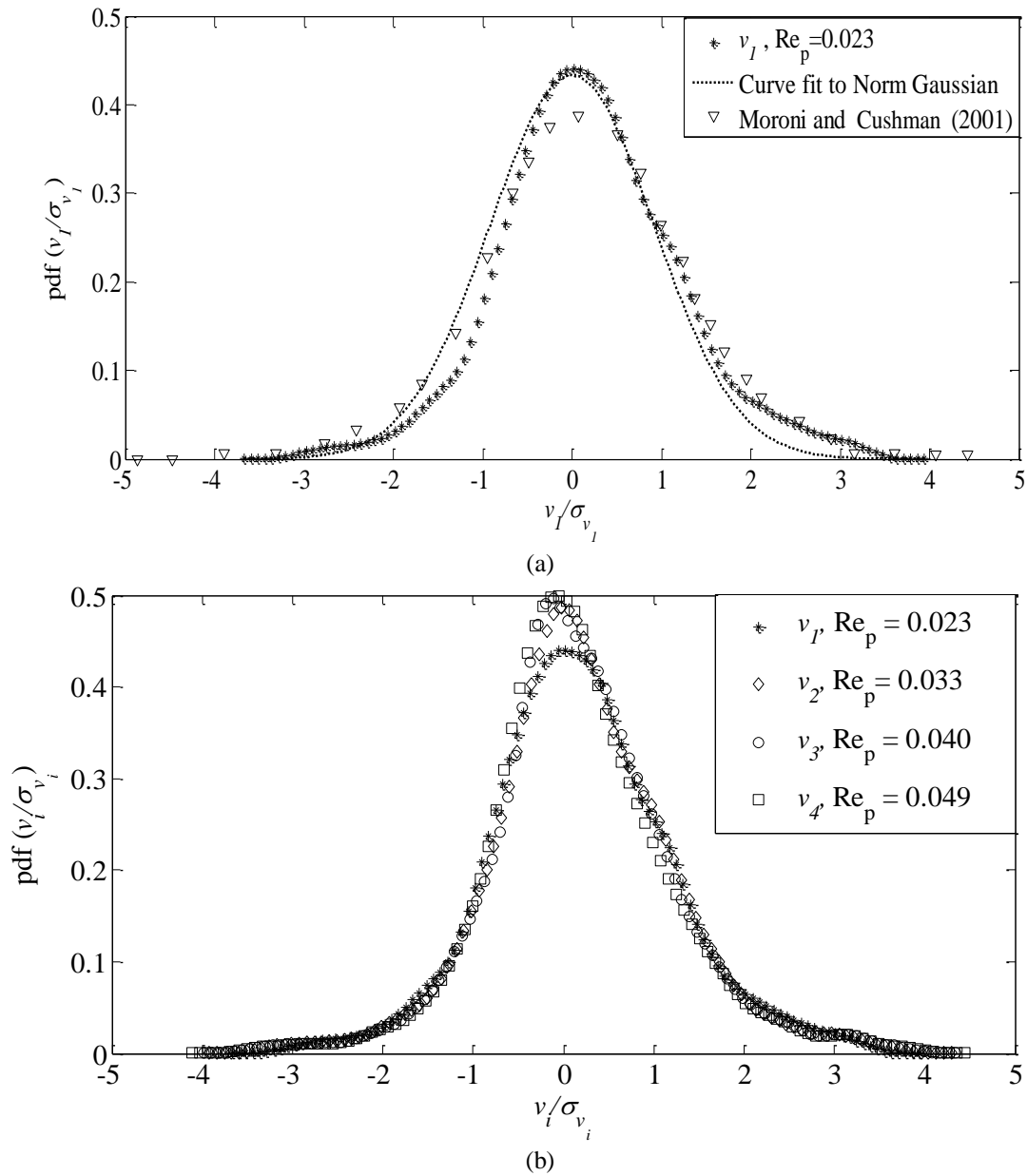
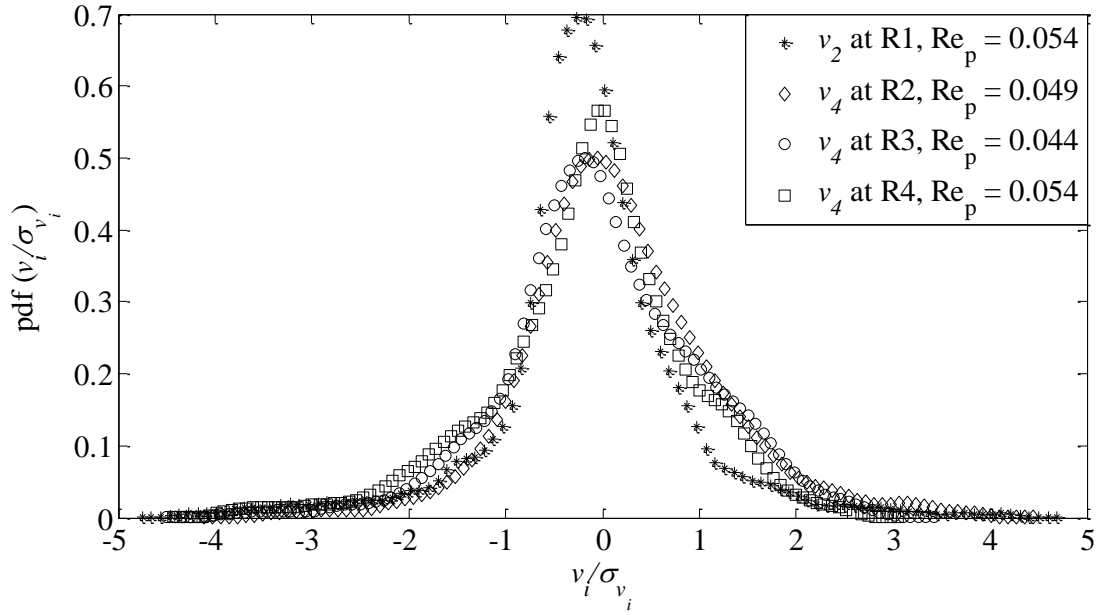
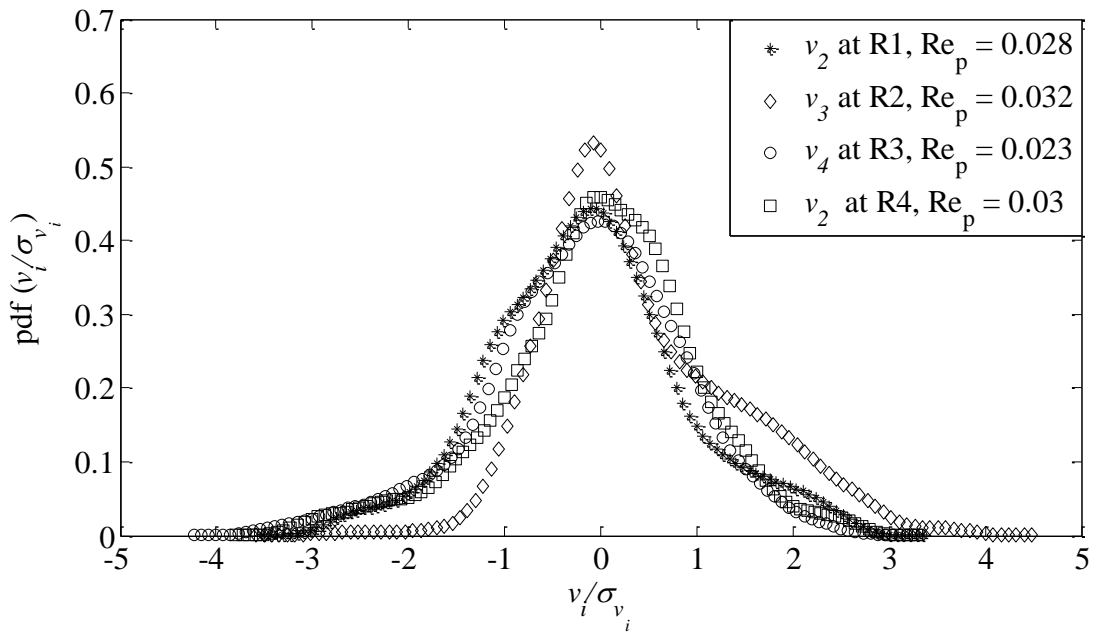


Figure 3-8 The probability density function (pdf) of non-dimensionalized transverse (y-component) velocity $\left(\frac{v_i}{\sigma_{v_i}}\right)$ is plotted, where σ_{v_i} the standard deviation of v_i is, is plotted. The velocity data are obtained from R2 at $z = 25 \mu\text{m}$ plane. (a) pdf $\left(\frac{v_1}{\sigma_{v_1}}\right)$ is denoted by *asterisk*. v_1 is the transverse velocity component corresponding to the mean velocity and $\text{Re}_p = 0.023$. A normal Gaussian curve is fitted to the data as shown by *dotted lines*. The results are compared with Moroni and Cushman (2001), denoted by *upward pointing triangle*. (b) pdf is plotted for four Reynolds numbers.

The pdf of transverse velocity field is also computed for the plane close to the wall for different regions R1, R2, R3 and R4 as shown in Fig. 3-9 (a). The values of flow parameters for this study are documented in Table 3-3. It can be observed that for different regions the velocity field collapses well into a Gaussian shaped curve with center of the peak close to zero. Although, the Reynolds number are selected close to each other for this study but the influence of Reynolds number is still visible. The height of the peak is influenced by Reynolds number and the peak height increases with Reynolds number. The influence of Reynolds number is more prominent than the influence of pore structure at different regions. The region denoted by R1 and R4 has the same Reynolds number but for Region R1 the peak height is higher compared to region R4. This could be an influence of the pore geometry.



(a)



(b)

Figure 3-9 The probability density function (pdf) of non-dimensionalized transverse (y-component) velocity $\left(\frac{v_i}{\sigma_{v_i}}\right)$ is plotted, where σ_{v_i} the standard deviation of v_i . The velocities data are obtained at different regions are shown. (a) velocity profile close to the wall at $z = 25 \mu\text{m}$ (b) velocity profile at mid plane location at $z = 100 \mu\text{m}$.

3.3.2 Pdf of longitudinal velocity field

The pdf of the longitudinal velocity, u_i , is plotted using Ksdensity function as shown in Fig. 3-10. The velocity profiles are studied, at different Reynolds number. It has been observed from the experiments that with the increase in flow velocity, the positive tails of the velocity increases as shown in Fig. 3-10. Similar trend for positive tail was observed by Huang et al. (2008) and Moroni & Cushman (2001) for macroscopic study. In the collected velocity fields, no recirculation zone was observed and there is no evidence of negative velocity which could be due to the fact that the experiments are conducted at low Reynolds number. Maier et al. (1998) in their numerical study showed that the decrease in Reynolds number, the negative tails decreases due to a lower chance of flow recirculation. Maier et al. (1998) showed that for a random packed bed, the negative tail almost disappears for Reynolds number less than 0.6.

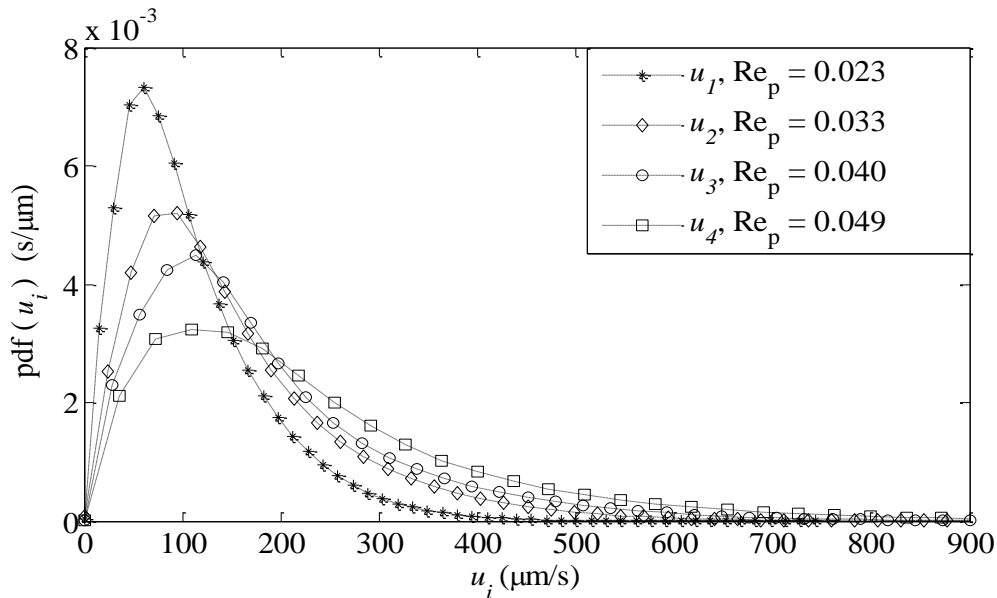
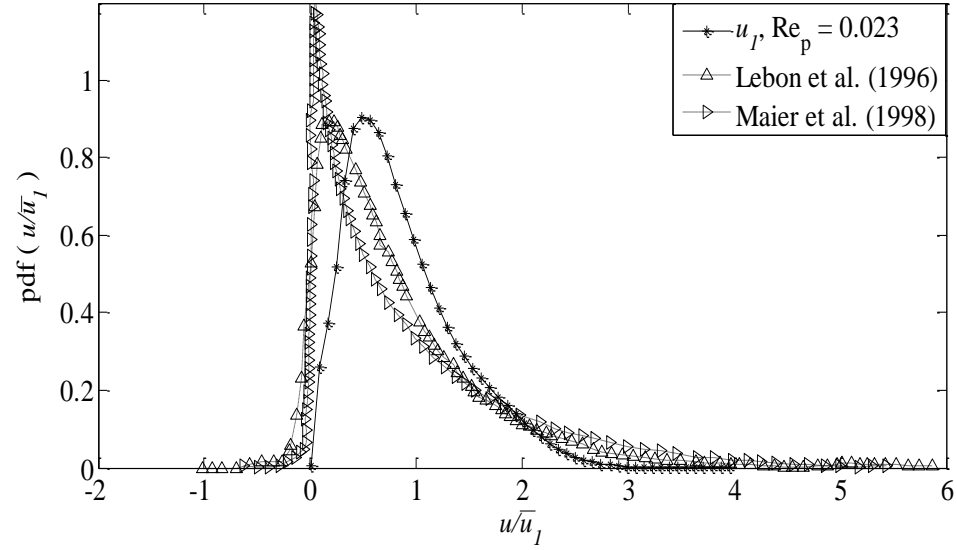
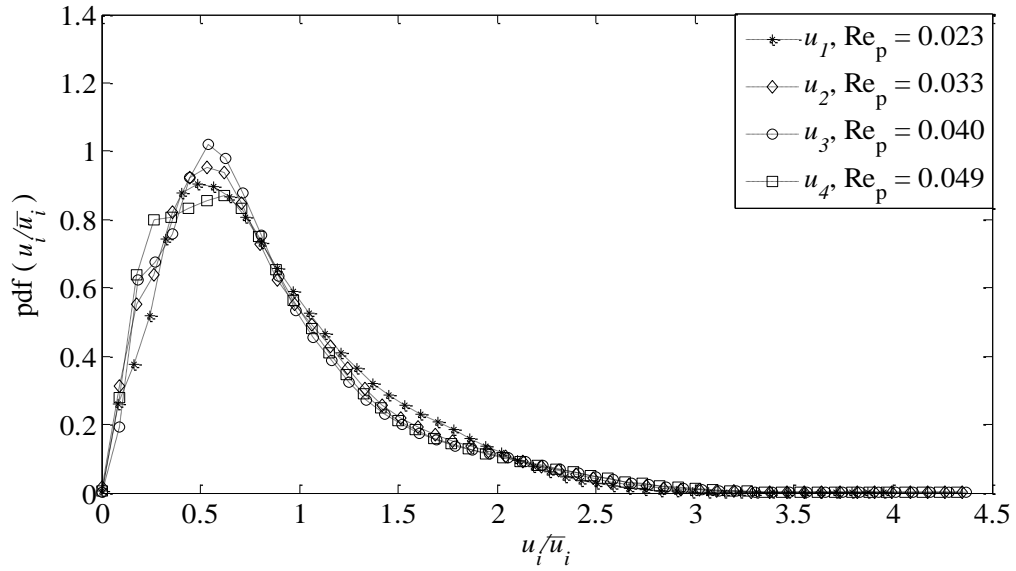


Figure 3-10 The probability density function for longitudinal velocity component, u_i , is plotted at different Reynolds number. The velocity data is obtained at region R2 at $z = 25 \mu\text{m}$ plane.

For the purpose of comparing our results with available data for macro-porous media, longitudinal velocity, u_i , is non-dimensionalized by dividing it with its mean, $\overline{u_i}$. The probability density function of $\left(\frac{u_i}{\overline{u_i}}\right)$ is plotted in Fig. 3-11 (a). The present results are compared with numerical results provided by Maier et al. (1998) and experimental data given by Lebon et al. (1996). Maier et al. (1998) obtained a sharp peak at zero axial velocity because the numerical method sampled data very close to the spheres, within one lattice space. Lebon et al. (1996) used nuclear magnetic resonance (NMR) technique to obtain velocity distribution as shown in Fig. 3-11 (a). A sharp peak was not obtained by them because of loss of signal close to the surface. Similar results are obtained for the current study. The PIV+PTV algorithm could successfully track particles close to the surface of the glass beads, however there are particles which get attached to the glass beads or particles which move less than its diameter. This results in neglecting some of the velocity fields very close to the glass beads and this explains the reason for not obtaining a sharp peak. Since there are no negative velocity in the data, the peak is biased to the positive side as compared to Maier et al. (1998) and Lebon et al. (1996). The negative tail of velocity was observed by Maier et al. (1998) due to flow recirculation. The present study was conducted at Reynolds number 10^{-2} and there was hardly any flow recirculation. Figure 3-11 (b) shows the probability density function of $\left(\frac{u_i}{\overline{u_i}}\right)$ for different Reynolds number. At different Reynolds the pdf of $\left(\frac{u_i}{\overline{u_i}}\right)$ collapses well into one curve as shown in Fig. 3-11 (b). This confirms that creeping flow regime for the current study as pointed out by Moroni and Cushman (2001).



(a)



(b)

Figure 3-11 The probability density function (pdf) of non-dimensionalized longitudinal (x -component) velocity $\left(\frac{u_i}{\bar{u}_i}\right)$, where \bar{u}_i is the arithmetic mean of u_i , is plotted on the vertical axis and $\left(\frac{u_i}{\bar{u}_i}\right)$ is plotted on the horizontal axis. The velocity data is obtained from region R2 at $z = 25 \mu\text{m}$ plane (a) $\text{pdf}\left(\frac{u_i}{\bar{u}_i}\right)$ is denoted by *asterisk*. u_1 is the transverse velocity component corresponding to mean velocity $|\bar{V}_1| = 117 \mu\text{m/s}$ and $\text{Re}_p = 0.023$. The results are compared with Lebon et al. (1996) denoted by *upward pointing triangle* and Maier et al. (1998) denoted by *right pointing triangle* (b) $\text{pdf}\left(\frac{u_i}{\bar{u}_i}\right)$ is plotted for four different Reynolds number.

Similar to the transverse velocity profile the longitudinal velocity profile is studied for different regions denoted by Fig. 3-12 (a) and Fig. 3-12 (b). The longitudinal velocity is studied at two planes at $z = 25 \mu\text{m}$ and $z = 100 \mu\text{m}$ plane. The tails of the velocity profiles collapse well and it can be concluded that the creeping flow holds good for different regions (Moroni & Cushman 2001).

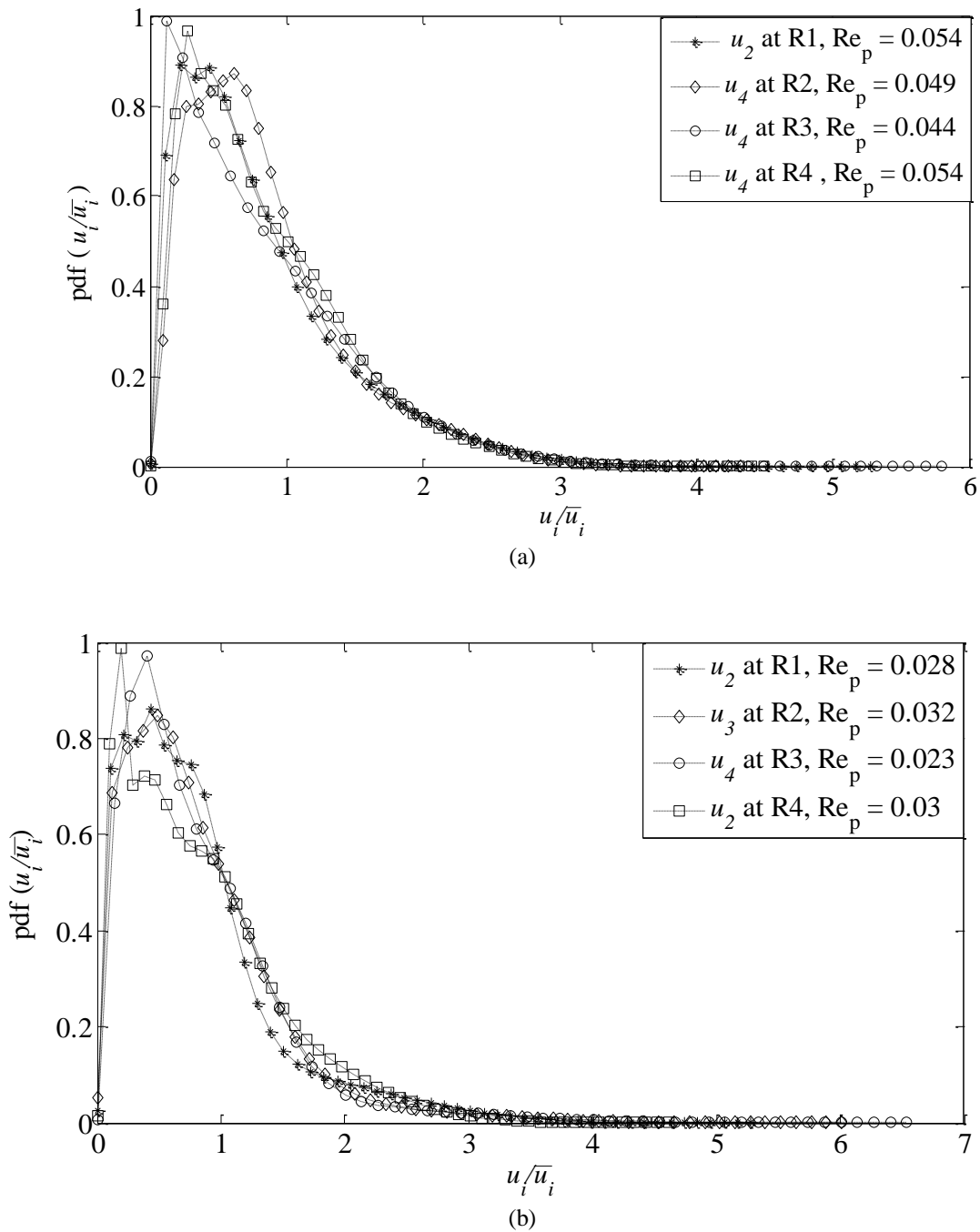


Figure 3-12 The probability density function (pdf) of non-dimensionalized longitudinal (x -component) velocity $\left(\frac{u_i}{\bar{u}_i}\right)$, where \bar{u}_i is the arithmetic mean of u_i , is plotted on the vertical axis and $\left(\frac{u_i}{\bar{u}_i}\right)$ is plotted on the horizontal axis. The velocity profile at different regions are studied. (a) velocity profile close to the wall at $z = 25 \mu\text{m}$ (b) velocity profile at mid plane location at $z = 100 \mu\text{m}$.

3.4 Summary

The 2C2D velocity field at different regions in the porous media is studied. The velocity field at close to the wall and at mid plane location is studied. The statistical distribution of each component of the velocity field is studied and the effect of Reynolds number on the velocity profiles is noted. The results agreed well with available numerical and experimental results pertaining to macro-porous media. Creeping flow behavior at low Reynolds number is observed for the present study.

CHAPTER 4: RESULTS AND DISCUSSIONS PERTAINING TO THE 3C3D VELOCITY FIELD MEASUREMENT

4.1 Introduction

In this chapter a preliminary study is reported to capture the 3C3D velocity field within the micro porous media. The main objective of the study is to show that the velocity field within a micro porous media is in fact three dimensional and the present optical measurement technique can resolve the out of plane component of velocity field. For this study a packed bed of 400 μm glass spheres are used. A single pore region formed by four micro spheres is identified and the 3C3D velocity field is studied in the pore region. In Fig. 4.1 the pore region formed by four spheres are shown. The spheres are marked by symbols S1, S2, S3 and S4. The positive z axis is into the plane i.e., away from the observer. The location of the z plane for this study is explained by Fig. 2.6. Few representative location marked by L_1 , L_2 , L_3 and L_4 as shown in Fig. 4.1 is used to study the z component of velocity field

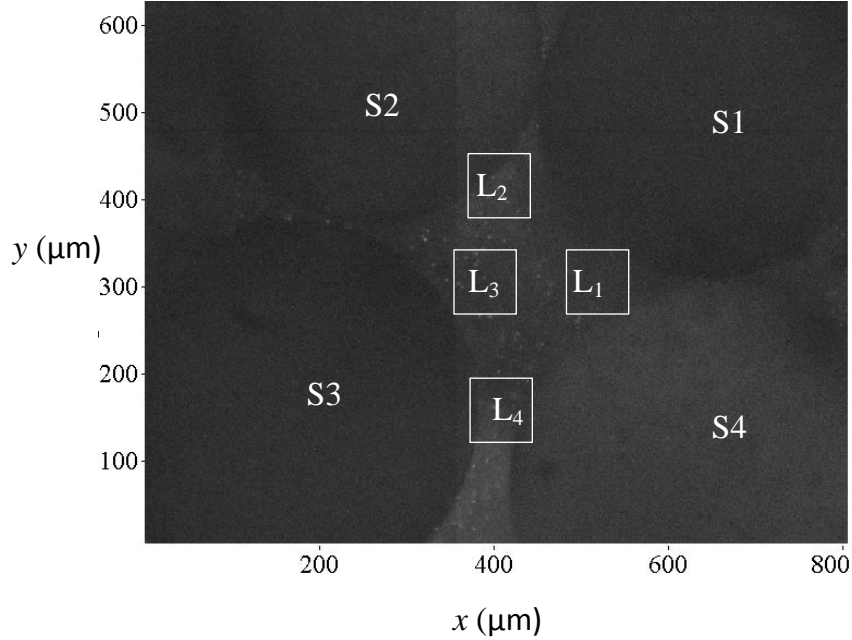


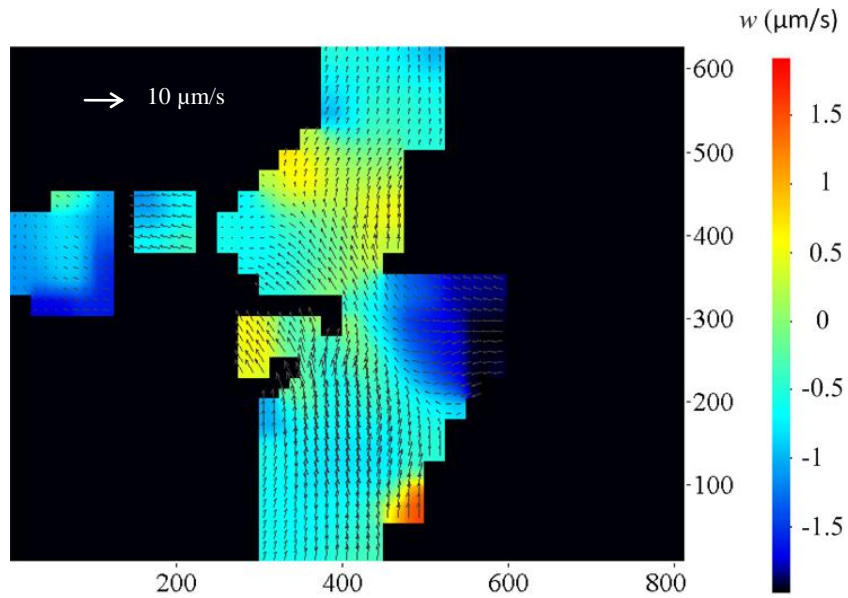
Figure 4-1 A micro pore region formed by 4 glass spheres of 400 μm diameters and denoted by S1, S2, S3 and S4. Four regions which are denoted by L₁, L₂, L₃ and L₄ are identified. The out of plane component of velocity, w , is quantified for each of this locations.

4.2 3C3D velocity field

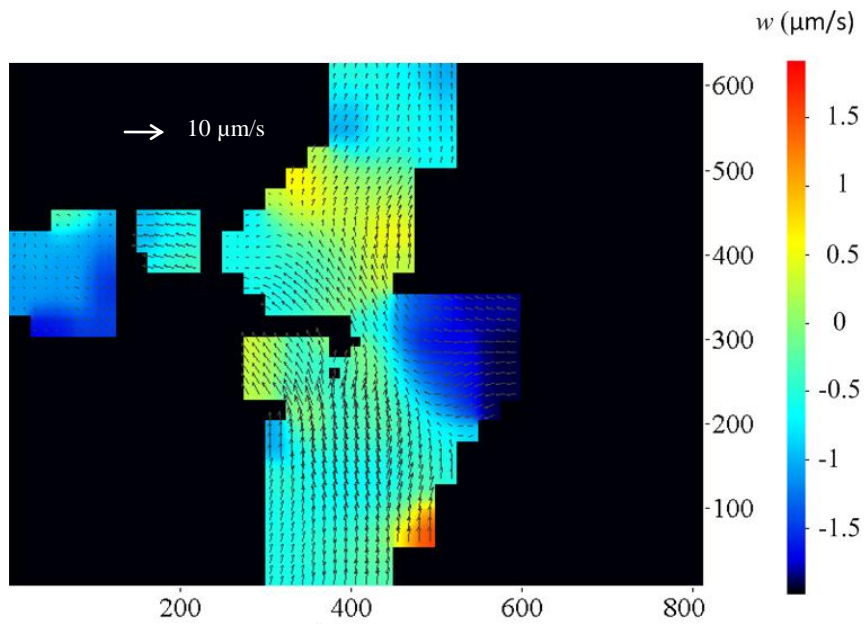
The 3C3D velocity field was obtained by using 3D cross correlation algorithm which is described in details in section 2.5.3.3. Inlet flow rate for the experiment, $Q_s = 1 \mu\text{l}/\text{min}$ was used which resulted in Reynolds number, $Re_p = 6.4 \times 10^{-4}$. The Reynolds number is calculated based on the diameter of the sphere and the average magnitude of velocity in the entire region. The calculation of Reynolds number is given by equation 1.1. The instantaneous velocity field obtained by cross correlating two volumes of data generated by two consecutive scans is presented. 2D slices at equal z interval were used to analyze the three component velocity field. The slices were taken at $z = 0 \mu\text{m}$ through $z = 72 \mu\text{m}$ at an interval of $9 \mu\text{m}$. Fig. 4-2 shows the three component velocity field at each z - plane location. For each slice, the in-plane components of velocity u and v are

represented by vectors arrow. The length of the arrow represents the magnitude of the vector. The z component of the velocity, w , is represented by the background color map.

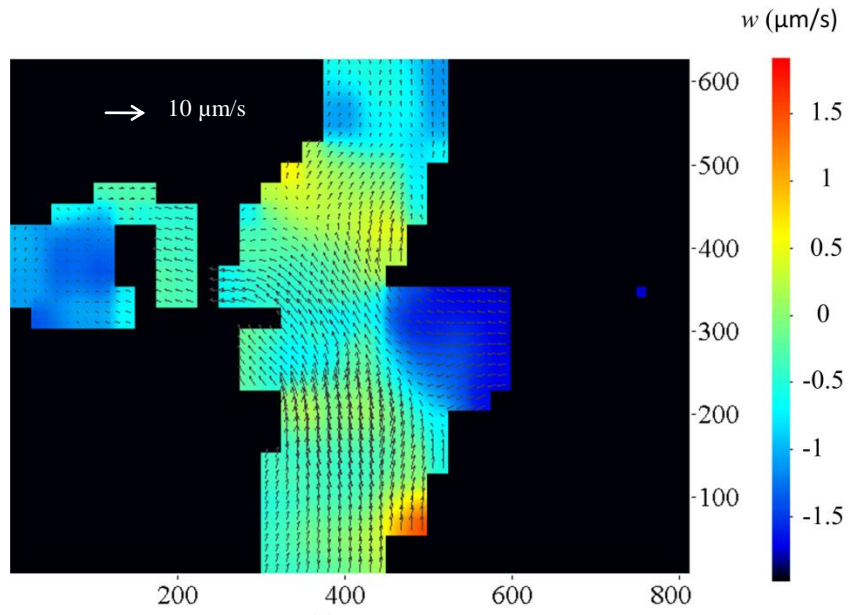
The color bar shows value of w .



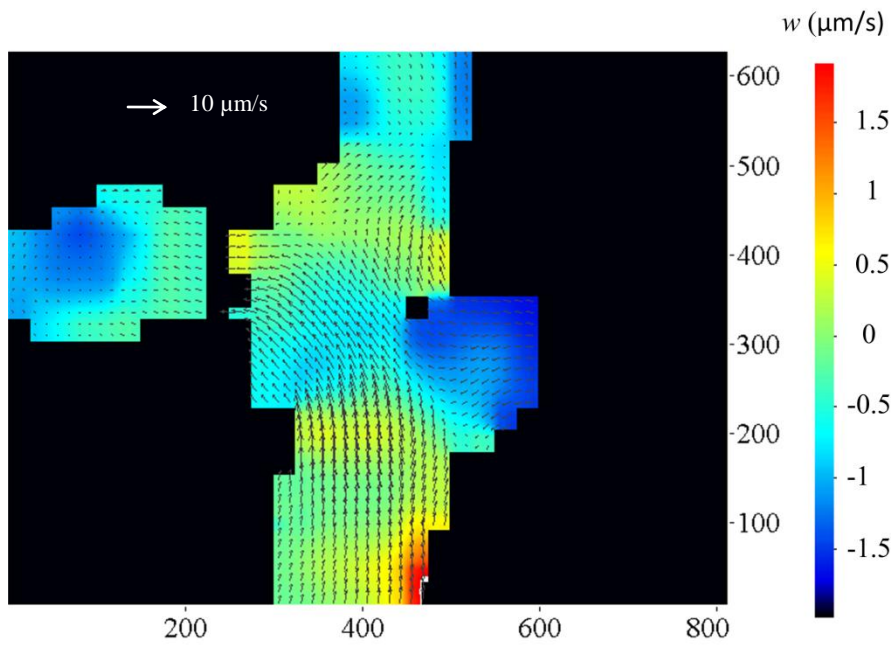
(a)



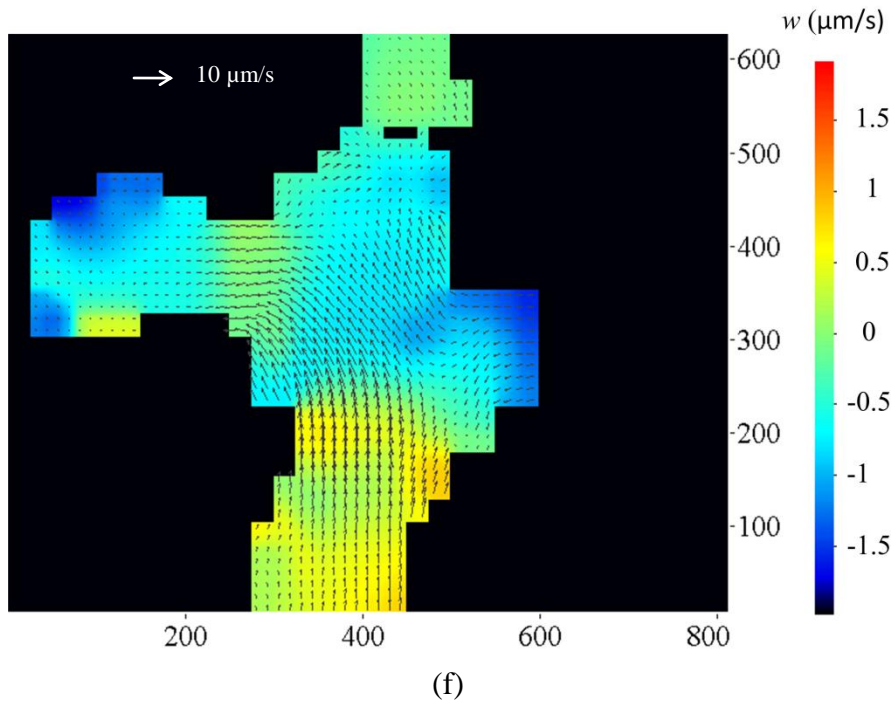
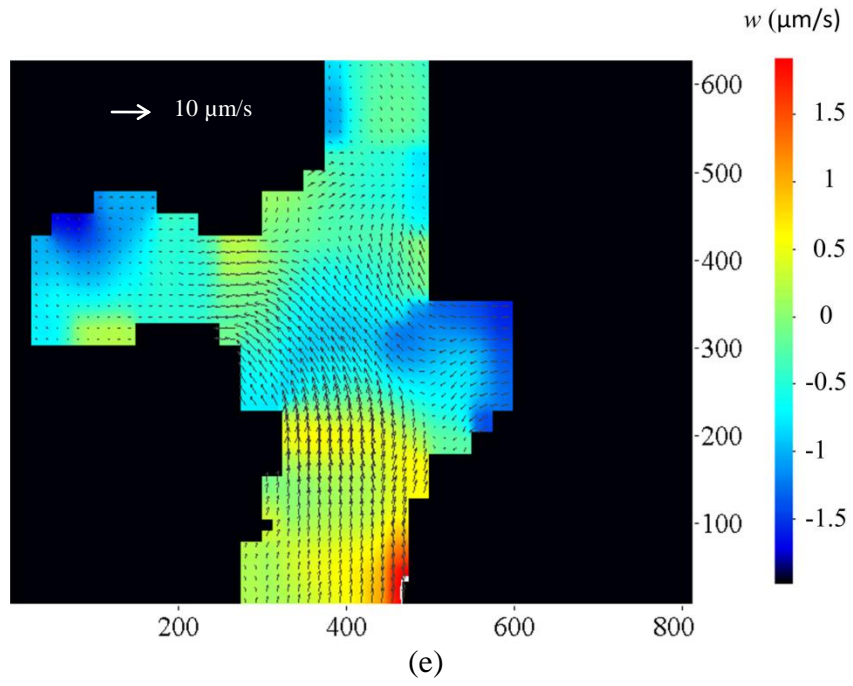
(b)

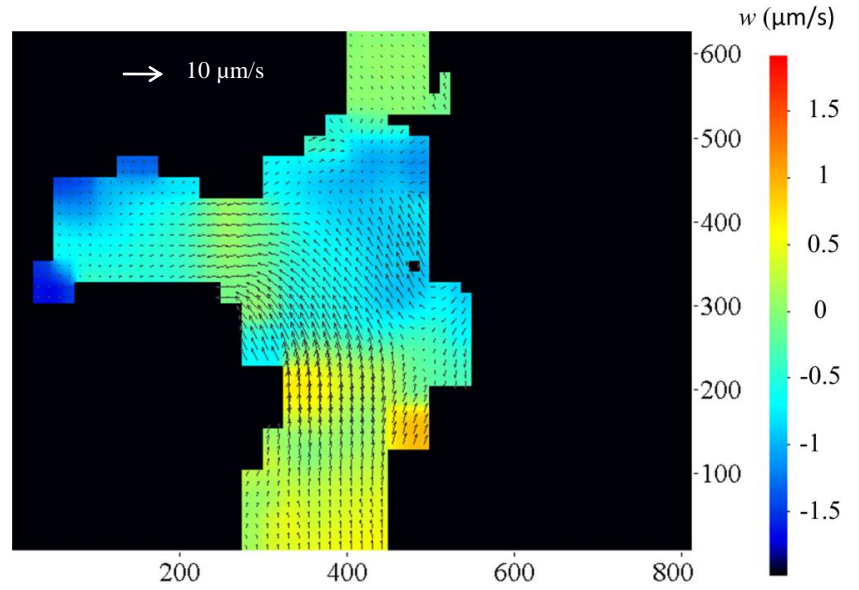


(c)

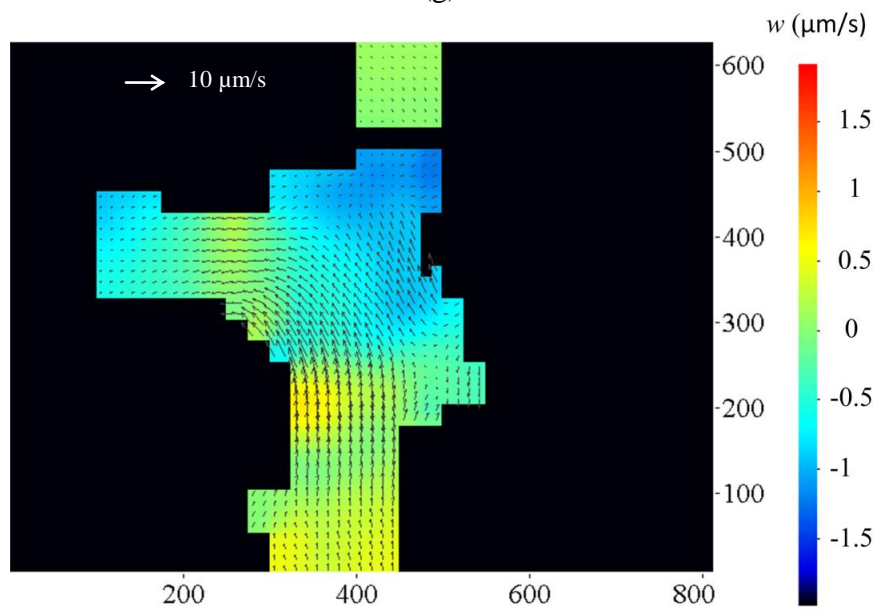


(d)





(g)



(h)

Figure 4-2 The horizontal and vertical axis represents position of x and y co-ordinate respectively in μm . The direction of flow is in negative x -direction. The in plane velocity components are denoted by the vectors. The length of the vectors denotes the magnitude. A reference velocity vector of $10 \mu\text{m/s}$ is shown. The out of plane velocity component, w , is shown by the color map and the color bar represents corresponding values of w . $Q_s = 0.1 \mu\text{l/min}$ and $\text{Re}_p = 6.4 \times 10^{-4}$. All spatial positions are in μm . Each subplot represents velocity field at a z -plane. (a) $z = 0 \mu\text{m}$ (b) $z = 9 \mu\text{m}$ (c) $z = 18 \mu\text{m}$ (d) $z = 27 \mu\text{m}$ (e) $z = 36 \mu\text{m}$ (f) $z = 45 \mu\text{m}$ (g) $z = 54 \mu\text{m}$ (h) $z = 63 \mu\text{m}$.

The in-plane velocity component is denoted by the velocity vectors which show that there is cross flow patterns in the pore regions. The general direction of flow is in the negative x direction which is from right to left. There is also flow towards positive y direction which sets up the cross flow. Fig. 4-2 (a) through 4-2 (h) shows that evidence of z component of velocities. It can be observed that the z component of velocity varies from one plane to another. Also, it is observed that at some spatial locations w has positive value, which suggests that the flow is towards the observer. A negative value of w , suggests that the flow is moving away from the observer, i.e, its moving into the pore space. A detailed quantitative value of w at different locations denoted by L_1, L_2, L_3 and L_4 is tabulated in Table 4-1. The arithmetic mean of w values denoted by \bar{w} at each location is calculated and is documented in Table 4-1

The pore space formed between sphere S1 and S4 is denoted by L_1 . Spheres S1 and S4 are physically touching each other as shown in Fig. 4-1. The major contribution of fluid velocity in location L_1 is from the out of plane fluid flow. Location L_1 , has strong out of plane component which is denoted by the blue color. The value of w increases as one moves from $z=0 \mu\text{m}$ plane to $z = 63 \mu\text{m}$ plane which is observed from the fading blue color in location L_1 in Fig. 4-2 (a) through Fig. 4-2 (b). The mean values of w at different z planes are shown in Table 4-1 and the values of \bar{w} increases as one move into the pore. At $z = 0$ plane the value of \bar{w} is $-1.26 \mu\text{m/s}$ and close to the mid plane location i.e $z = 63 \mu\text{m}$, the value of \bar{w} increases to $-0.08 \mu\text{m/s}$. Since the magnitude of \bar{w} decreases which means that the out of plane motion of the fluid towards the observer decreases as one move into the pore.

In location L₂, the value of w decreases as the mid plane location is approached. The value of \bar{w} is positive from $z = 0$ to $z = 36 \mu\text{m}$ plane. This can be observed from the color map for location L₂ in Fig. 4-2 (a) through 4-2 (e). On further moving towards the mid plane location flow reversal takes place and the value of \bar{w} becomes negative. The color map in Fig. 4-2 (f) through Fig. 4-2 (h) evidence of negative values of \bar{w} . This shows that flow reversal takes place close to the mid plane location. Fig. 4-2 shows evidence of flow reversal for location L₃ and location L₄ as well. For location L₃, flow reversal takes place on transition from $z = 18 \mu\text{m}$ to $z = 27 \mu\text{m}$. The value of \bar{w} is negative for $z = 0 \mu\text{m}$ to $z = 18 \mu\text{m}$ plane and beyond $z = 18 \mu\text{m}$ plane the value of \bar{w} becomes positive. Similar observation was made for location L₄ where flow reversal takes place on transition from $z = 9 \mu\text{m}$ to $z = 18 \mu\text{m}$. The values of \bar{w} for all locations and different planes are listed in Table 4-1.

Table 4-1 The mean value of w denoted by \bar{w} , for each spatial location denoted by L_1, L_2, L_3 and L_4 are shown below. z represents the plane at which the values of \bar{w} is measured.

z (μm)	\bar{w} at L_1 ($\mu\text{m/s}$)	\bar{w} at L_2 ($\mu\text{m/s}$)	\bar{w} at L_3 ($\mu\text{m/s}$)	\bar{w} at L_4 ($\mu\text{m/s}$)
0	-1.26	0.58	-0.15	-0.2
9	-1.28	0.61	-0.09	-0.07
18	-1.17	0.58	-0.03	0.03
27	-0.9	0.41	0.01	0.59
36	-0.6	0.09	0.09	0.83
45	-0.4	-2.5	0.18	0.9
54	-0.2	-4.7	0.24	0.7
63	-0.08	-5.5	0.26	0.6

4.3 Probability density function for w component

For the purpose of comparing the present results with the available results in literature, the w component of velocity for the entire volume is non-dimensionalized with its standard deviation, σ_w . The probability density function of $\left(\frac{w}{\sigma_w}\right)$ is plotted as shown in Fig. 4-3. The probability density function closely resembles a Gaussian normal distribution with a regression square value of 0.98. The nature of the curve can be explained from the fact that the values of w component of velocity fluctuates spatially.

The curve is symmetric about $x = 0$ because w fluctuates from positive to negative values at different spatial location.

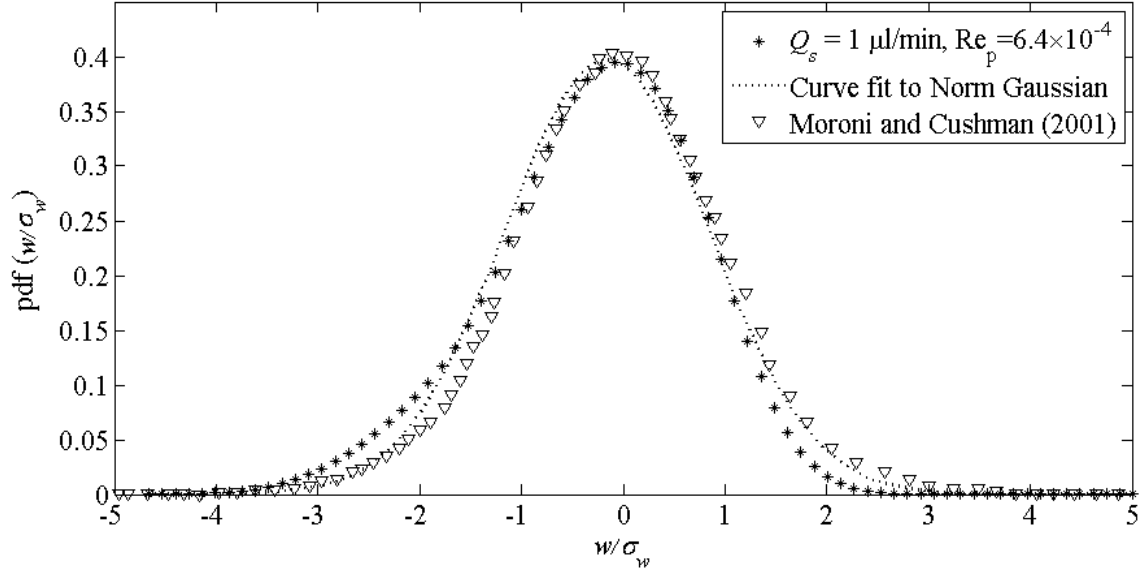


Figure 4-3 The probability density function (pdf) of non-dimensionalized transverse (z -component) velocity $\left(\frac{w}{\sigma_w}\right)$, where σ_w the standard deviation of w is, is plotted on the vertical axis and $\left(\frac{w}{\sigma_w}\right)$ is plotted on the horizontal axis. The probability density function is plotted using kernel density estimator .

The present results for w component of velocity is compared with results obtained by Moroni and Cushman, (2001). $\left(\frac{w}{\sigma_w}\right)$ values obtained by Moroni and Cushman for 3D PTV study for macro porous media, agrees well with the results from the current experiment. This shows that the nature of out of plane component of velocity is in fact Gaussian and the velocity profiles are similar for micro porous media.

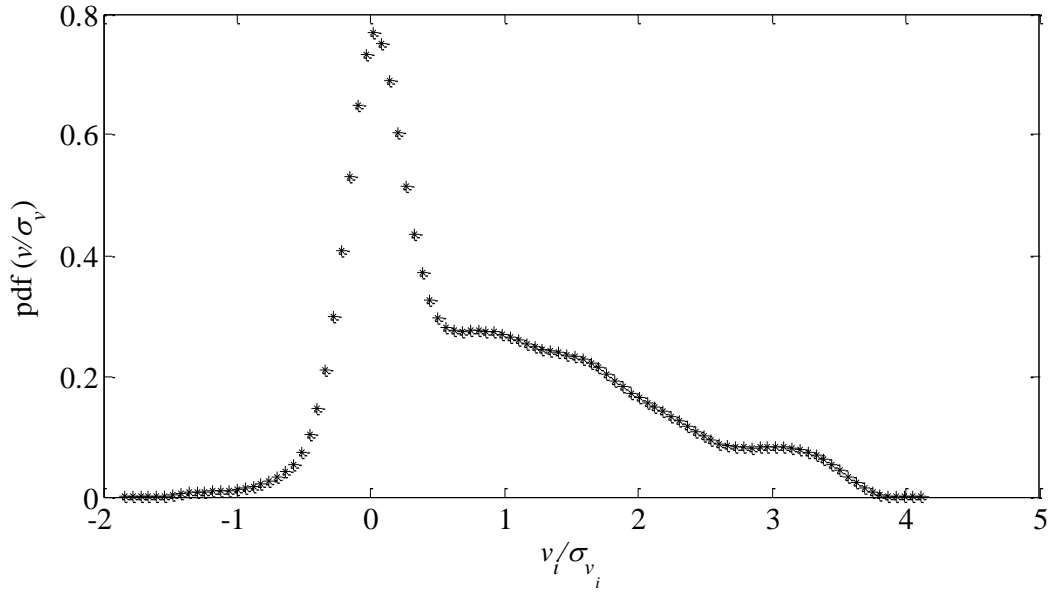


Figure 4-4 The probability density function (pdf) of non-dimensionalized transverse (y-component) velocity $\left(\frac{v}{\sigma_v}\right)$, where σ_v the standard deviation of v is, is plotted on the vertical axis and $\left(\frac{v}{\sigma_v}\right)$ is plotted on the horizontal axis. The probability density function is plotted using kernel density estimator

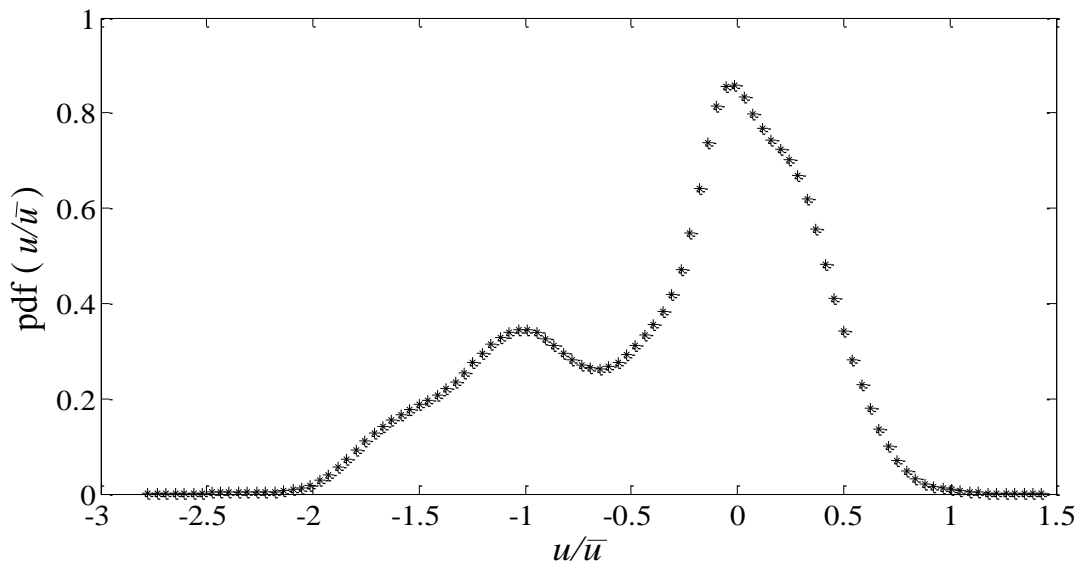


Figure 4-5 The probability density function (pdf) of non-dimensionalized longitudinal (x-component) velocity $\left(\frac{u}{\bar{u}}\right)$ is plotted. The probability density function is plotted using kernel density estimator

The pdf of v component of velocity is non-dimensionalized with its standard deviation and is plotted as shown in Fig. 4-4. The plots shows a longer tail on the positive axis which is due to the fact that v is mostly positive in the pore as shown from Fig. 4-2. The expected nature of the pdf curve is Gaussian, since v is the transverse component of velocity. However this measurement is taken for a single pore and the local behavior of v is captured. The longitudinal component of velocity, u , is non dimensionalized by its mean and the pdf of $\left(\frac{u}{\bar{u}}\right)$ is plotted as shown in Fig 4-5. Since the bulk flow is in the negative x direction, the positive tail of the curve shown in Fig. 4-5 is unusual. At such a low Reynolds number flow recirculation is not possible, so the nature of the curve can be due to the following reasons. It could be due to some local effect in the pore for which the bulk flow changes its direction. Another reason could misalignment of the direction of bulk flow with the axis of the camera, hence the image. It could be due to some spurious vector which was not removed during image post processing. To get a better idea of the flow field velocities from several different pores needs to be analyzed which can give unbiased results.

4.4 Summary

The optical system can successfully resolve the out of plane component of velocity field inside a micro- porous media. The out of plane component of velocity has a fluctuating nature with a mean value close to zero, which is confirmed from the shape of the pdf. The results obtained in the current study for w component of velocity agree well

with results obtained for experiments in macro-porous media. This confirms the similarity of flow properties for micro and macro porous media.

CHAPTER 5: CONCLUSION

A pore scale study of flow through micro porous media formed by packing of micro glass spheres is conducted. The pore scale velocity field is quantified using the μ -PIV setup. The optical system is capable of resolving velocity field at pore scale where the pore size is typically in the order of few microns. The image pre-processing algorithm used in the present study can successfully remove background noise and can enhance signal to noise ratio. The PIV+PTV algorithm was successfully used to obtain the 2C2D velocity field components and the 3D cross correlation algorithm was used to obtain the 3C3D velocity field. The statistical distribution of each component of velocity field is studied and results agreed with existing literature.

5.1 2C2D velocity field

Two in plane components of velocity field i.e., the transverse component and the longitudinal components of velocity field were studied. The study was conducted at different regions in the random porous bed. The average magnitudes of velocity in the narrow pore regions in between the spheres are found to be higher than at relatively bigger pores. The average magnitude of velocity was found to be higher at plane close to the wall ($z = 25\mu\text{m}$) compared to mid plane location ($z = 100\mu\text{m}$) of the first layer of spheres. The pdf of transverse component of velocity field non-dimensionalized with its standard deviation $\left(\frac{v_i}{\sigma_{v_i}}\right)$, closely fits to a normal distribution Gaussian curve and the results agree well with macroscopic study of porous media. The pdf of longitudinal velocity shows no negative tails where as evidence of negative tails was found in results

obtained numerically and experimentally for study of macroscopic porous media. The present study was conducted at low Reynolds number, $Re_p \sim 10^{-2}$ and the flow is strictly in creeping flow regime and no evidence of flow recirculation was found. The positive tails of longitudinal velocity changes with Reynolds number and the pattern agreed well with numerical and experimental work for macroscopic porous media.

5.2 3C3D velocity field

The preliminary results from 3C3D velocity field study capture some of the intricate flow structures. The Reynolds number for the study was found to be $\sim 10^{-6}$. The in-plane components of velocity shows cross flow patterns in the pore. The out of plane component of velocity, w is studied at different z plane locations and it was found that the value of out of plane component of velocity changes from positive to negative at different plane. This proves that flow reversal is taking place at different z planes. The out of plane component of velocity was found to fluctuate spatially. The probability density function of $\left(\frac{w}{\sigma_w}\right)$ closely resembles a Gaussian curve and the results agree with existing literature.

5.3 Future work

5.3.1 Matched refractive index technique

For the current study, the experiments were conducted at planes close to the wall as far optical access was possible. Using a matched refractive index technique the current study can be extended to few layers of spheres. A matched refractive index technique involves a fluid with same refractive index as that of the spheres. This makes the entire

medium optically transparent and optical access could be possible for few layers of spheres. However, precise refractive index matching is difficult to achieve as refractive index changes with temperature. A constant temperature should be maintained around the flow cell and setting up such an experimental setup needs rigorous engineering. Another potential problem in achieving matched refractive index is that the glass spheres have manufacturing defects in them. There are air bubbles trapped inside the micro glass spheres which may affect optical access. Northrup et al. (1993) used PMMA glass beds and used matched refractive index technique, however the glass beads were 9 mm in size. To conduct experiments using matched refractive index technique within micro porous media needs micro glass beads with minimum defects..

5.3.2 3D PIV +PTV

The PIV + PTV algorithm used for the 2C2D velocity field can be extended for three dimensional flow measurements within micro porous media. The volume of data obtained from each scan can be correlated using a 3D PIV + PTV algorithm to get more robust and reliable 3C3D vector field. At low Reynolds number where laminar flow conditions prevails, several volumes of time lapsed data can be averaged over to get the average velocity field. Such a velocity field can be used to study the spatial variation of velocity components in 3D within the micro porous media.

5.3.3 Validation of out of plane component of velocity

The out of plane component of velocity obtained from the experiment can be validated using continuity equation. The flow is incompressible and the divergence of

velocity should be zero. All the components of velocity are known which can be fed into the continuity equation and a zero divergence test can be done to validate the data.

5.3.4 Ordered porous media

The present study was done using a random porous media. A future study can be conducted by generating an ordered porous media. An ordered porous media can be obtained by packing of colloidal crystals as described by Kumacheva et al. (2003). The effect of different packing on the velocity field can be studied.

REFERENCES

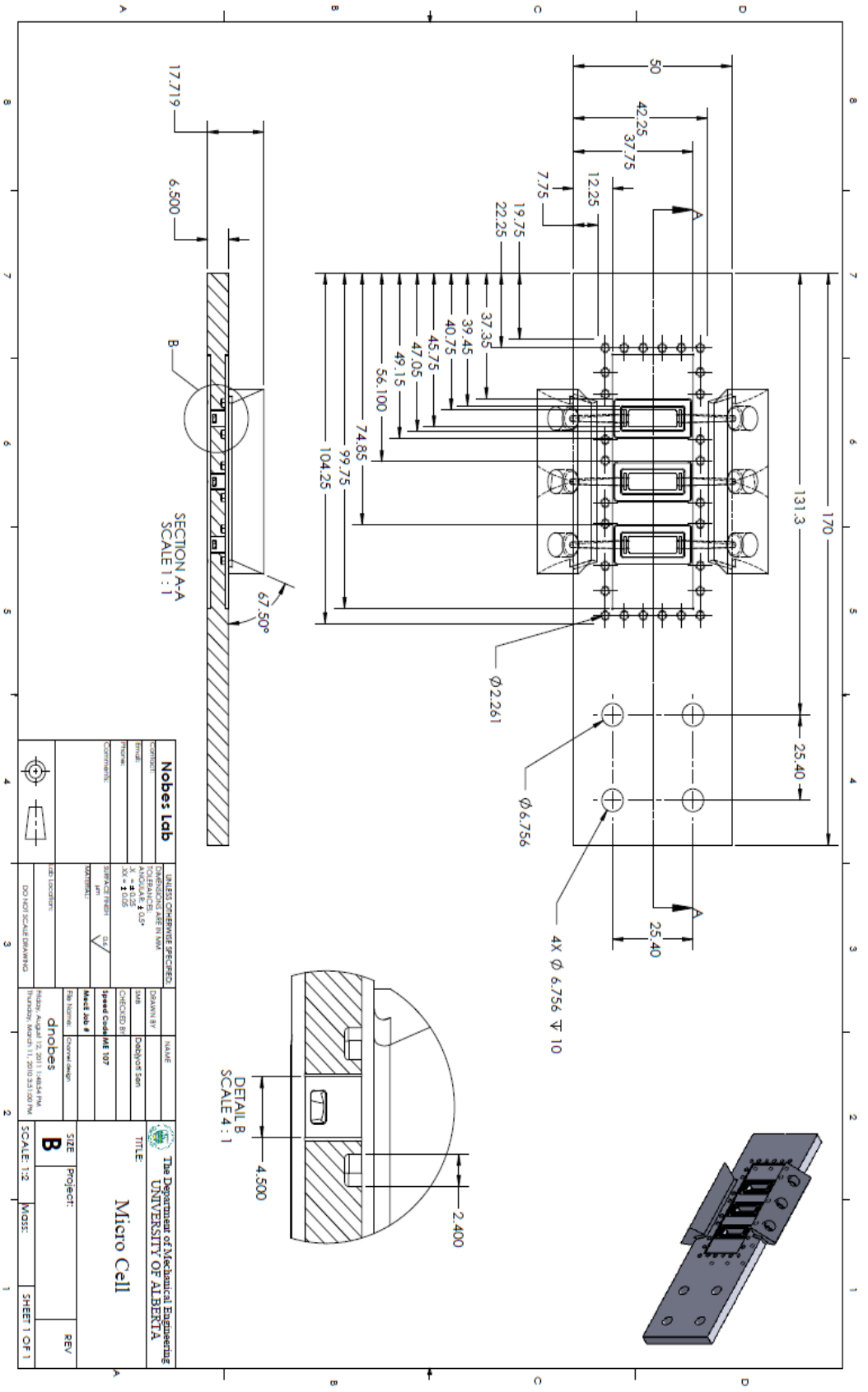
- Akanji, L.T. & Matthai, S.K., 2009. Finite Element-Based Characterization of Pore-Scale Geometry and Its Impact on Fluid Flow. *Transport in Porous Media*, 81(2), pp.241-259.
- Berejnov, V., Djilali, N. & Sinton, D., 2008. Lab-on-chip methodologies for the study of transport in porous media: energy applications. *Lab on a chip*, 8(5), pp.689-93.
- Dawe, R., Wheat, M. & Binder, M., 1992. Experimental investigation of capillary pressure effects on immiscible displacement in lensed and layered porous media. *Transport in Porous Media*, 7(1), pp.83-101.
- Dybbs, A. & Edwards, R.V., 1984. An indexed matched flow system for measurements of flow in complex geometries. In *Proceedings of an International Symposium on the Application of Anemometry to Fluid Mechanics, Laser Anemometry to Fluid Mechanics-II*. Lisbon, Portugal, pp. 171-184.
- Hatiboglu, C.U. & Babadagli, T., 2008. Pore-scale studies of spontaneous imbibition into oil-saturated porous media. *Physical Review E*, 77(6), pp.1-11.
- Hill, R., Koch, D. & Ladd, A., 2001. Moderate reynolds number flows in ordered and random arrays of spheres. *Journal of Fluid Mechanics*, 448, pp.243-278.
- Hoef, M. a V.D., Beetstra, R. & Kuipers, J. a M., 2005. Lattice-Boltzmann simulations of low-Reynolds-number flow past mono- and bidisperse arrays of spheres: results for the permeability and drag force. *Journal of Fluid Mechanics*, 528, pp.233-254.
- Homeniuk, D., 2009. *Development and testing of macro and micro three dimensional tracking system*. University of Alberta.
- Huang, A.Y.L. et al., 2008. Optical measurements of pore geometry and fluid velocity in a bed of irregularly packed spheres. *Experiments in Fluids*, 45(2), pp.309-321.
- Hunter, M.W., Jackson, a N. & Callaghan, P.T., 2010. Nuclear magnetic resonance measurement and lattice-Boltzmann simulation of the nonlocal dispersion tensor. *Physics of Fluids*, 22(2), p.027101.
- Johnston, W., Dybbs, A. & Edwards, R.V., 1975. Measurement of fluid velocity inside porous media with a laser anemometer. *Physics of Fluids*, 18, pp.913-914.
- Kajitani, L. & Dabari, D., 2005. A full three-dimensional characterization of defocusing digital particle image velocimetry. *Measurement Science and Technology*, 16, pp.790-804.

- Keane, R.D., Adrian, R. J. & Zhang, Y., 1995. Super resolution particle imaging velocimetry. *Measurement Science and Technology*, 6, pp.754-768.
- Kutsovsky, Y.E. et al., 1996. NMR imaging of velocity profiles and velocity distribution in bead packs. *Physics of Fluids*, 8, p.863.
- Lebon, L. et al., 1996. Pulsed gradient NMR measurements and numerical simulation of flow velocity distribution in sphere packings. *Physics of Fluids*, 8(2), pp.293–301.
- Lee, S.J. & Kim, S., 2009. Advanced particle-based velocimetry techniques for microscale flows. *Microfluidics and Nanofluidics*, 6(5), pp.577-588.
- Lindken, R. et al., 2009. Micro-Particle Image Velocimetry (microPIV): recent developments, applications, and guidelines. *Lab on a chip*, 9(17), pp.2551-67.
- Maier, R.S. et al., 1998. Simulation of flow through bead packs using the lattice Boltzmann method. *Physics of Fluids*, 10(1), p.60.
- Moroni, M. & Cushman, J.H., 2001. Statistical mechanics with three-dimensional particle tracking velocimetry experiments in the study of anomalous dispersion. II. Experiments. *Physics of Fluids*, 13(1), p.81.
- Neild, D. & Bejan, A., 2006. *Convection in porous media* 3rd ed., New York: Springer.
- Nobes, D.S., Abdolrazaghi, M. & Homeniuk, D., 2010. Three-component, three-dimensional velocity measurement technique for micro-channel applications using a scanning microPIV. In *15th International symposium on applications of laser techniques to fluid mechanics*. Lisbon, Portugal.
- Northrup, M.A. et al., 1993. Direct measurement of interstitial velocity field variations in a porous medium using fluorescent-particle image velocimetry. *Chemical Engineering Science*, 48(1), pp.13-21.
- Pattekar, A.V. & Kothare, M.V., 2005. A radial microfluidic fuel processor. *Journal of Power Sources*, 147(1-2), pp.116-127.
- Perrin, C. et al., 2005. Micro-PIV: A New Technology for Pore Scale Flow Characterization in Micromodels. In *Proceedings of SPE Europe/EAGE Annual Conference*. Madrid, Spain: Society of Petroleum Engineers.
- Prasad, A. et al., 1992. Effect of resolution on the speed and accuracy of particle image velocimetry interrogation. *Experiments in Fluids*, 13, pp.105-116.
- Sahimi, M., 1995. *Flow and Transport in Porous Media and Fractured Rock* 1st ed., New York, USA: Wiley-VCH.

- Saleh, S., Thovert, J.F. & Adler, P.M., 1992. Measurement of two-dimensional velocity fields in porous media by particle image displacement velocimetry. *Experiments in Fluids*, 12(3), pp.210-212.
- Santiago, J.G. et al., 1998. A particle image velocimetry system for microfluidics. *Experiments in Fluids*, 25(4), pp.316-319.
- Santosh, V. et al., 2007. Experimental and Numerical Investigations of Waterflood Profiles with Different Well Configurations. *Energy*, (7), pp.3353-3359.
- Scarano, F. & Reithmuller, M.L., 2000. Advances in iterative multigrid PIV image processing. *Advances in iterative multigrid PIV image processing*, 29, p.S051-S060.
- Shattuck, M. et al., 1991. Magnetic resonance imaging of interstitial velocity distributions in porous media. *Experimental techniques for multiphase flows*, 125, pp.39-45.
- Silverman, B.W., 1986. *Density estimation for statistics and data analysis*, Chapman & Hall/CRC.
- Stanislas, M. et al., 2005. Main results of second international PIV challenge. *Experiments in Fluids*, 39, pp.170-191.
- Takehara, K. et al., 2000. A kalman tracker for super-resolution PIV. *Experiments in Fluids*, 29, p.s34-s41.
- Theunissen, R., 2003. *Improvement of hybrid PIV and PTV algorithms and droplet sizing*. University of Technology Delft.
- Turta, A. et al., 2003. Toe-to-hill waterflooding. part II: Laboratory test results. In *SPE Annual Technical Conference and Exhibition*. Denver, Colorado.
- Vafai, K., 2005. *Handbook of Porous Media* 2nd ed., New York, USA: CRC Press.
- Vafai, K., 2010. *Porous media and its application in science, engineering, and industry* Third Inte., New York, USA: American Institute of Physics.
- Xu, R. & Jiang, P., 2008. Numerical simulation of fluid flow in microporous media. *International Journal of Heat and Fluid Flow*, 29(5), pp.1447-1455.
- Yu, C.H. & Kim, H.B., 2008. Stereoscopic micro-ptv measurement of micro impinging jet flow. In *ISFV13*. pp. 1-9.
- Zaman, E. & Jalali, P., 2010. On hydraulic permeability of random packs of monodisperse spheres: Direct flow simulations versus correlations. *Physica A: Statistical Mechanics and its Applications*, 389(2), pp.205-214.

APPENDIX A

Manufacture drawings of the flow cell and holder.



SECTION A-A
SCALE 1:1

DETAIL B
SCALE 4:1

Nobes Lab		UNLESS OTHERWISE SPECIFIED	
DIMENSIONS ARE IN MM		TOLERANCES ARE IN MM	
FINISH	COLLAR: 100	GRINDING	100
FORM	X = ± 0.25	Y = ± 0.25	Z = ± 0.25
TEXT	100 = 1.025	200 = 2.050	300 = 3.075
DATE	10/11/11	SCALE	1:1
DESIGNED BY	DR	CHECKED BY	DR
DRAWN BY	DR	DATE	10/11/11
PROJECT	Micro Cell	SCALE	1:1
REV		DATE	

APPENDIX B

The specification of the equipments used for the present study is listed here. The main components of the optical measurement system with their detailed specification is given below:-

Table B-1 Specification of the illumination source (continuous green laser)

Manufacturer	Laserglow Technologies
Model	LRS 0532-PFW02000-01
Operation Mode	Continuous
Maximum output power	15 W
Wavelength	532 +/- 1
Warm-up time	<10 mins

Table B-2 Specifications of fluorescent tracing particles

Manufacturer	Thermo Scientific
Model	R200
Absorption wavelength	532
Emission Wavelength	612
Size	2 μm
Material	Polystyrene
Density	1050 kg/m^3
Nominal size distribution	< 5%

Table B-3 Specification of the high speed camera.

Manufacturer	Basler
Model	piA 640-210 gm
Maximum frame rate	200
CCD sensor	1/3 inch, KAI 0340 DCM
CCD array size	640 × 480
Pixel size	7.4 μm
Data acquisition	Gigabit-Ethernet Port